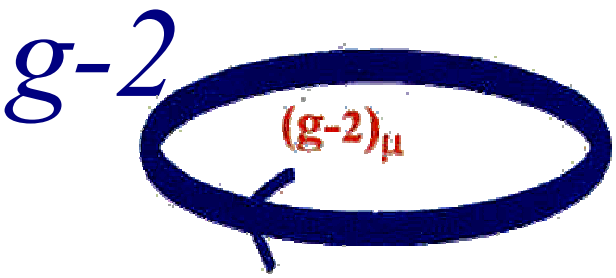

Brookhaven National Laboratory

Brookhaven Science Associates

Upton, New York 11973

Muon g-2 Note No. 442

Title: **2001 ω_a Analysis Using the Ratio Method with the G2)FF Production**

Author: **Jonathan M. Paley**

Affiliation: **Boston University**

Date: **February 13, 2004**

2001 ω_a Analysis Using the Ratio Method with the `G2OFF` Production

Jonathan M. Paley

February 13, 2004

Abstract

The 2001 g-2 spin precession frequency has been determined using the `G2OFF` production of the decay electron data and a multi-parameter ratio fit function. In this report we describe the method and systematic studies in detail. The data were split into two data sets, corresponding to the two n-values used in the electrostatic focusing of the beam: n=0.122 (low n) and n=0.142 (high n) and fit to a 9 parameter ratio function which incorporates CBO effects into the fit. R is defined as $R = 1 - \omega_a/\omega_{a_0}$, where $\omega_{a_0} = 2\pi \times 229.1$ kHz, however all R values quoted in this report have a global offset of -7.80 ppm. The final R values (with offsets) for both data sets are consistent with each other: 108.21 $\pm$ 0.91 $\pm$ 0.21 ppm for the low-n data set, and 108.42 $\pm$ 1.10 $\pm$ 0.22 ppm for the high-n data set. An additional, much smaller data set with n=0.122 for which the run-conditions were not ideal (however still acceptable) has also been analyzed, the result of which is R = 110.55 $\pm$ 3.73 $\pm$ 0.35. The first error is statistical, the second error is systematic.

Contents

List of Tables

Chapter 1

2001 Data Selection

1.1 Run Selection

In the following analysis, the 2001 data were divided into two groups, the data for n=0.121 (21.7 KV quads) and the data for n=.141 (25.3 kV quads). These will be referred to as the low n-value and the high n-value data sets, respectively.

The runs used were selected by Chris Polly, Xiaobo Huang and others, termed the 'golden runs'. Runs were selected based on experimental stability (ie: only runs after the detectors were calibrated and the electrostatic quadrupoles were "stable" were selected), accessibility/readability (some runs were simply lost or unreadable), and data content. The details of the run selection can be found in [2]. In the end, a total of 978 runs were selected, 606 of which were of the low n-value data set. This corresponds to, roughly, 1.7×10^9 and 1.2×10^9 decay electrons after 32 μs and with an energy > 1.9 GeV for the low and high n-value data sets respectively. With an average asymmetry of ~ 0.38, 2.9 billion decay electrons corresponds to a relative statistical uncertainty of ~ 0.77 ppm for ω_a.

An additional set of runs has also been analyzed which are labeled 'silver+bronze' (SB) runs. This set of runs includes data taken under non-ideal, but still acceptable, run conditions, such as low kick and low scraping voltages runs. In addition, 13 golden runs, which were missing from the `g2off` production were reproduced. All but four of these runs were taken with the low-n quadrupole high voltage settings, therefore the 'SB' list consists of 54 total runs, which contain approximately 160×10^6 decay electrons after 32 μs and with an energy greater than 1.9 GeV. Note, however, that the systematic studies were not done separately for this data set, which is only 1/10 the size of the larger low-n data set.

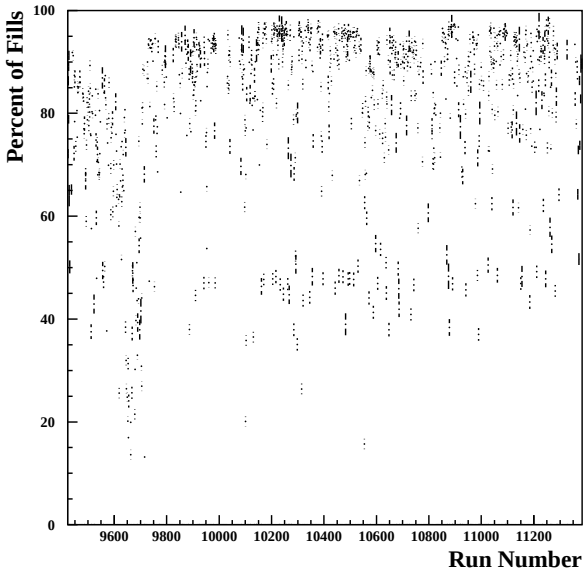

Figure 1.1: Percent of "good" fills vs. run number.

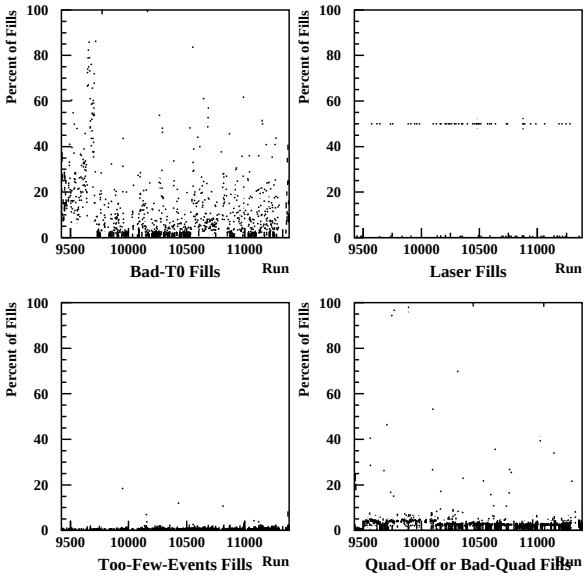

Figure 1.2: Percent of the different kinds of "bad" fills vs. run number.

1.2 Fill Selection

Quality-control was further enforced in this analysis in the form of fill cuts. We require that the quads be on for at least 700 μs after injection and that there is no sign of quadrupole sparking. To check if the quadrupoles sparked during a fill, the variables `QEARLY`, `QMID`, and `QLATE` are checked that they are not zero and that the difference between the mid and early values and the late and mid values are not "out of range", that is, we require `QMID-QEARLY` < 40 and `QLATE-QMID` < 15.

Other effects to look for are missing (or "bad") T0 pulses, fills where the laser is fired that may have escaped the original run selection, and a final requirement that there be a minimum number of 15 pulses in each fill for each calorimeter. Fig. 1.1 shows the percent of "good" fills vs. run number. The low percentage of good fills early on in the data-taking period is due to the T0 cuts (see Fig. 1.2). During these runs, the voltage on the T0 counter was set low so that often the T0 pulse was below threshold, thus not appearing in the data stream. This was eventually noticed and fixed, however we see that a fair amount (15%) of fills are lost due to this. However in terms of useful data, this turns out to be only 3.7% of the total number of pulses above the hardware threshold.

Late in the analysis, Qinzeng Peng discovered a large number of 'narrow pulses' in the `g2off` data. Narrowness of a pulse is defined as

$$n = \frac{a(k_{max} - 1) + a(k_{max} + 1)}{a(k_{max})} \tag{1.1}$$

where $a(k) = ISAM(k) - PED$, $ISAM$ is the 8-ADC sample of the pulse in the WFD, $k = 1, 8$, k_{max} is the element in the array with the largest value (the peak of the pulse) and PED is the minimum value in $ISAM$. Narrow pulses therefore have a small value of n, and 'normal' pulses have values of n ranging from 1-2. Peng also succeeded in discovering two types of narrow pulses, one with 'one peak', and the other with 'two peaks'. The two peak narrow pulses have been identified as pulses that were mis-constructed due to misalignment in the marker pulse, which aligns the two phases of the WFD. The cause of the mis-constructed marker pulses was determined to be due to noise on the baseline before the marker pulse which confused the phase-alignment algorithm Since the pulses in such mis-aligned fills were mis-constructed, they must not be included in the data. Peng has also shown that all narrow pulses have a `FITCHI2` greater than 20, whereas 'good' pulses have a `FITCHI2` less than 18. Therefore, fills for which the average `FITCHI2` is greater than 20 are thrown out.

1.3 Energy Calibration

The traditional way of calibrating the calorimeter pulse height data to actual energy is to obtain energy spectra in units of ADC counts, and fit the linear region found in the higher end of the spectrum to a straight line. The point where it crosses the axis (the "endpoint") is then assumed to be 3.1 GeV, and

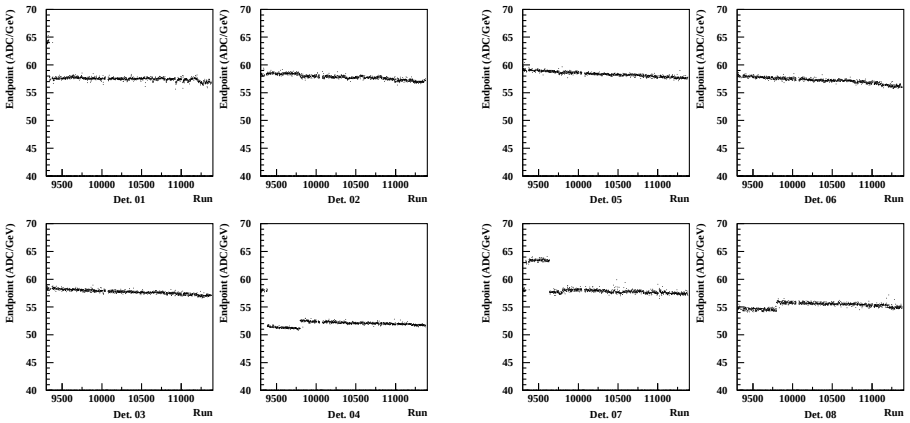

(a) Detectors 1-4

(b) Detectors 5-8

Figure 1.3: Energy calibration on a run-by-run basis.

one now has a conversion between ADC counts and energy. Xiaobo Huang has done this for the `G2OFF` data, and Figs. 1.3-1.5 show the endpoints for the individual detectors on a run-by-run basis. One can see that over time the pulses became slightly smaller, which is not unexpected since detectors and electronics can degrade over time.

Given these endpoints, two-dimensional Energy vs. Time histograms were constructed, with energy binned in 0.2 GeV steps, and time binned in 0.4365 μs steps, roughly 1/10 the g-2 period. This was originally done in order to look at average energy vs. time in the fill, and to do this one must bin out the g-2 period. The results of that study are found in Section 3.2.

At present however, we fit the energy-integrated data, summed over all runs, at late times ($\sim 180\mu s$) with different energy thresholds to obtain $A(E_t)$, $N(E_t)$ and $NA^2(E_t)$, where E_t is the energy threshold, and energy is defined by Xiaobo's endpoints. The plots in Figures 1.6-1.7 show the dependence of A, N and NA^2 on energy threshold for detector 1.

We wish to minimize the statistical error on ω_a and therefore we need to maximize NA^2. Fitting a 7^{th} order polynomial to the histogram of NA^2, we then set the derivative of the fitted polynomial to zero and find the root (we use the `CERNLIB` function `RZERO` to do so). Fig. 1.8 shows the energies, expressed in GeV (defined by the determined endpoints), where NA^2 is maximized for each detector. These are the energy thresholds that are used for each detector. An upper energy cut of 3.2 GeV is applied to all detectors when filling the time spectra. This choice is based on the fact that we should have very few decay electrons above 3.1 GeV as well as the desire to eliminate as many pileup events from entering into the decay spectrum.

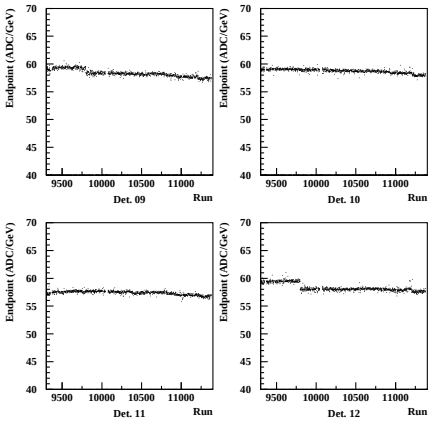

(a) Detectors 9-12

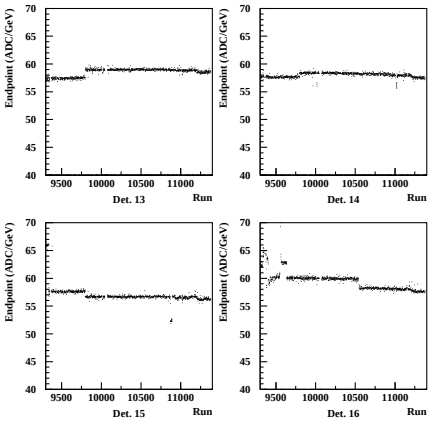

(b) Detectors 13-16

Figure 1.4: Energy calibration on a run-by-run basis.

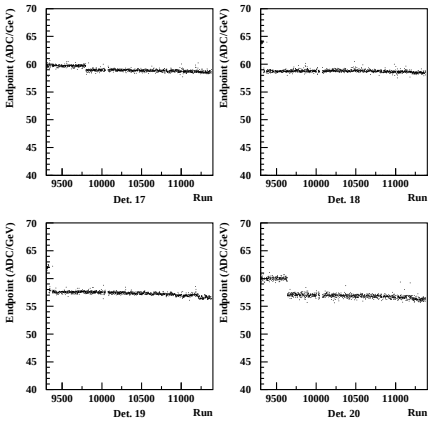

(a) Detectors 17-19

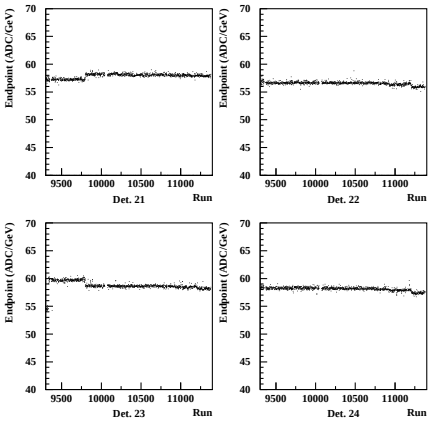

(b) Detectors 21-24

Figure 1.5: Energy calibration on a run-by-run basis.

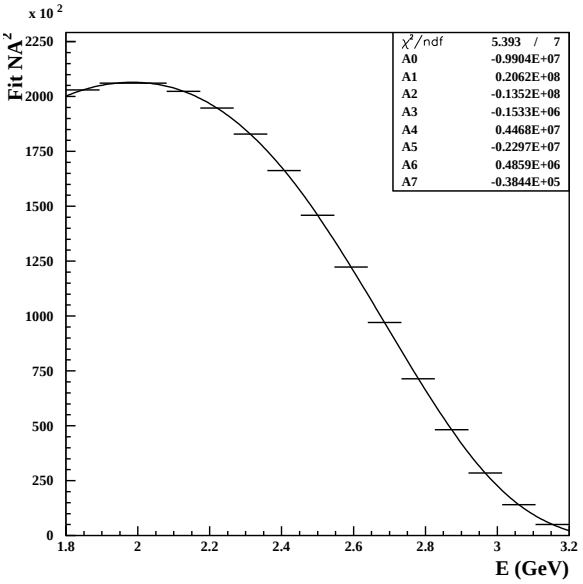

Figure 1.6: Fit NA^2 vs. lower energy threshold. The histogram is fit to a 7^{th} order polynomial in order to determine the maximum value of NA^2, which will minimize the statistical error on the fitted value of ω_a.

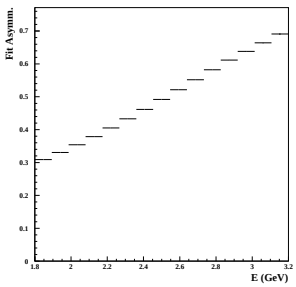

(a) Fit asymmetry vs. low energy threshold.

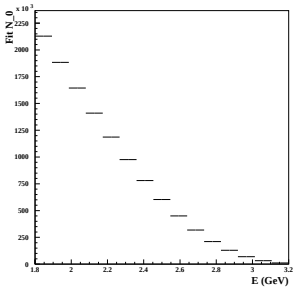

(b) Fit N vs. low energy threshold.

Figure 1.7: All plots are for detector 1.

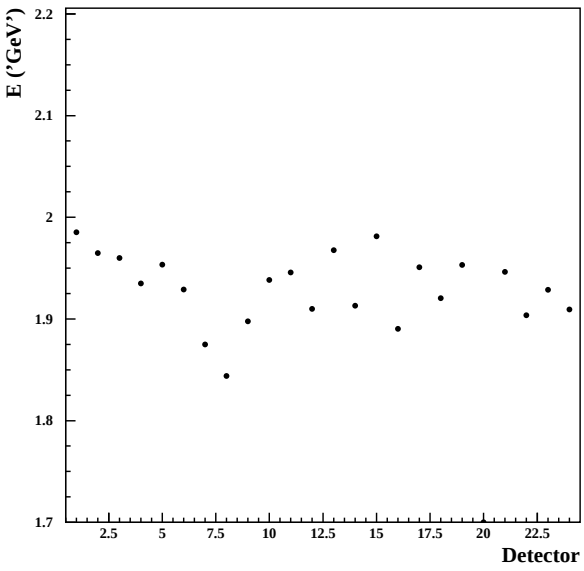

Figure 1.8: Energy threshold values at the peak of NA^2 vs. E_t.

Chapter 2

2001 ω_a Analysis

2.1 The Ratio Method

The ratio method was originally derived by Yuri Orlov and first implemented by Joel Kindem. Since then, the ratio method has been used in the analysis of the 1999 data by Long Duong and the 2000 data by Ben Bousquet. The basic idea is to shift one quarter of the data forward in time by half a g-2 cycle, shift another quarter of the data backward in time by half a g-2 cycle, and leave the remaining one-half of the data untouched. If the spin precession frequency is already known to within sufficient accuracy, one can then reduce the five-parameter function

$$N_5(t) = N_0 e^{-t/\tau}(1 + A\cos(\omega_a t + \phi) \tag{2.1}$$

to a three-parameter function

$$r(t) = A\cos(\omega_a t + \phi) + C_1 \tag{2.2}$$

by taking a ratio of differences over sums of the shifted and non-shifted data (see Section A.1 for details of the method). Figs. 2.1 and 2.2 show the $N(t)$ spectrum and the same data converted into the ratio ($r(t)$) spectrum.

However, much work was put into this analysis to properly account for CBO in the fitting function. Therefore, several functions were used in fitting the data; in the end, it was decided that a 9-parameter ratio function best describes the data, and it is from fits to this function that the final values of R are taken. A comparison of the fit results using the various fit functions may be found in Section 2.7.

2.2 CBO Parameters

If one assumes the same exponentially decaying CBO envelope for N_{cbo}, A_{cbo} and ϕ_{cbo}, then Eq.A.33 has 11 parameters: the three from Eq. A.20, the three

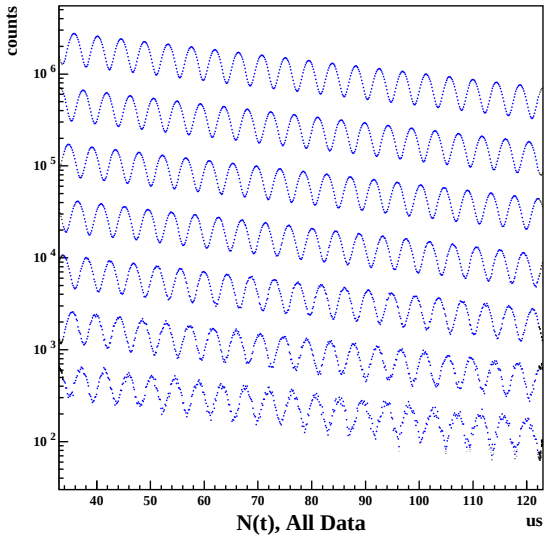

Figure 2.1: Original N(t) spectrum, plotted on a log vertical scale. The horizontal axis is modulo 90 μs, starting from 33 μs after injection.

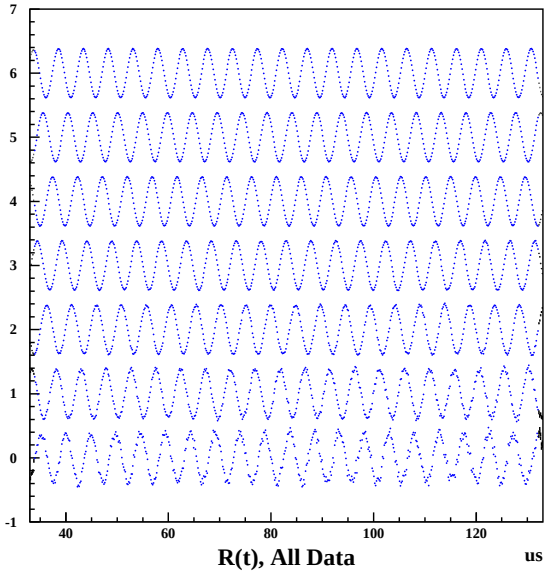

Figure 2.2: Ratio ($r(t)$) spectrum, again plotted modulo 90 μs however on a linear vertical scale. The data in Fig. 2.1 has been converted into a pure cosine via the method described in Section A.1. For display purposes, each 90 μs segment has been shifted up, so that the first segment is centered on 6, the second is centered on 5, etc.

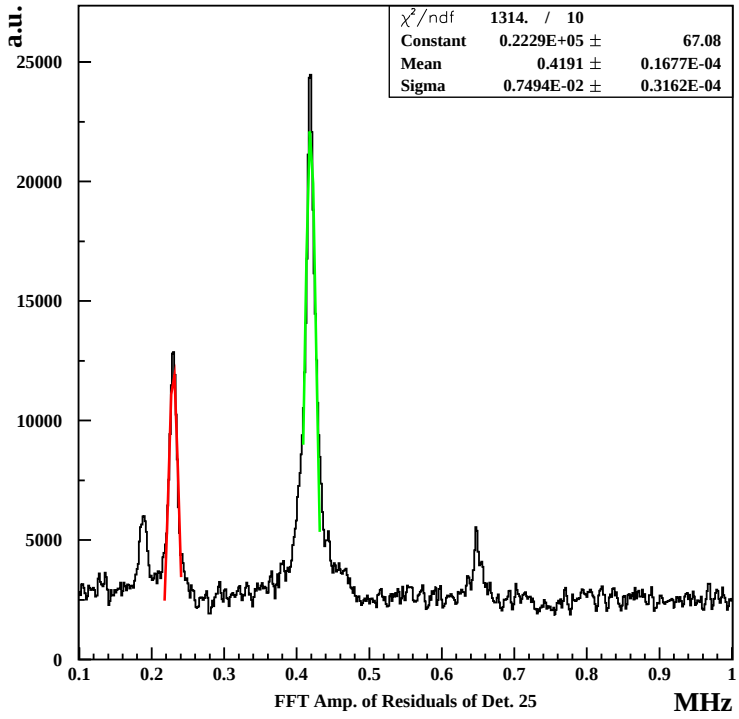

Figure 2.3: FFT of the residuals from a 5 parameter fit at 180μs of the usual time spectrum of the low n-value data set. The main CBO peak was fit to a Gaussian, the results of which are shown in the upper right-hand corner.

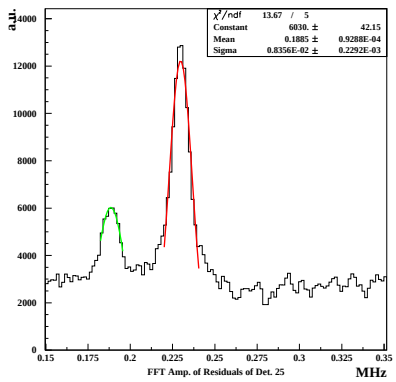

(a) Same as Fig. 2.3, lower frequency range.

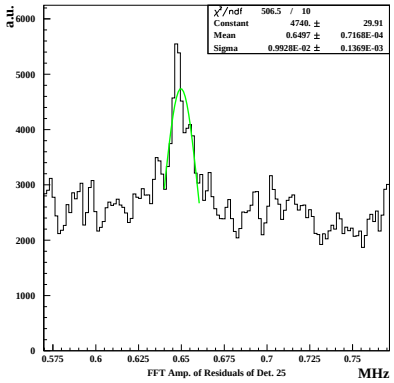

(b) Same as Fig. 2.3, higher frequency range.

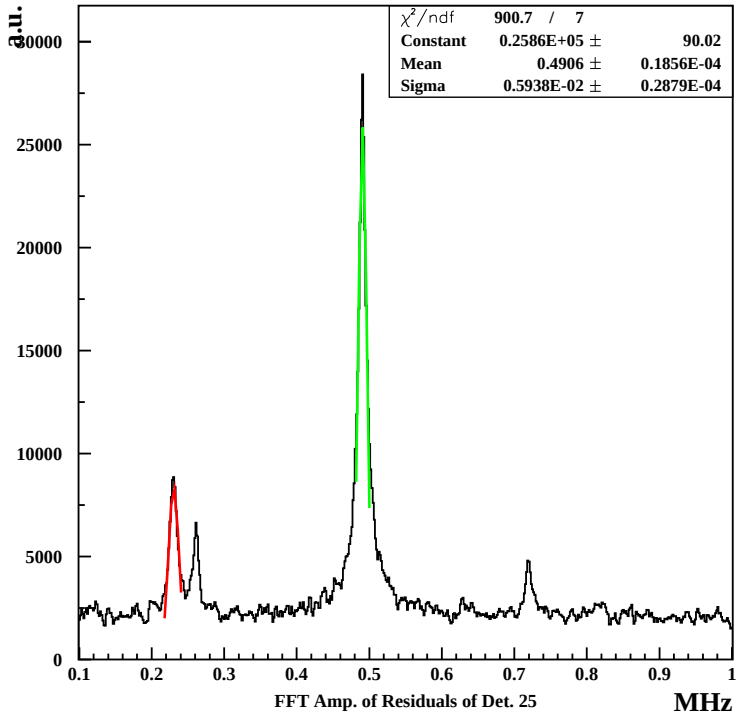

Figure 2.4: FFT of the residuals from a 5 parameter fit at 180μs of the usual time spectrum of the high n-value data set. The main CBO peak was fit to a Gaussian, the results of which are shown in the upper right-hand corner.

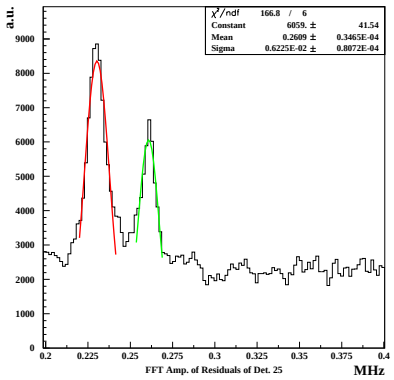

(a) Same as Fig. 2.4, lower frequency range.

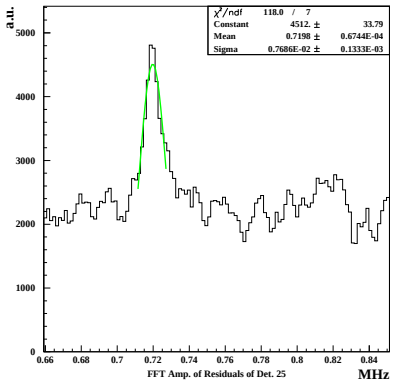

(b) Same as Fig. 2.4, higher frequency range.

Low n-value Data Set				
	main cbo	g-2	lower cbo sideband	upper cbo sideband
freq. (kHz)	419.06	229.75	188.46	649.74
sigma (kHz)	7.49	6.73	8.36	9.93
amp. (a.u.)	22293.	12224.	6029.7	4739.6
High n-value Data Set				
	main cbo	g-2	lower cbo sideband	upper cbo sideband
freq. (kHz)	490.62	230.25	260.87	719.76
sigma (kHz)	5.94	7.43	6.22	7.69
amp. (a.u.)	25861.	8355.1	6058.6	4512.0

Table 2.1: Results of Gaussian fits to the four main peaks in the FFT spectrum of residuals to fits at late times.

CBO amplitudes and their phases, the CBO lifetime, and the CBO frequency. However, we can reduce the number of parameters by obtaining the CBO frequency and lifetime empirically. The CBO frequency is quite easy to obtain: simply fit the time spectra to the five parameter function at late times (in this case, $\sim 180\mu s$ after injection), subtract the results, and Fourier transform the residuals (i^{th} residual $= N_{i_{fit}} - N_{i_{data}}$). The results of this approach are shown in Figs. 2.3- 2.2. The top plots show the frequency range of 100-1000 kHz, and four peaks are immediately discernable: the main CBO peak, the residual g-2 signal at $\simeq 229.1$ kHz, and the "lower" and "upper" CBO sidebands ($f_{cbo} - f_{g-2}$ and $f_{cbo} + f_{g-2}$). To obtain values for the CBO frequencies, Gaussian fits around the peaks' were performed, the results of which are summarized in Table 2.1 (the results are also printed in the upper right corners of each plot). The top plots show the range of frequencies from 100 to 1000 kHz, with the CBO peak fit in green and the residual g-2 peak fit in red (the fit results of the g-2 peak are not printed in the corner, however). The bottom plots show narrower frequency ranges to zoom in on the sideband frequencies, the left plot showing the lower CBO sideband and the right plot showing the upper CBO sideband. The sideband fits are in green and the fit results are printed in the uppper right corner; again, the red line is the residual g-2 peak.

We now have reduced Eq. A.33 to 10 parameters by eliminating the need to fit for the CBO frequency. We can further reduce the number of free parameters by determining the CBO lifetime. This was done by looking at the average energy vs. time, using time bin widths smaller than the g-2 period. In particular, in this study, the time bin width is 1/8 of a g-2 period. The energy distribution varies a great deal over a g-2 period, since at the peak of the g-2 period there are many more high-energy decay electrons than at the trough of the period. However, the energy distribution is effectively the same every eighth time bin (always at the same g-2 phase), yet it is very sensitive to CBO acceptance effects,

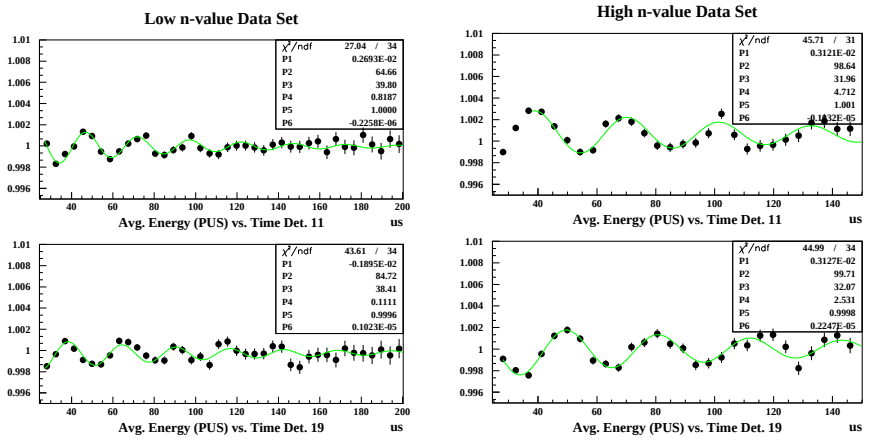

(c) Low n-value data set.

(d) High n-value data set.

Figure 2.5: Average energy vs. time where only decay electrons falling within the same g-2 phase are considered. The acceptance effect of CBO is very apparent, and the histograms are fit to Eq. 2.3 in order to extract the frequency and lifetime of the CBO.

especially those energy distributions of decay electrons coming near the peak of the g-2 oscillation. Just a few examples of the CBO acceptance effect on the average energy are shown in Fig. 2.5, for detectors 11 and 19, for both data sets.

The oscillations are stunningly clear, and in fact are present in nearly all eight g-2 phases, not just those near the g-2 peak. Therefore the data for detectors 9-24 (except 20) were fit (in the range of $\sim$ 30 to $\sim$ 200μs) to the function

$$< E_{T_a/8} > (t) = Ae^{-t/\tau_c}\cos(\omega t + \phi) + c_1 t + c_0 \qquad (2.3)$$

where $A = p1$, $\tau_c = p2$, $\omega = p3$, $\phi = p4$, $c_1 = p5$ and $c_0 = p6$. We obviously have assumed here an exponential decay as the CBO envelope, and the c_1 and c_0 parameters of the fit function are present in order to account for actual gain. For detectors 9-24, a linear function is sufficient to describe the changes in average energy. Since there are eight g-2 phases and 15 detectors used in this study, a total of 120 fits were made. Cuts on the fit results were applied (reasonable values of fit $\chi^2/d.o.f.$ and reasonable values of fit parameters and errors on the fit parameters), and typically about 2/3 of the fits were found to be acceptable.

The distributions of the fitted CBO lifetimes and frequencies and fit $\chi^2/d.o.f.$ of the acceptable fits are shown in Figs. 2.6-2.7. The mean CBO frequencies, $f = |f_c - 2f_{g-2}|$, are found to be $f_{cbo} = 418.7 \pm 0.2$ and 490.3 ± 0.2 kHz for the low and high n-value data sets respectively. These agree to within 2 σ with

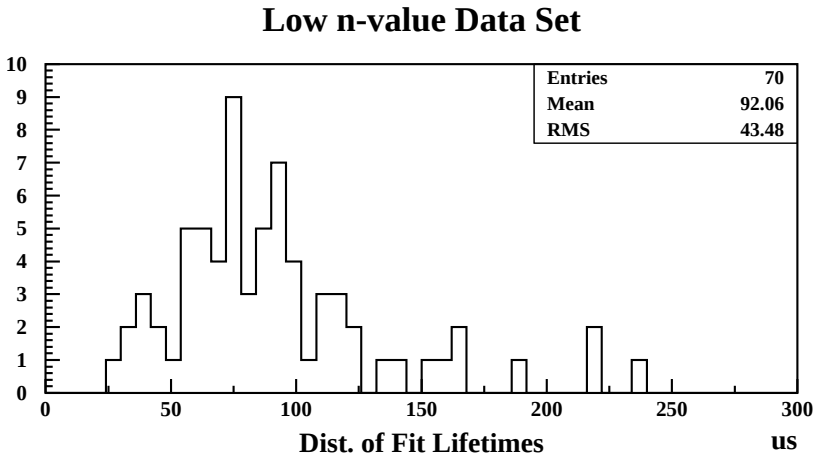

Figure 2.6: Distributions of fit CBO lifetime obtained from fits to $< E_{T_a/8} >$ vs. time plots (low n-value data set) to Eqn. 2.3.

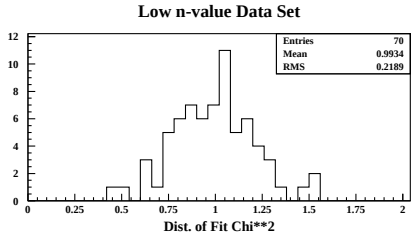

(a) Distribution of fit χ^2 for the study described in Fig. 2.6

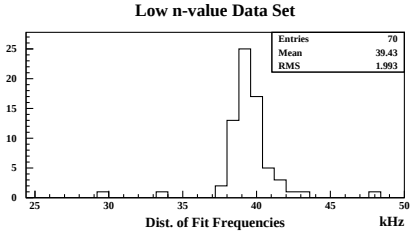

(b) Distribution of fit CBO frequencies for the study described in Fig. 2.6

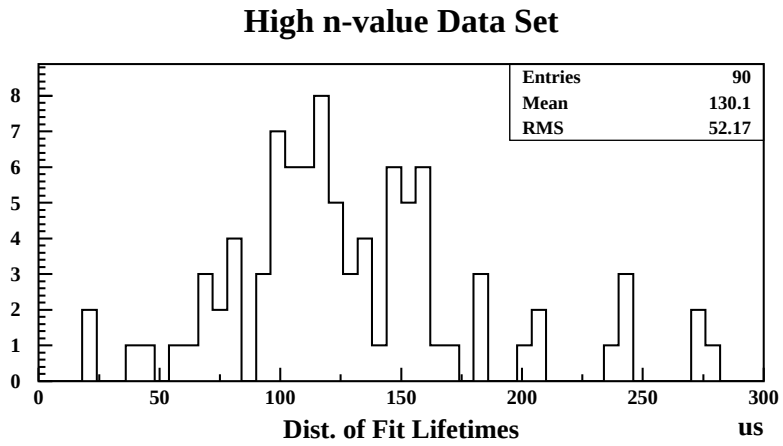

Figure 2.7: Distributions of fit CBO lifetime obtained from fits to $< E_{T_a/8} >$ vs. time plots (high n-value data set) to Eqn. 2.3.

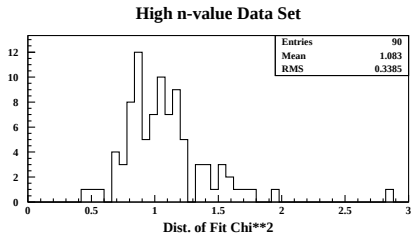

(a) Distribution of fit χ^2 for the study described in Fig. 2.7

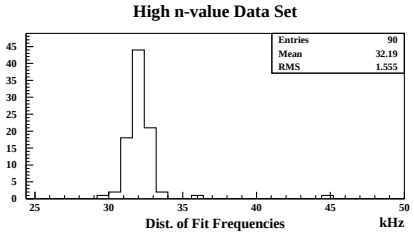

(b) Distribution of fit CBO frequencies for the study described in Fig. 2.7

the CBO frequencies found above. The means of the distributions of the fit χ^2 also agree with the expected value of 1.0 to within 2 σ. Finally, the mean CBO lifetimes found are 92.1 ± 5.2 and $130.1 \pm 5.5 \mu s$ for the low and high n-value data sets respectively. These are the values of the lifetimes used in the fits in this analysis.

2.3 Removing Pileup From the Data

When two decay electrons hit a detector within the detector's deadtime, the two pulses cannot be separated by the pulse-finding algorithm and are treated as one pulse. These pileup events affect the time spectrum of the decay electrons by creating a background term with its own asymmetry and g-2 phase, which is highly correlated to the spin precession frequency. The pileup background term is well understood, and could be included in a fit, however any uncertainty in the pileup phase on the order of tens of mrad can induce a systematic shift in the fit value of the spin precession frequency on the order of a few tenths of a ppm. Instead of fitting to the pileup background term, methods to statistically construct the pileup by looking at 'shadow' pulses have been developed that allow one to subtract the pileup from the data *before* fitting to relatively high accuracy. Since the pileup is reconstructed, the issue of any uncertainty in phase of the pileup is greatly reduced.

In this analysis, we use the pileup contruction algorithm derived in [3], using an energy-dependent deadtime and an energy-dependent scale factor for combining two pulses calculated by Ivan Logashenko. Typical values for the deadtime and scale factor are 2.9 ns and 0.96, respectively. The time offset of the shadow pulse search window is set to 12 ns for all detectors. Figs. 2.8-2.10 show the energy spectra of the individual detectors before pileup subtraction (black) and the energy spectra of the constructed pileup events (blue and red). The number of pileup events goes negative around 2.6 GeV; this means that below 2.6 GeV, pileup events have a *negative* contribution to the number of detected decay electrons, whereas above 2.6 GeV pileup events have a *positive* contribution. The actual energy at which the pileup spectrum crosses zero as a function of detector is shown in Fig. 2.11.

Time spectra of the constructed pileup events using different energy cuts for detector 1 are shown in Fig. 2.12. Note that for the nominal cuts ($1.9 < E < 3.2$ GeV) applied to the data, the number of pileup events as a function of time oscillates near zero and therefore the integrated number of events is very close to zero. This is not surprising, since if one looks at Figs. 2.8-2.10 then it is clear that from 1.9-3.2 GeV, nearly half the constructed PU events contribute negatively (the lower energy events) and the other half contribute positively (the higher energy events).

In order to estimate the efficiency with which we construct pileup, we compare energy spectra obtained during different times from the spill. Specifically, we compare both pileup-subtracted and unsubtracted energy spectra of decay electrons detected from 20-250 μs after injection to energy spectra from elec-

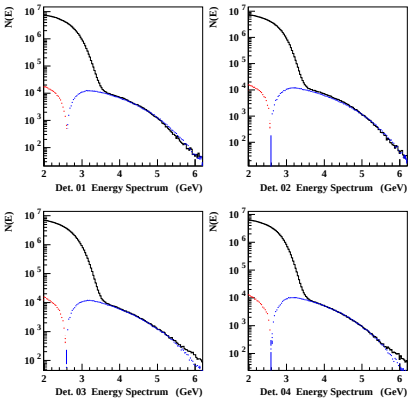

(c) Detectors 1-4.

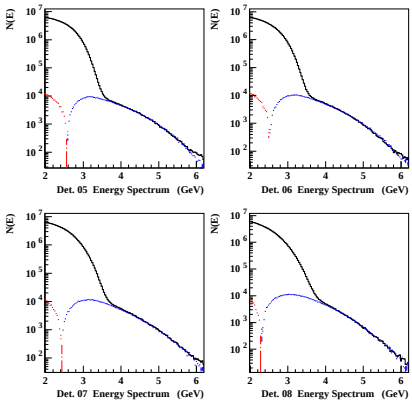

(d) Detectors 5-8.

Figure 2.8: Energy spectra for the individual detectors. The black line represents the spectrum before pileup subtraction, the blue line represents the spectrum of the positive contribution of the pileup events, and the red line represents the spectrum of the negative contribution of the pileup events.

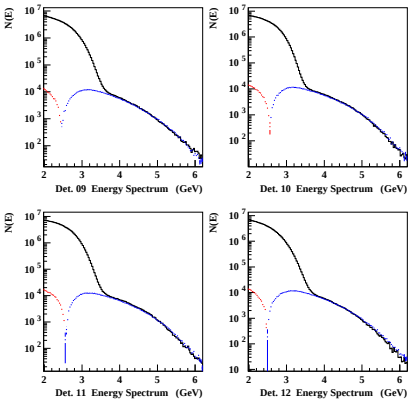

(a) Detectors 9-12.

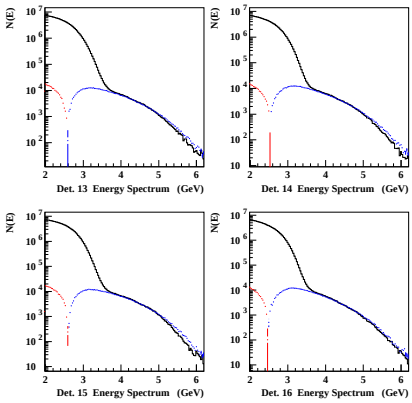

(b) Detectors 13-16.

Figure 2.9: Same as Fig. 2.8.

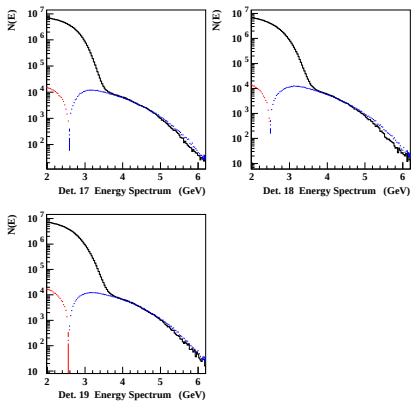

(a) Detectors 17-19.

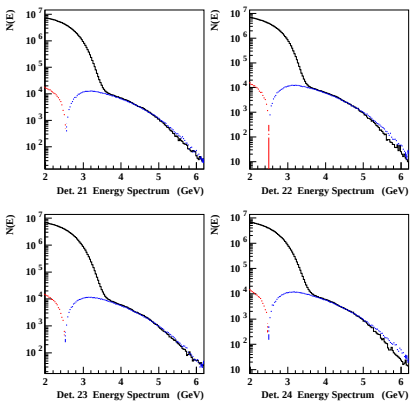

(b) Detectors 21-24.

Figure 2.10: Same as Fig. 2.8.

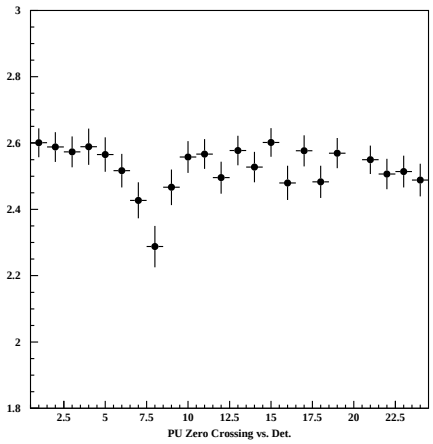

Figure 2.11: Energy at which the number of pileup events crosses zero as a function of detector.

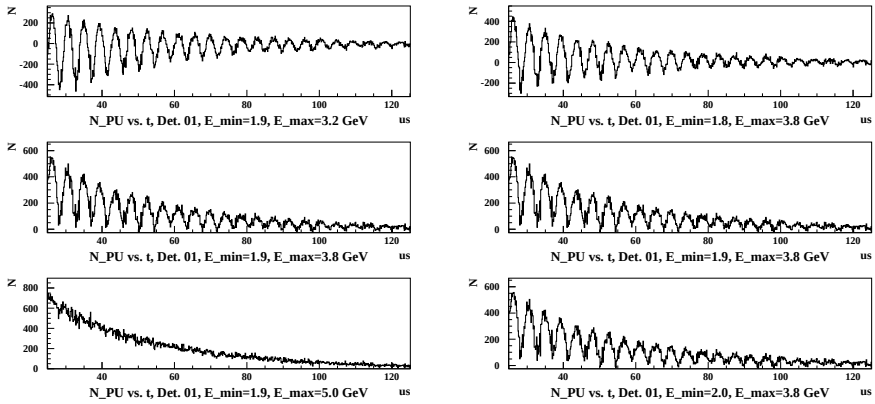

(a) Lower energy threshold is fixed, upper energy threshold is varied.

(b) Upper energy threshold is fixed, lower energy threshold is varied.

Figure 2.12: Constructed pileup time spectra for detector 1 using different energy cuts.

trons detected after 250 μs. Since there is less data after 250 μs, the energy spectra from the late-time data must be scaled up by a factor λ. The scale factor λ is obtained by taking the ratio of $N_{early}(E)$ to $N_{late}(E)$ and fitting the region 2.3 GeV $< E <$ 2.7 GeV to a constant. Typical values for λ are 34.3, which is very close to what one would expect from the simple approximation of $exp((250-20)/64.4$.

We define the parameter ζ such that

$$\zeta(E) = \frac{N_{early_{PUS}}(E) - \lambda N_{late}(E)}{N_{early}(E) - \lambda N_{late}(E)} \tag{2.4}$$

In the region where pileup dominates the spectrum, energies above 3.1 GeV, the average value of ζ is an approximation of the inefficiency with which we construct the pileup. Fig. 2.13 shows the average values of ζ versus detector, where the average value of ζ is taken from 3.1-4.5 GeV. With a few exceptions, we typically construct pileup with an efficiency $> 95\%$.

2.4 Energy Scale Changes

If the energies of the detected decay electrons change with time, due to detector/PMT response (gain), residual pileup, etc., then this introduces an early-to-late effect on the counting rate. If not dealt with properly, this is problematic when fitting the data.

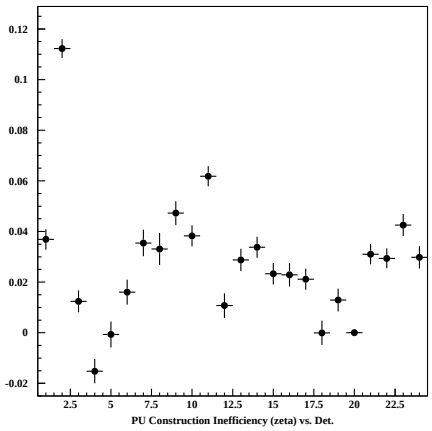

Figure 2.13: Pileup construction efficiency (average ζ from 3.1-4.5 GeV) vs. detector.

One way to get a handle on energy scale changes is to look at average energy as a function of time in the fill. Figures 2.14- 2.16 show the normalized average energy vs. time in the fill for each detector, using the entire data set. The normalization is with respect to the average energy of decay electrons detected after 250 μs. The red circles show the average energy vs. time before pileup subtraction and the blue triangles show the average energy vs. time after pileup subtraction. We see that at early times pileup raises the average energy by about 0.07-0.08%.

Of particular concern are detectors 3-7 which show not only very large changes in $< E >$ vs. time, but the time-dependence of these changes does not 'behave' as any of the other detectors. The cause of these large, odd-shaped changes in average energy during the first 100 μs for these detectors has been found by Logashenko to be due to the treatment of island length by the `G2OFF` production. Detectors 3-7, because of their close proximity to the injection point, see the largest amount of flash, and at early times the detectors continuously digitize. The very long islands of data seen during and just after the WFDs' continuous digitization are broken up into smaller islands in order to fit the individual pulses. This affects the number of samples each pulses is fit to, and since there is an early-to-late change in the number of samples used in the pulse fitting routine, one finds an early-to-late affect on the average energy. According to Logashenko, "[the] pulse shape is known only to few-percent precision, and the pulse has a long tail. Therefore, when we fit to a different number of sample, we get slightly different fit result. The figure of merit is the following: if one changes the island length by 1 sample, the reconstructed pulse amplitude will change by [10^{-4}]. In the worst case the average island length changes by 10 samples, which lead to [an effect of] about [10^{-3}]." The large change in average energy for these detectors is not as dramatic in the `g2Too` production because

the number of samples fitted per pulse is fixed and therefore only islands with multiple pulses are affected. On the otherhand, the `G2OFF` production island with just one pulse are also affected.

Logashenko has also shown that one may treat this early-to-late change in the average WFD island length problem as a linear energy-scale change. However another systematic error arises due to the effect of having multiple pulses on a single island; this will be discussed and evaluated in Section 3.2.

Until the cause of the large changes in average energy was discovered, several other possible causes were investigated. We document these studies here for both their historical and "physics" value.

Lost antiprotons ($\bar{p}$) were suggested as a possible source for the large changes in $< E >$ seen in detectors 3-7. However, it was determined that the $< E >$ changes by $\sim 0.03\%$ per 1% of $\bar{p}$ contamination. The ratio of $N_{\bar{p}}$ seen after the quadrupoles are turned off to N_{e^-} is $< 0.3\%$. Therefore we would need to be losing an unreasonable amount of antiprotons at early times to see any measureable effect on the $< E >$.

Neutrons, which show up as 'narrow pulses' in the calorimeters, were also proposed as a possible candidate for the large changes in $< E >$ vs. time seen in detectors 3-7. However, this model was ruled out since detector 8 which sees an order of magnitude more narrow pulses than detectors 3-7, does not see large changes in average energy vs. time.

As shown previously, pileup, if not subtracted from the data, changes the average energy by almost 0.1% at very early times. If we subtract pileup with with better than 95% efficiency, then we expect a $5\% \times 0.1\%$ change in $< E >$ at the earliest times, which again is completely negligible in comparison to the size of the changes in $< E >$ seen in the first 100 μs (of order 0.2%).

We assume that the changes seen are true energy-scale changes due to some linear effect on the energies of the decay electrons, whether it is PMT gain or an effect due to the pulse fitting algorithm. Since the decay electron energy spectrum is not flat versus energy, we must determine how the ratio of early-to-late average energies relates to 'gain', where 'gain' is defined as a linear change in a detector's pulse height. In other words, we need to understand how to go from

$$\frac{E_g}{E} = 1 + g \tag{2.5}$$

to

$$\frac{< E_g >}{< E >} = 1 + m \cdot g \tag{2.6}$$

where m relates changes in average energy to gain. To determine m, we apply various software gains to late-time data where energy-scale changes are assumed negligible and plot the ratio $< E_g > / < E >$ vs. gain for each detector. The plot on the left of Fig. 2.17 shows such a plot for detector 10, and the plot on the right shows the extracted slope, or m, for each detector. Having determined m, we next determine

$$f_g(t) = \frac{< E_g >}{< E >}(t) \tag{2.7}$$

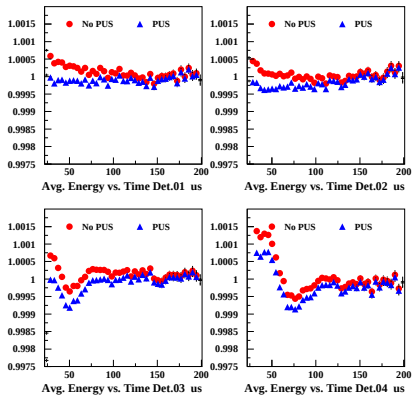

(a) Detectors 1-4.

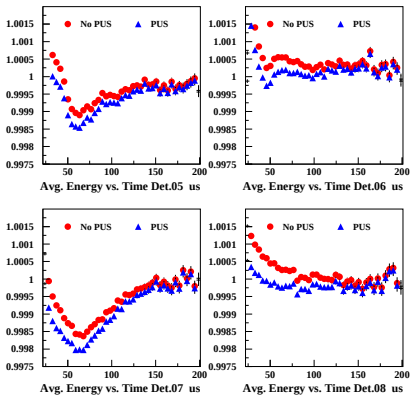

(b) Detectors 5-8.

Figure 2.14: Average energy vs. time after injection. The red circles are $\bar{E}/\bar{E}_{late}$ for non-pileup-subtracted data, the blue triangles are $\bar{E}/\bar{E}_{late}$ for pileup-subtracted data.

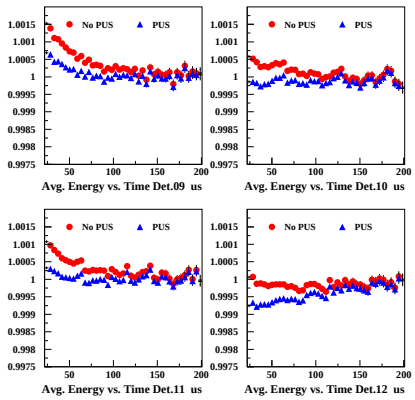

(a) Detectors 9-12.

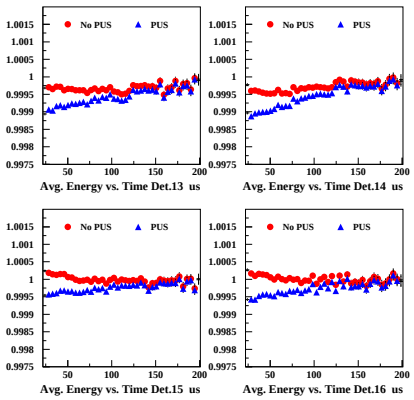

(b) Detectors 13-16.

Figure 2.15: Same as in Fig. 2.14.

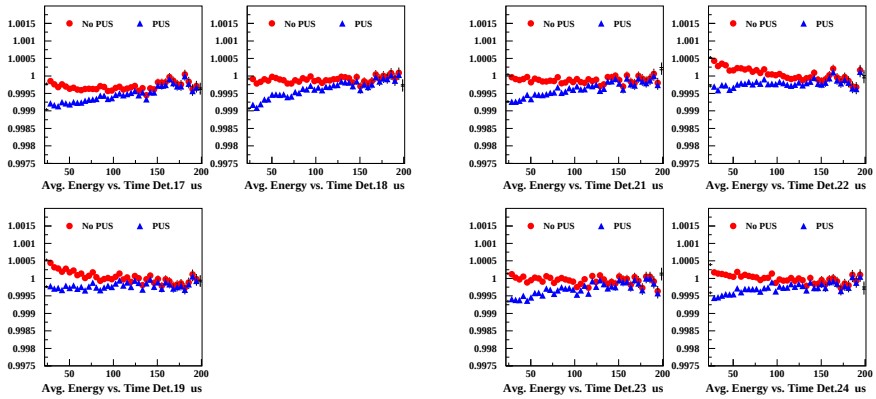

(a) Detectors 17-19.

(b) Detectors 21-24.

Figure 2.16: Same as in Fig. 2.14.

by fitting the average energy vs. time plots to a polynomial. In practice, the order of the polynomial is chosen 'by eye' such that the function passes through all the data points. Applying the proper correction

$$E = \frac{E_{obs}}{1 + (f_g(t) - 1)/m} \tag{2.8}$$

to each pulse, we see in Figs. 2.18-2.20 a great improvement in the stability of the average energy vs. time. This implies that whatever is causing the changes in average energy vs. time has a dominantly linear effect on the energies of the pulses. If this were not the case, if the effect was non-linear, then applying a gain correction would not flatten out the average energy vs. time.

However, just because the gain correction manages to flatten out the average energy vs. time of the decay electrons, this does not necessarily mean that applying the gain correction is the proper thing to do. A better judge of whether or not one should make the correction is the time spectrum itself, or rather, the fits to the time spectrum.

Fig. 2.21 shows the fit $\chi^2/d.o.f.$ for detector 25 when applying a -1x correction (red), no correction (blue) and a 1x correction (blue). We see that for the low n-value data set that there is a significant improvement in the fit $\chi^2/d.o.f.$ when we apply the gain correction. The improvement is considerably smaller for the high n-value data set. As expected, the fits get significantly worse when we magnify the gain in the data by applying a -1x correction.

Another parameter to investigate is the asymmetry. Since asymmetry is energy dependent, the fit asymmetry will not be constant versus fit time if the average energy vs. time is changing. We see in Fig. 2.22 that when we do not apply the correction (middle plots) the fit asymmetry is more or less stable

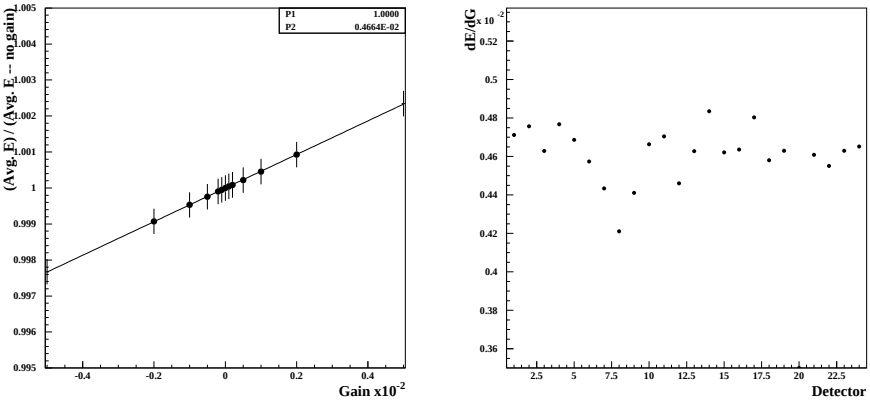

(a) The effect of gain on the average energy for detector 10.

(b) Slope of average energy vs. gain for each detector.

Figure 2.17: To determine the sensitivity of average energy to gain, artificial gains were applied to the data.

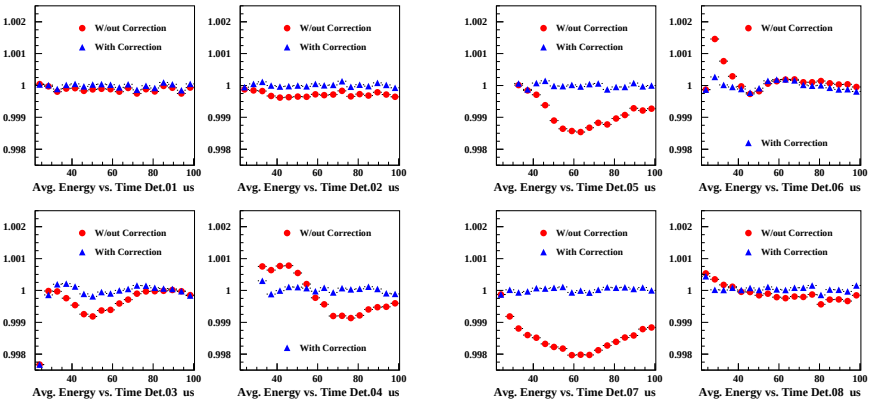

(a) Detectors 1-4.

(b) Detectors 5-8.

Figure 2.18: Pileup-subtracted average energy vs. time before (red circles) and after (blue triangles) an energy-scale correction was applied.

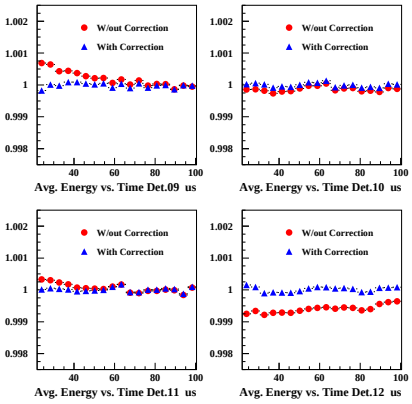

(a) Detectors 9-12.

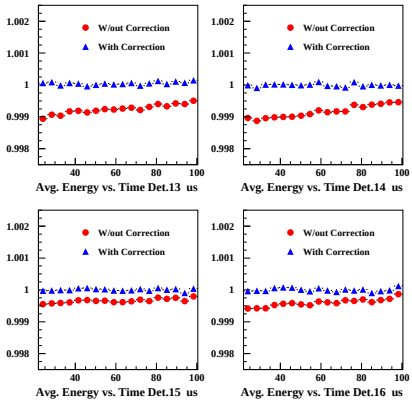

(b) Detectors 13-16.

Figure 2.19: Same as Fig. 2.18

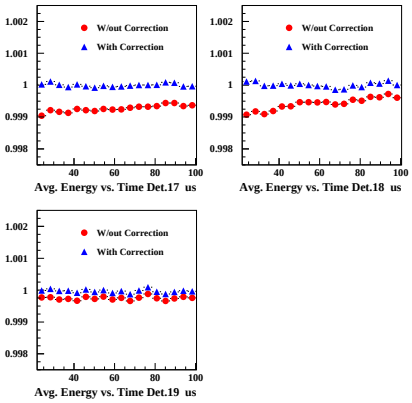

(a) Detectors 17-19.

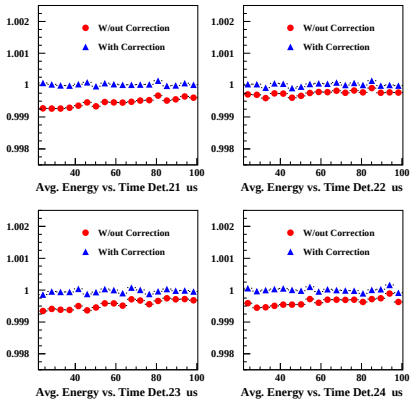

(b) Detectors 21-24.

Figure 2.20: Same as Fig. 2.18

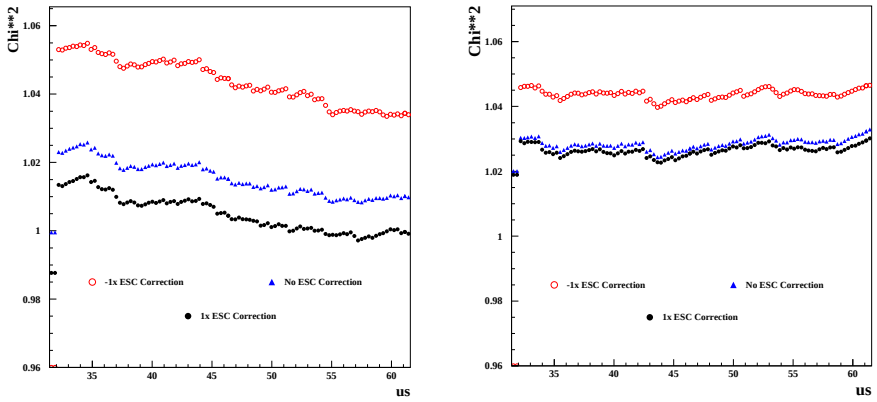

(a) Low n-value data.

(b) High n-value data.

Figure 2.21: Comparison of fit $\chi^2/d.o.f.$ vs. fit time between between uncorrected and gain-corrected data.

vs. time, however it does trend downward over time. When the correction is applied (bottom plots), the asymmetry is still more or less stable vs. time, but now it trends upwardward over time. The trend upward is also consistent with expectations from low-energy pileup.

Based on the facts that the average energy vs. time is constant, the fit $\chi^2/d.o.f.$ improves and the fit asymmetry is flat vs. time after we apply a gain correction to the data, we therefore will use gain-corrected data to obtain our final fit values for R. A systematic error due to uncertainties in the corrections will be determined later (see Section 3.2).

2.5 Fast Rotation and Fill Randomization

Because the muon beam is produced and injected in bunches of width $\sim$ 20 ns from the AGS, the stored muons are not distributed uniformly around the storage ring immediately after injection. However, within 50 μs however the injected beam 'debunches' and the bunch-structure of the injected muon beam is greatly diminished. Debunching occurs because the slower muons actually catch up to the faster muons, since the slower muons are at smaller average radii than the faster muons, and the actual difference in velocity is very small. The counting rate of the decay electrons is therefore modified to be (assuming the simple five-parameter function for counting rate):

$$N(t) = N_5(t) * f_{fr}(t) \tag{2.9}$$

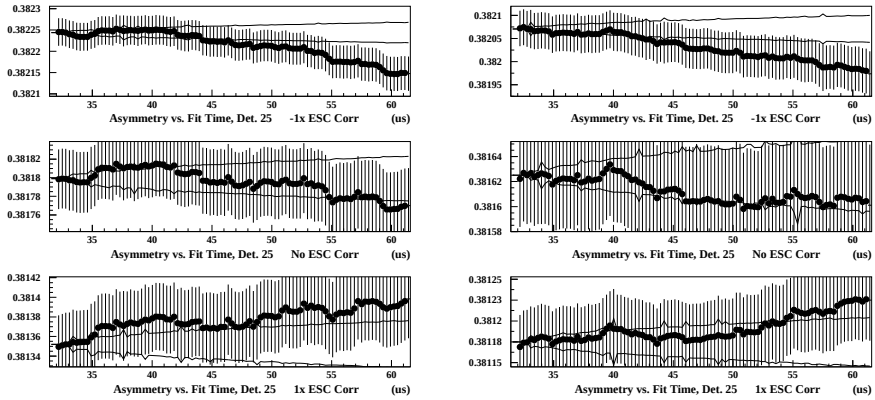

(a) Low n-value data.

(b) High n-value data.

Figure 2.22: Comparison of fit asymmetry vs. fit time between uncorrected data sets (top) and gain-corrected data sets (bottom).

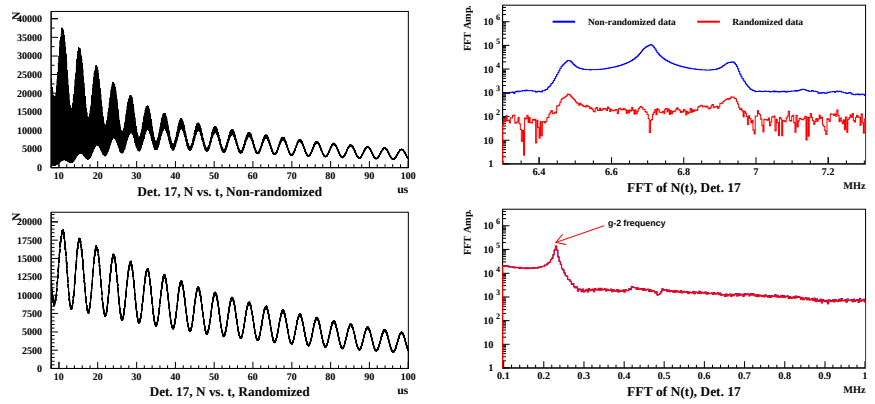

(a) Time spectra of non-randomized data (top) and randomized data (bottom) for detector 17.

(b) FFT spectra of non-randomized data (blue) and randomized data (red) for detector 17.

Figure 2.23: Comparison of time and frequency spectra of fill-randomized data and non-randomized data.

where

$$f_{fr}(t) = A_{fr}(t) * \cos(\omega_{cyc}t + \phi_{cyc}) \tag{2.10}$$

where fr stands for 'fast-rotation', $A_{fr}(t)$ describes the decaying envelope of the bunched structure of the muons in the storage ring, and ω_{fr} is the fast-rotation, or cyclotron, frequency. However, because the cyclotron frequency is so much higher than that of the g-2 frequency, instead of modifying our fit function we can effectively filter out the cyclotron frequency from the data. This is done by randomizing the time for T0 in each fill. The cyclotron period is very close to 149.185 ns, therefore adding random times generated from a uniform distribution between -74.5925 to +74.5925 ns for each fill washes out the fast rotation signal. Fig. 2.23 shows the FFT of the time spectra of the data from detector 17, which is gated on very early after injection, between 0 and 200 μs and of a binwidth of 5 ns, with and without randomization. We see that the amplitude of the fast rotation peak is reduced by 3 orders of magnitude, whereas the amplitude of the g-2 frequency component is unaltered by the fill randomization procedure. In the end, five histograms are built with different random numbers in each fill, and the results of the final value for R is taken from the average of the 5 fits.

Because randomization is so effective in removing the fast rotation component in the time spectrum, one may in fact use this process to eliminate all other effects on the counting rate, including muon lifetime, g-2, CBO, and muon decay, by taking the ratio of the non-randomized time spectrum to the randomized time spectrum; this leaves only the fast rotation in the time spectrum. Such a ratio is shown in the top plots of Fig. 2.24, where on the left the fast rotation function for detector 17, $f_{fr}(t)$, is plotted from 8-100 μs, which shows the envelope of the fast rotation oscillations, and on the right it is plotted from 10-12 μs which shows the oscillations themselves. The FFT amplitudes of this time spectrum, from 0-200 μs is shown in the bottom plots of Fig. 2.24. On the bottom left the FFT amplitudes in the range 6.3-7.15 MHz are plotted, and a very sharp peak is seen at the fast rotation frequency. This peak is much sharper than the peak obtained in Fig. 2.23, since the muon lifetime, which is the main contributor to the width of the peak in Fig. 2.23 is divided out. On the bottom right of Fig. 2.24 the FFT amplitudes in the frequency range 0.1-0.95 MHz are plotted, and we see that there is no g-2 frequency peak. Although this approach to obtaining the fast rotation frequency was not used in this analysis, this approach may be a very useful tool for the fast rotation analysis, which gives us the radial distribution of the stored muons.

2.6 Histogram Filling and Fit Procedure

The time of the decay electron is obtained by the following formula:

$$\begin{aligned} time_i &= (int((\texttt{TSTART}_i + \texttt{TOFFSET} + 0.5)2.5) * 2.5 - \\ &\quad \texttt{TOFFSET} + \texttt{FITTIME}_i - \texttt{TOMEAN} + \end{aligned}$$

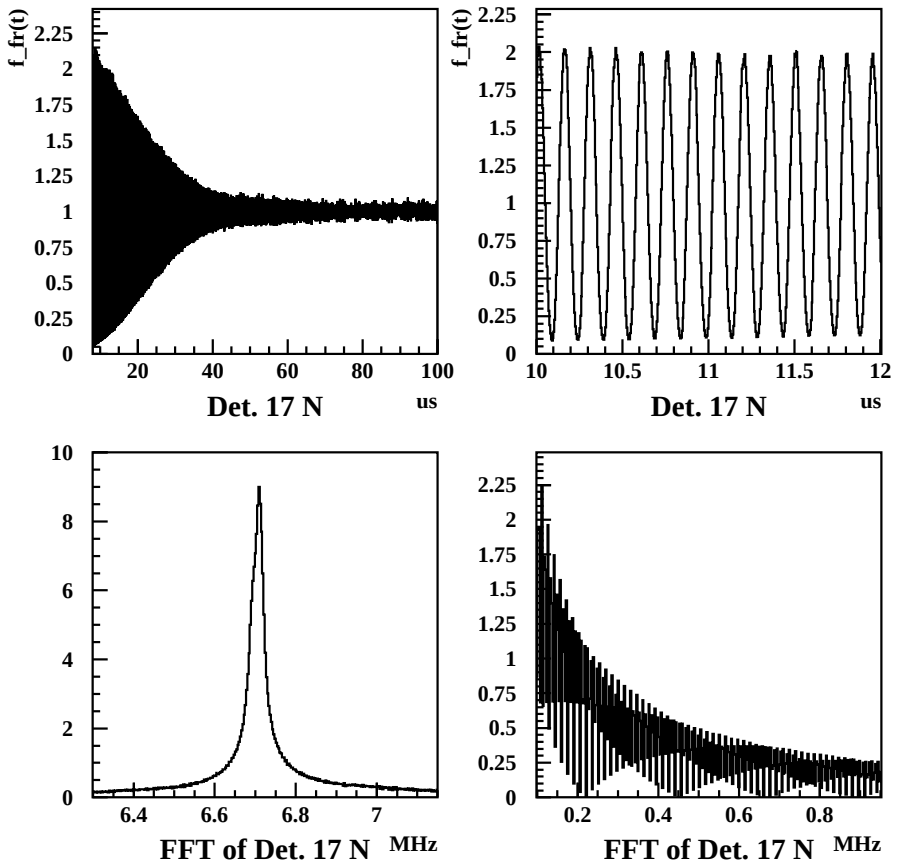

Figure 2.24: Top Left: Ratio of non-randomized time spectrum to the randomized time spectrum of detector 17 from 8-100 μs after injection. Top Right: Same as on left, but from 10-12 μs. Bottom Left: FFT of the ratio time spectrum above from 0-200 μs in the frequency range 6.3-7.15 MHz. The sharp peak is that of the fast rotation frequency. Bottom Right: Same as on left, but in the frequency range 0.1-0.95 MHz. Note that the g-2 frequency has been effectively divided out.

$$t_{shift} + t_{rand})/1000. \tag{2.11}$$

where `TSTART, TOFFSET, FITTIME`, and `TOMEAN` are variables from the `g2off` production are of `REAL` precision. `DOUBLE PRECISION` in the time of the pulse is obtained from the first line of Eq. 2.11. All other variables and numbers are of double precision. t_{shift} is a double precision variable that adjusts the pulse times for differences in cable lengths, and t_{rand} is a fill-dependent random time between -74.5925 to +74.5925 ns that washes out the fast-rotation structure of the data.

The ratio method requires four time spectra to be built, therefore a random integer between 0 and 3 is generated from a normal distribution obtained using the `RANLUX` routine at luxury level 4. The four number 0, 1, 2, and 3 determine into which of the four histograms the pulse time gets inserted: if it is 0, the pulse time gets shift by +1/2 the g-2 period and is inserted into the u_+ histogram, if is 1 the pulse time is shifted by -1/2 the g-2 period and is inserted into the u_- histogram, and if it is either 2 or 3, the pulse time is not shifted and is inserted to either the v_1 or the v_2 histogram respectively.

The u_+, u_-, v_1, and v_2 time spectra are later summed over runs, and then the ratio time spectra are built.

Since the g-2 phase is energy dependent, the detectors do not necessarily have all the same phase. We therefore should align the detectors so that they are all in phase. To accomplish this, we fit the ratio time spectra to the 3 parameter ratio function and obtain the fit parameters as a function of fit start time. We then obtain the phases of each detector by fitting a constant to phase vs. fit start time after 100 μs. The results of these fits are shown in table 2.2. All phases are quite close to π which seems like a reasonable phase to align the detectors to. Therefore, we build new time spectra, however this time the times of the pulses are adjusted such that

$$time'_i = time_i + \frac{\phi_{fit} - \pi}{\omega_a}. \tag{2.12}$$

where $time_i$ is defined by Eq. 2.11.

To fit the ratio time spectra, the `CERNLIB` routine `MINUIT` is used with the following commands:

(1) `migrad`

(2) `improve`

(3) `minos`

(4) `migrad`

The command `migrad` minimizes the function with "the most efficient and complete single method" [4]. `Improve` searches "for additional distinct local minima" [4], and `minos` performs a very reliable error analysis calculation which takes "account of non-linearities in the problem as well as parameter correlations..." [4].

Phase vs. Detector					
Det.	**Phase**	**Det.**	**Phase**	**Det.**	**Phase**
01	3.068692	09	3.068926	17	3.064036
02	3.072004	10	3.070950	18	3.072648
03	3.076609	11	3.068810	19	3.062937
04	3.085156	12	3.073176	20	———
05	3.090871	13	3.073592	21	3.064160
06	3.075665	14	3.069421	22	3.062883
07	3.089982	15	3.067344	23	3.068196
08	3.068110	16	3.068527	24	3.066248

Table 2.2: Phase vs. detector. These were initially obtained in order to align the detectors so they are all in-phase.

2.7 Ratio Fit Results

3 Parameter Ratio Fit

The data were fit to Eqn. [A.20],

$$r_3(t) = A_a \cos(2\pi f_a(1 - (R - R_{off}) \times 10^{-6})t + \phi_a) - C_1 \tag{2.13}$$

where $f_a = 229.067$ kHz. R_{off} is an offset known only to the analyzer, used to ensure a blind analysis of a_μ. R and fit χ^2 vs. Detector with a fit start time of $32.5\mu s$ are shown in Fig. 2.25 for the low and high n-value data sets on the left and right respectively. The first 24 detectors in the R vs. detector plot is fit to a constant, which gives the average R value over the 23 detectors. Detector 20, ignored in the 2001 analysis, is set to $R = 0$ and $\delta R = 0$; this has no effect on the fit to a straight line, since with $\delta R = 0$, it's R value has no weight. The resulting average R values for the low and high n-value data sets respectively are 107.6 ± 0.94 ppm and 109.2 ± 1.17 ppm, where the error is obtained from the fit to a constant.

To get a better view of what happens when we **don't** fit for CBO, R vs. fit start time for the sum of detectors 1-12 (detector 26), 13-24 (detector 27), and 1-24 (detector 25), where detector 20 is always excluded, is shown in Fig. 2.26. For the low n-value data set, we see that from about 30 to 100 μs, the R-values for both halves of the ring track quite well, the biggest differences being near 38, 50 and 80 μs. The fit R-values of the two different data sets does seem to diverge around 100 μs, however they later converge around 200 μs, so this is most likely a statistical effect. However, for the high n-value data set, there is quite a large difference ($\sim$ 3 ppm) in the R-values for the two halves of the ring at all fit start times. By splitting the high n-value data set up into various subsets, fitting the subsets and looking at the differences between the fit R values of the first and second halves of the ring, Peter Shagin has demonstrated that this 3 ppm difference is very likely a statistical effect. We also see oscillations of roughly 30 kHz in both data sets; this is most easily seen by looking at the difference

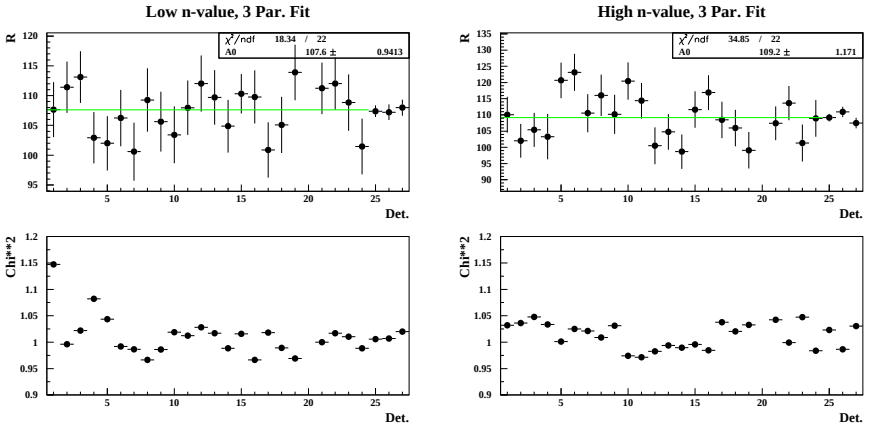

(a) Low n-value data set.

(b) High n-value data set.

Figure 2.25: Top: R vs. Detector for the 3 parameter fit. Bottom: Fit $\chi^2/d.o.f.$ for each detector for the 3 parameter fit. All points are taken at t=32.5 μs.

between R vs. fit start time of the two halves of the ring, the bottom plots in Fig. 2.26. This is the difference $f_{CBO} - 2f_{g-2}$. This leaves one with little doubt that CBO must be fit for or otherwise dealt with in both data sets.

Fig. 2.27 shows the fit asymmetry for detector 25 vs. fit starttime, and the $\chi^2/d.o.f.$ vs. fit start time for detectors 25-27.

5 Parameter Ratio Fit

In this fit we neglect the effect of CBO on the asymmetry and phase, and calculate the ratio by writing out explicitly the function:

$$r_5(t) = \frac{2f_0(t) - f_+(t) - f_-(t)}{2f_0(t) + f_+(t) + f_-(t)} \tag{2.14}$$

where

$$f_0(t) = (1 + e^{-t/\tau_c} A_{N_c} \cos(\omega_c t + \phi_c))(1 + A\cos(\omega_a t + \phi_a)) \tag{2.15}$$

and

$$f_\pm(t) = (1 + e^{-t'/\tau_c} A_{N_c} \cos(\omega_c t' + \phi_c)) e^{\mp T/(2\tau)} (1 + A\cos(\omega_a t' + \phi_a)) \tag{2.16}$$

where t' is the shifted time

$$t' = t \pm T/2, \tag{2.17}$$

$$\omega_a = 2\pi f_a (1 - (R - R_{off}) \times 10^{-6}), \tag{2.18}$$

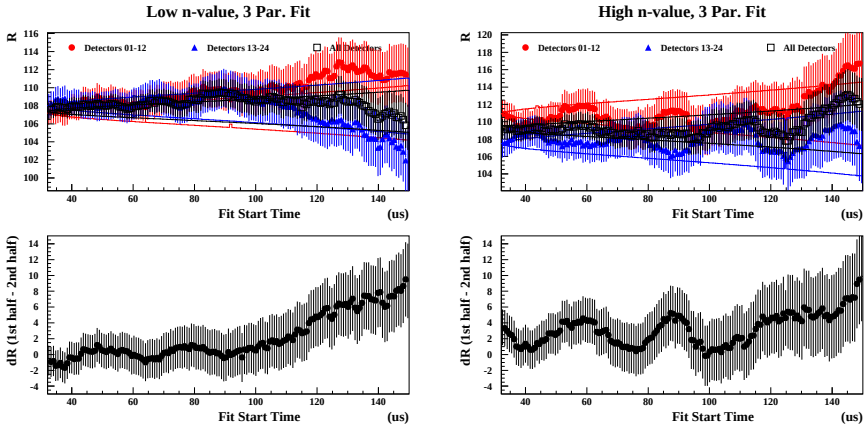

(a) Low n-value data set.

(b) High n-value data set.

Figure 2.26: Top: R vs. fit start time for the 3 parameter fit for different combinations of detectors: 1-12 (red circles), 13-24 (blue triangles), and 1-24 (black squares). Bottom: Difference of R vs. fit start time plots between first and second halves of the ring.

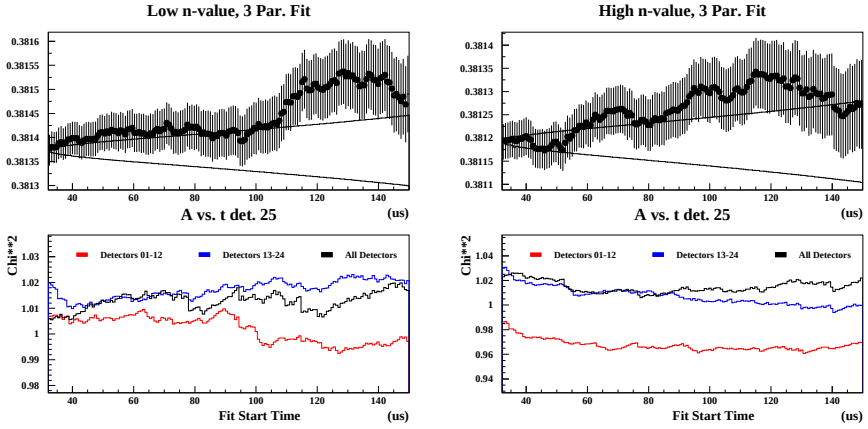

(a) Low n-value data set.

(b) High n-value data set.

Figure 2.27: Top: Asymmetry vs. fit start time for detector 25 for the 3 parameter fit. Bottom: $\chi^2/d.o.f$ vs. fit start time (bottom) for different combinations of detectors for the 3 parameter fit.

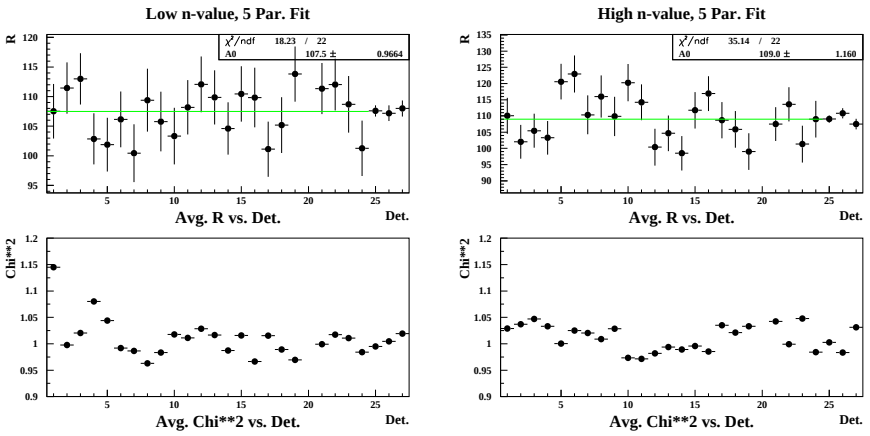

(a) Low n-value data set.

(b) High n-value data set.

Figure 2.28: Top: R vs. Detector for the 5 parameter fit. Bottom: Fit $\chi^2/d.o.f.$ for each detector for the 5 parameter fit. All points are taken at t=32.5 μs.

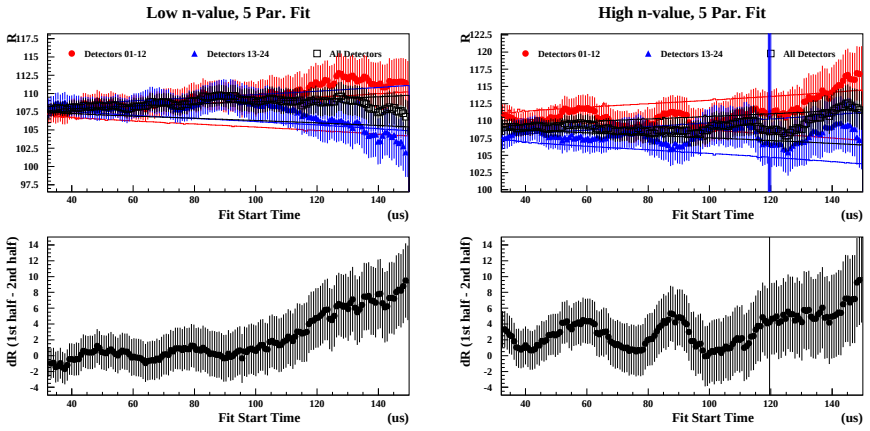

(a) Low n-value data set.

(b) High n-value data set.

Figure 2.29: Top: R vs. fit start time for the 5 parameter fit for different combinations of detectors: 1-12 (red circles), 13-24 (blue triangles), and 1-24 (black squares). Bottom: Difference of R vs. fit start time plots between first and second halves of the ring.

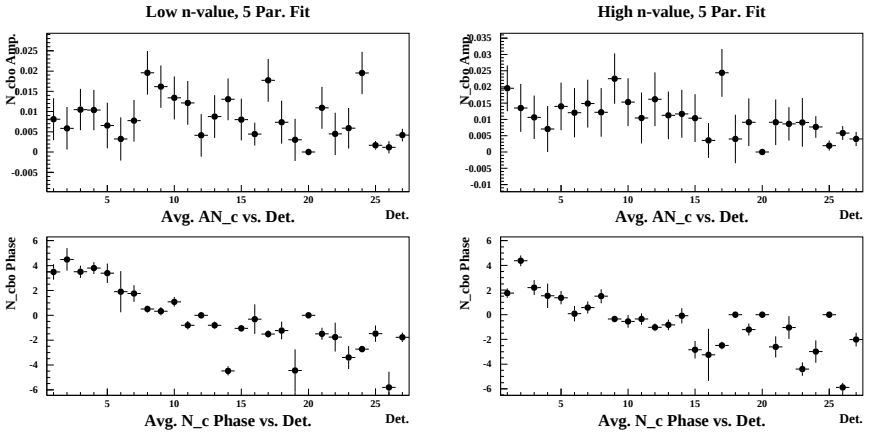

(a) Low n-value data set.

(b) High n-value data set.

Figure 2.30: CBO amplitude (top) and phase (bottome) vs. detector for the 5 parameter ratio fit.

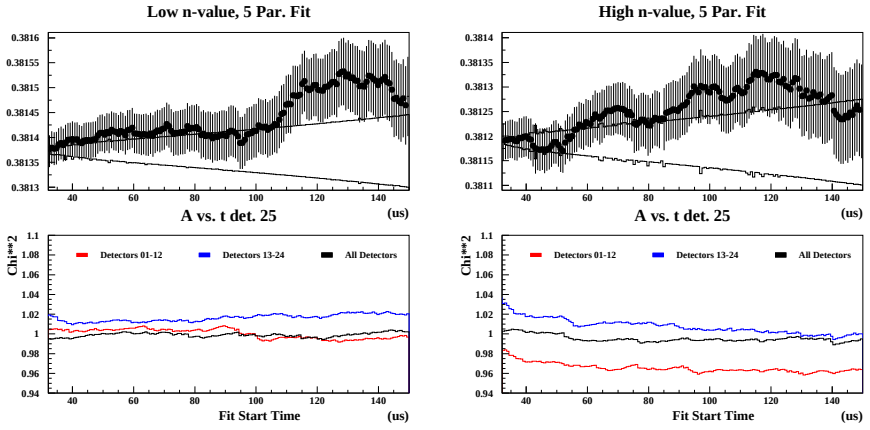

(a) Low n-value data set.

(b) High n-value data set.

Figure 2.31: Asymmetry vs. fit start time for detector 25 (top) and $\chi^2/d.o.f$ vs. fit start time (bottom) for different combinations of detectors for the 5 parameter fit.

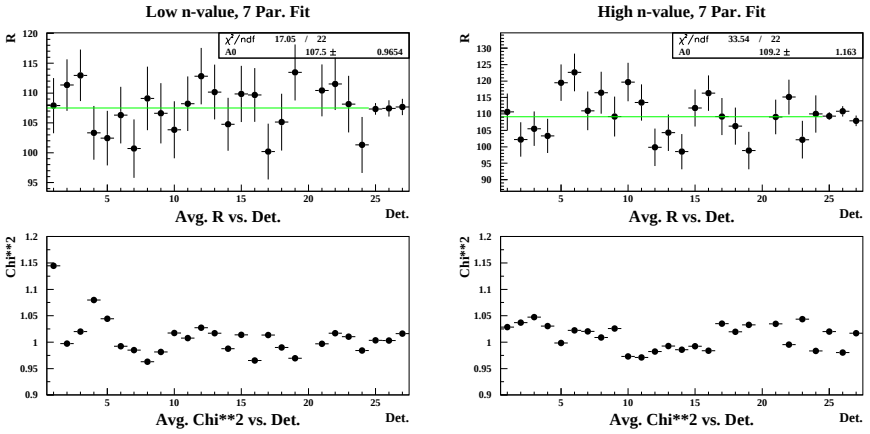

(a) Low n-value data set.

(b) High n-value data set.

Figure 2.32: R vs. Detector for the 7 parameter ratio fit. Left: Low n-value data set. Right: High n-value data set. All points are taken at t=32.5 μs.

as before, τ is the dilated muon lifetime fixed to 64.4 μs, A_{N_c} is the amplitude of the CBO effect on N, and ϕ_c is the CBO phase. The CBO frequencies and lifetimes were fixed to the values determined in Section 2.2: 419.1 kHz and 92.1 μs for the low n-value data set and 490.6 kHz and 130.1 μs for the high n-value data set.

Fig. 2.28 shows R vs. detector for the two data sets. The fitted values for average R at 32.5 μs are very consistent with those obtained from the three parameter fit. In fact, comparing all plots from the 3 parameter fits to those from the 5 parameter fits, we see no real difference between the two.

CBO amplitudes and phases vs. detector with a fit start time of 32.5μs are shown in Fig. 2.30. As expected, the CBO phase changes from detector to detector, traversing 2π radians from the first to last detector. The difference in phase between detectors is not exactly equal to $2\pi/24$, which we understand to be due to differences in geometrical acceptances for each detector and of course statistical fluctuations. However, although reasonable values for the CBO parameters were obtained in the fits, it is still quite clear that the functional form of the fit is not quite right, since we still see the $\sim$ 30 kHz oscillations in Fig. 2.29 that we saw in the three parameter ratio fits.

Again, asymmetry and $\chi^2/d.o.f.$ vs. fit start time is shown in Fig. 2.31.

7 Parameter Ratio Fit

The data were fit to the function:

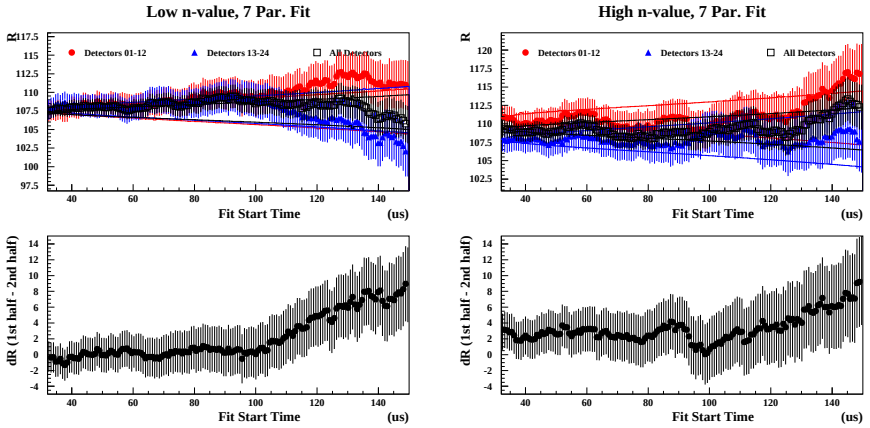

(a) Low n-value data set.

(b) High n-value data set.

Figure 2.33: R vs. Fit Start Time for the 7 parameter ratio fit.

$$r_7(t) = \frac{2f_0(t) - f_+(t) - f_-(t)}{2f_0(t) + f_+(t) + f_-(t)} \tag{2.19}$$

where

$$f_0(t) = (1 + A_{N_c}(t))(1 + A(1 + A_{A_c}(t)) \cos(\omega_a t + \phi_a)) \tag{2.20}$$

and

$$f_\pm(t) = (1 + A_{N_c}(t'))e^{\mp T/(2\tau)}(1 + A(1 + A_{A_c}(t')) \cos(\omega_a t' + \phi_a)) \tag{2.21}$$

where t' is the shifted time

$$t' = t \pm T/2, \tag{2.22}$$

$$\omega_a = 2\pi f_a(1 - (R - R_{off}) \times 10^{-6}), \tag{2.23}$$

as before, τ is the dilated muon lifetime fixed to 64.4 μs,

$$A_{N_c}(t) = A_{N_c} e^{-t/\tau_c} \cos(\omega_c t + \phi_{N_c}) \tag{2.24}$$

is the amplitude of the CBO effect on N, and

$$A_{A_c}(t) = A_{A_c} e^{-t/\tau_c} \cos(\omega_c t + \phi_{A_c}) \tag{2.25}$$

is the amplitude of the CBO effect on A. The CBO frequencies and lifetimes are fixed to the same values used in the five-parameter ratio fit.

The fit results for R, χ^2, N_c and A_c are shown in Figs. 2.32-2.36. With regards to CBO, the results from these fits are much improved over the 3 and

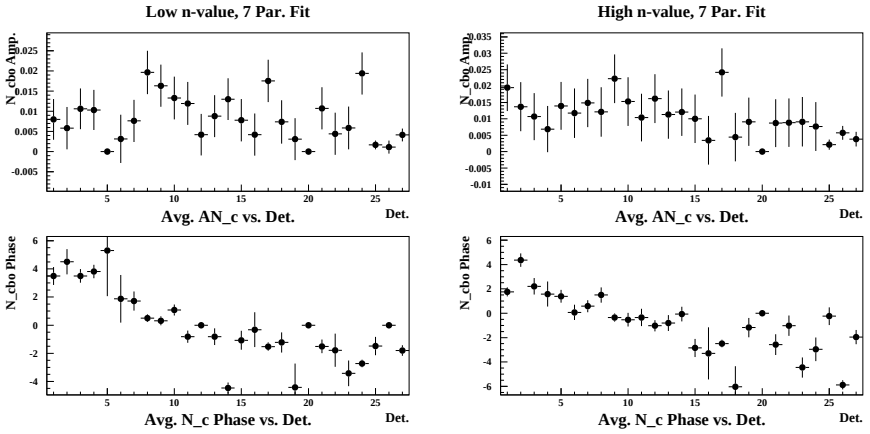

(a) Low n-value data set.

(b) High n-value data set.

Figure 2.34: N_c amplitudes and phases vs. Detector for the 7 parameter ratio fit.

5 parameter fits. The amplitude of the half-ring effect, as seen in the difference between the R vs. fit time of the two halves of the ring is greatly diminished (see Fig. 2.32). And again, as expected, ϕ_{N_c} and ϕ_{A_c} both traverse 2π radians over the circumference of the storage ring.

9 Parameter Ratio Fit

Although the seven-parameter ratio function seems to effectively eliminate the "half-ring" effect, we know from past experience of another CBO term that may be necessary to fit for: the effect of CBO on the g-2 phase. Thus, the data were fit to the function:

$$r_9(t) = \frac{2f_0(t) - f_+(t) - f_-(t)}{2f_0(t) + f_+(t) + f_-(t)} \tag{2.26}$$

where

$$f_0(t) = (1 + A_{N_c}(t))(1 + A(1 + A_{A_c}(t))\cos(\omega_a t + \phi_a(1 + A_{\phi_c}(t)))) \tag{2.27}$$

and

$$f_\pm(t) = (1 + A_{N_c}(t'))e^{\mp T/(2\tau)}(1 + A(1 + A_{A_c}(t'))\cos(\omega_a t' + \phi_a(1 + A_{\phi_c}(t')))) \tag{2.28}$$

where t' is the shifted time

$$t' = t \pm T/2, \tag{2.29}$$

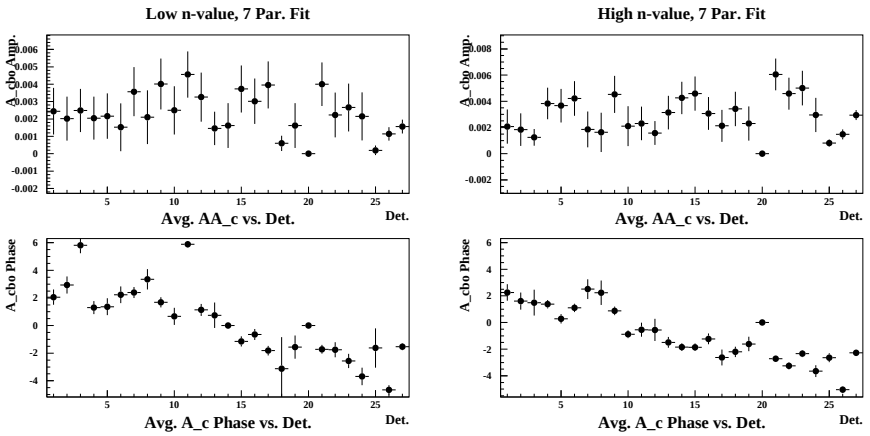

(a) Low n-value data set.

(b) High n-value data set.

Figure 2.35: A_c term amplitudes and phases vs. Detector for the 7 parameter ratio fit.

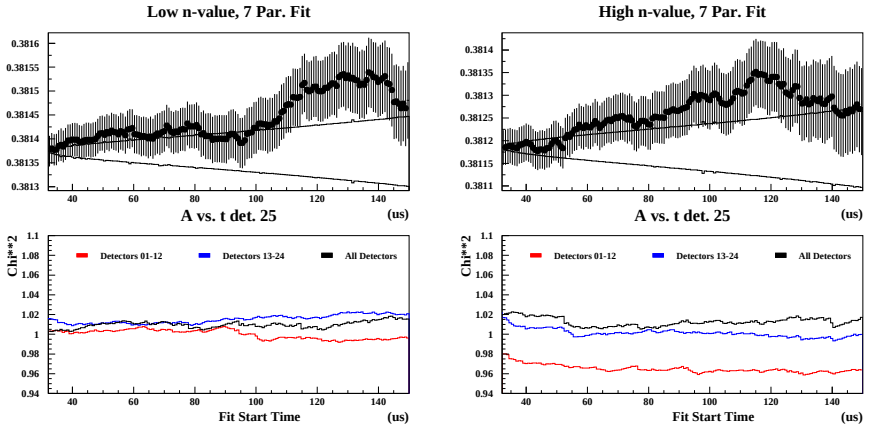

(a) Low n-value data set.

(b) High n-value data set.

Figure 2.36: Asymmetry vs. fit start time for detector 25 (top) and $\chi^2/d.o.f$ vs. fit start time (bottom) for different combinations of detectors for the 7 parameter fit.

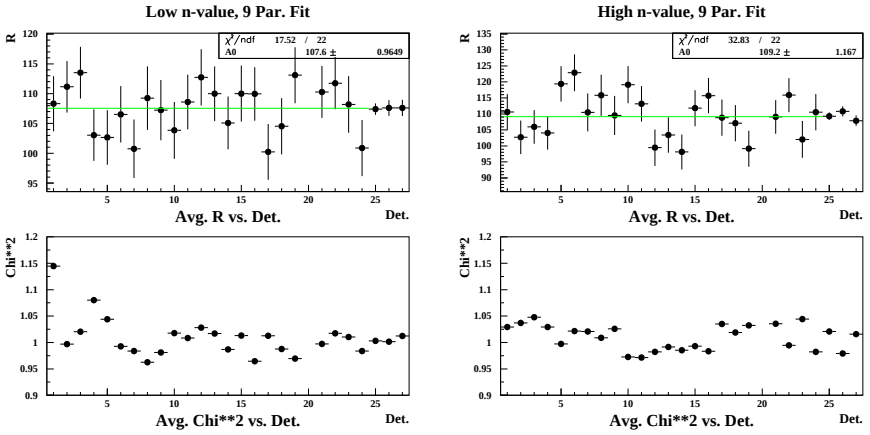

(a) Low n-value data set.

(b) High n-value data set.

Figure 2.37: R vs. Detector for the 9 parameter fit. All points are taken at t=32.5 μs.

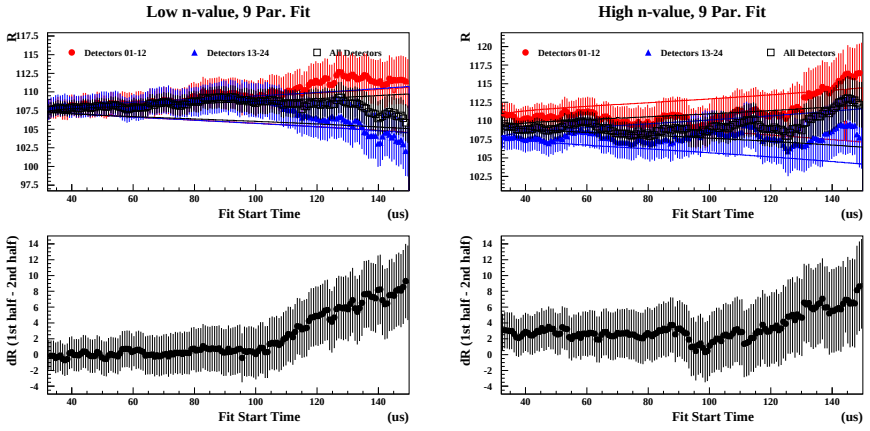

(a) Low n-value data set.

(b) High n-value data set.

Figure 2.38: R vs. Fit Start Time for the 9 parameter fit.

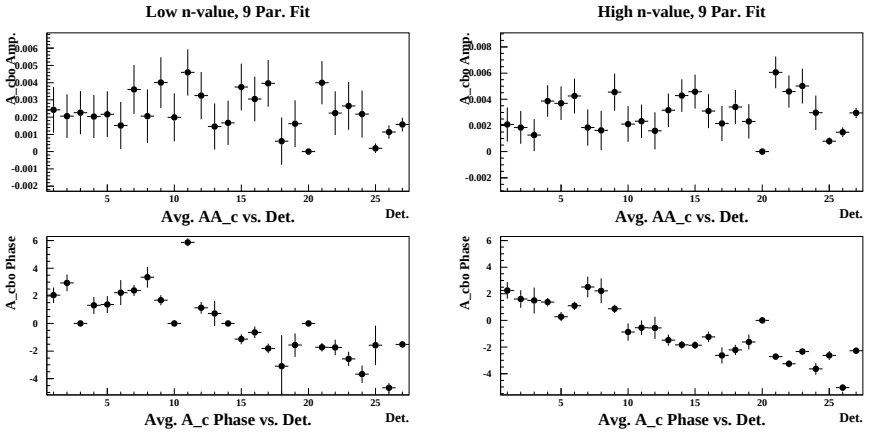

(a) Low n-value data set.

(b) High n-value data set.

Figure 2.39: A_c term amplitudes and phases vs. Detector for the 9 parameter fit. All points are taken at t=32.5 μs.

$$\omega_a = 2\pi f_a(1 - (R - R_{off}) \times 10^{-6}), \tag{2.30}$$

as before, τ is the dilated muon lifetime fixed to 64.4 μs,

$$A_{N_c}(t) = A_{N_c} e^{-t/\tau_c} \cos(\omega_c t + \phi_{N_c}) \tag{2.31}$$

is the CBO effect on N,

$$A_{A_c}(t) = A_{A_c} e^{-t/\tau_c} \cos(\omega_c t + \phi_{A_c}) \tag{2.32}$$

is the CBO effect on A, and

$$A_{\phi_c}(t) = A_{\phi_c} e^{-t/\tau_c} \cos(\omega_c t + \phi_{\phi_c}) \tag{2.33}$$

is the CBO effect on ϕ_a. Once again, the CBO frequencies and lifetimes are fixed to the same values used in the five- and seven-parameter ratio fits.

The results of the fits are shown in Figs. 2.37-2.41, and are very compatible with the fit results obtained from the 7-parameter ratio function. Fig. 2.38 shows that the half-ring effect is also effectively removed by the 9-parameter ratio function.

Fit Results with Different Fit Start Times

Because the detectors closest to the injection point see the largest flash, the PMTs of these detectors are gated on almost 25 μs later than the PMTs of the detectors on the opposite side of the ring. If one wishes to combine the time

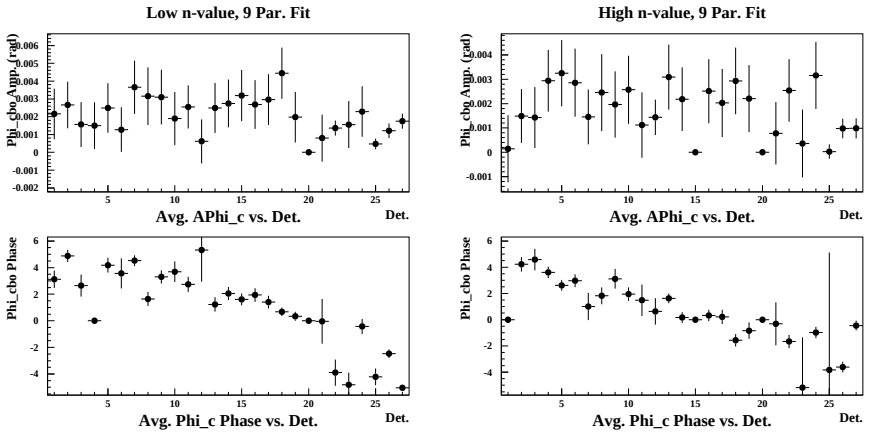

(a) Low n-value data set.

(b) High n-value data set.

Figure 2.40: ϕ_c term amplitudes and phases vs. Detector for the 9 parameter fit. All points are taken at t=32.5 μs.

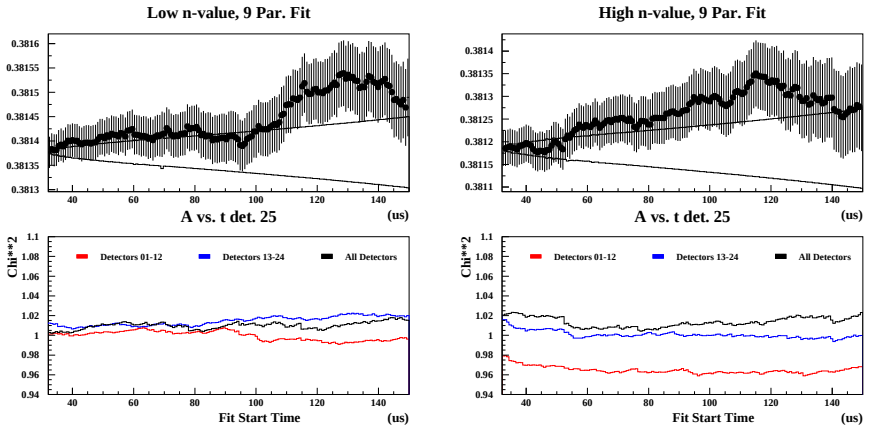

(a) Low n-value data set.

(b) High n-value data set.

Figure 2.41: Asymmetry vs. fit start time for detector 25 (top) and $\chi^2/d.o.f$ vs. fit start time (bottom) for different combinations of detectors for the 9 parameter fit.

Fit Start Time					
Det.	1,8	2	3,6,7	4,5	9-24
Time (μs)	27.4	25.3	29.6	34.0	23.0

Table 2.3: Fit start times for the individual detectors. All fit start times are after scraping and at (or very close to) g-2 zero crossings.

spectra from all of the detectors into one time spectrum (ie: that of detector 25), then the earliest one may begin to fit the data is $\sim 32\mu s$ after injection. One can gain more statistics however if the detectors are fit individually using different fit start times; at the end one simply takes the weighted average value of R from the distribution of R's obtained from the individual detectors. This of course requires that the fit does not rely on cancelling CBO by fitting the sum of detectors, and therefore only a 7 or 9 parameter fit function is appropriate for this approach. Nevertheless, for completeness, we show R vs. detector with different fit start times for all fit functions (3-, 5-, 7- and 9-parameter) in Figures 2.42 and 2.43. The average values of R for each fit is obtained by fitting a constant to the 24 detectors. Note that although the fit values of R vary only very slightly vs. fit function, the fit $\chi^2/d.o.f.$ improves significantly as more and more CBO effects are fit for, going from the 3-parameter ratio function to the 9-parameter ratio function.

The individual fit start times were determined according to the following criteria:

- $\chi^2/d.o.f.$ is 'acceptable'
- fit parameters are stable
- $t_{fit} > 22\mu s$ (after scraping)
- t_{fit} is a g-2 zero crossing

The fit start times of the detectors are listed in Table 2.3. "Acceptable" $\chi^2/d.o.f.$ is defined as the point in time at which the $\chi^2/d.o.f.$ in the fit-time scan drops below 2.5 σ from 1 (therefore, $|\chi^2 - 1| < 0.05$). In the case of consistently high (greater than 2.5 σ from 1) $\chi^2/d.o.f.$ vs. fit time, an average $\chi^2/d.o.f.$ is determined from fit results between 90 and 150 μs, and "acceptable" $\chi^2/d.o.f.$ is defined as $|(\chi^2 - \chi^2_{late})/\chi^2_{late}| < 0.05$.

For any fit, assuming the fit function is correct, one expects a $\chi^2/N_{dof} = 1 \pm \sqrt{2/N_{dof}}$. In our case, $\sqrt{2/N_{dof}} \simeq 0.025$ (there are approximately 3300 bins and the number of fit parameters is relatively small). Therefore, averaging over N detectors, one expects a $< \chi^2 >= 1 \pm 0.025/\sqrt{N}$ or $< \chi^2 >= 1 \pm 0.0053$. Fig. 2.44 shows χ^2/dof vs. t for both data sets. At fit times $< 32\mu s$, detectors 1-8 are ignored, therefore there is a discontinuity at $32\mu s$ when these detectors are then taken into account. The horizontal green lines are the 1 σ band, the vertical green line are at 23 μs and 32 μs. There is in general good agreement ($< 1\sigma$ difference) between the average fit results and the expected values.

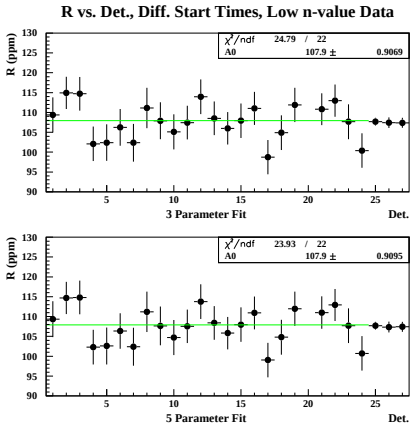

(a) 3 and 5 parameter ratio fits.

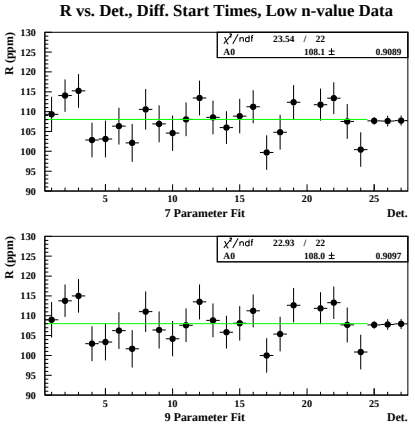

(b) 7 and 9 parameter ratio fits.

Figure 2.42: Fit result comparison of R vs. Det. for the low n-value data set using different fit start times for each detector.

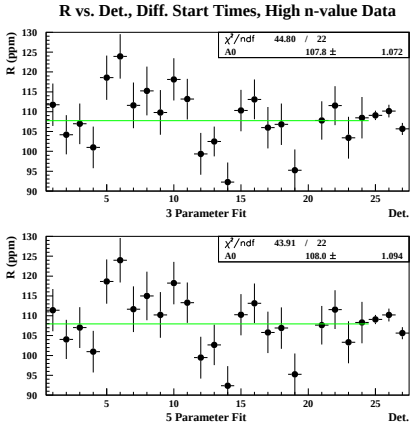

(a) 3 and 5 parameter ratio fits.

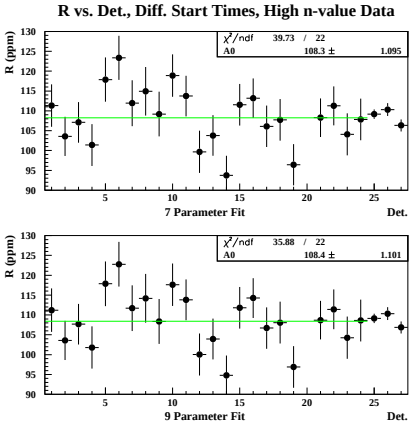

(b) 7 and 9 parameter ratio fits.

Figure 2.43: Fit result comparison of R vs. Det. for the high n-value data set using different fit start times for each detector.

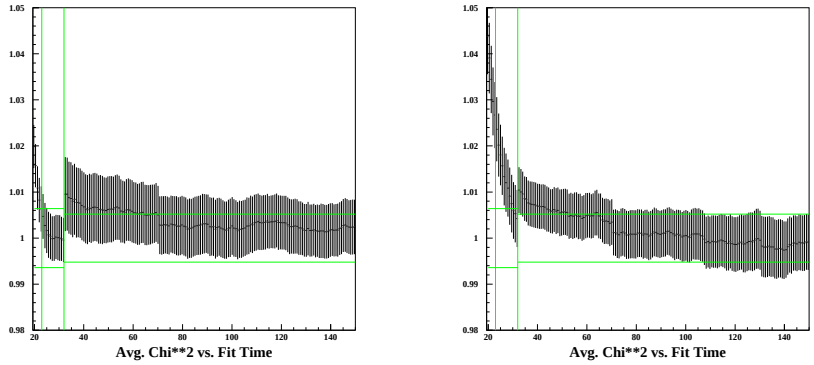

(a) Low-n data set.

(b) High-n data set.

Figure 2.44: $< \chi^2/dof >$ vs. t for both data sets. The average is over the detectors (15 detectors (9-24) from 20-32 μs, all 23 detectors from 32 μs on, hence the discontinuity at 32 μs. The horizontal green lines represent 1 σ bands, the vertical green lines are drawn at 23 and 32 μs after injection.

However, when averaging over detectors at different start times, there is a much larger discrepancy; in this case, $< \chi^2 >= 1.014 \pm 0.0081$ for the low-n data set, and $< \chi^2 >= 1.026 \pm 0.0052$ for the high-n data set. This is to be expected due to the nature of the chosen fit start times. At early fit start times the χ^2 is higher-but-still-acceptable than at later start times. Therefore, since over half of the detectors are used at much earlier start times, on average the χ^2 will be high. In fact, the width of the χ^2 distribution is very close to what it should be, only the mean is shifted. The reason for the large width in the χ^2 distribution for the low-n data set is primarily due to detector 1, which, for this data set, has a very high (but consistent vs. fit time) χ^2 of 1.15. If one were to ignore this detector, the average $\chi^2 = 1.008 \pm 0.0066$, in much better agreement with the expected width of 0.0042.

Summary of Fit Results

The data were fit to four different ratio functions, and many plots have been shown. Following are brief summaries of the fit parameters used in each fit (Table 2.4) and summaries of the resulting R values and fit χ^2's of each fit (Tables 2.5 and 2.6).

The final R value will be determined from fits to individual detectors at different start times, since the statistical error can be reduced by $\sim 7\%$. The question remains as to which function to use in the final analysis of the data:

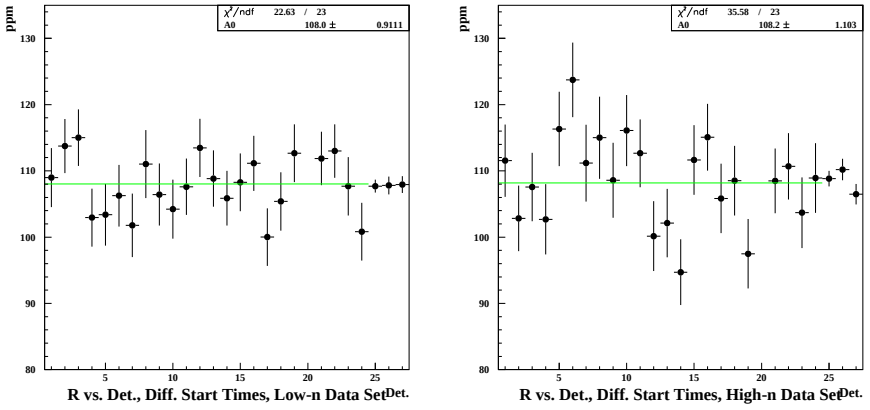

(a) Low-n data set.

(b) High-n data set.

Figure 2.45: R vs. Detector for the low- and high-n data sets, as determined using different start times for various detectors, using the 9-parameter ratio function, and correcting the error bars in the fits due to pileup subtraction. R vs. Detector is fit to a constant to determine the average value R. Results for only one random seed are shown.

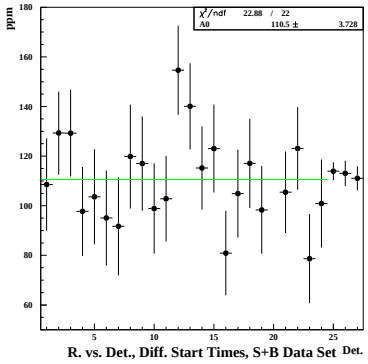

Figure 2.46: R vs. Detector for the S+B data set, as determined using different start times for various detectors, using the 9-parameter ratio function, and correcting the error bars in the fits due to pileup subtraction. R vs. Detector is fit to a constant to determine the average value R. Results for only one random seed are shown.

Fit Parameter Status				
Fit	3 Par.	5 Par.	7 Par.	9 Par.
A	Free	Free	Free	Free
R	Free	Free	Free	Free
ϕ	Free	Free	Free	Free
constant/ τ_μ	2.874×10^{-4}	64.4 μs	64.4 μs	64.4 μs
A_{N_c}	NA	Free	Free	Free
ϕ_{N_c}	NA	Free	Free	Free
A_{A_c}	NA	NA	Free	Free
ϕ_{A_c}	NA	NA	Free	Free
A_{ϕ_c}	NA	NA	NA	Free
ϕ_{ϕ_c}	NA	NA	NA	Free
f_{cbo} (low n)	NA	419.1 kHz	419.1 kHz	419.1 kHz
τ_{cbo} (low n)	NA	92.1 μs	92.1 μs	92.1 μs
f_{cbo} (high n)	NA	490.6 kHz	490.6 kHz	490.6 kHz
τ_{cbo} (high n)	NA	130.1 μs	130.1 μs	130.1 μs

Table 2.4: Summary of fit parameter status in each ratio fit. "Free" means that the parameter is left free in the `MINUIT` fit, number/values in an entry means that the fit parameter was held fixed to that value in the fit, and "NA" means not applicable.

clearly either the seven- or the nine-parameter ratio function must be used in order to effectively reduce the systematic error due to CBO. We base our decision to use the 9-parameter ratio function on three key points: a) simulation has shown the existence of the A_{ϕ_c} term, however small; b) the fit to a constant of R vs. detector obtained from the 9-parameter ratio fits has a better $\chi^2/d.o.f.$ than that obtained from the 7-parameter ratio fits (see Fig. 2.42); and c) there are no strong correlations between R and the other 8 fit parameters in the 9-parameter ratio function. Tables 2.7 and 2.8 show the correlation coefficient matrix of the nine parameters used in the 9-parameter ratio function, as determined by `Minuit`. We see that besides the g-2 phase, there are no other parameters that are strongly correlated to the g-2 frequency. This is an important and distinguishing feature of the fit function's ability to describe the data; in 2000, where the CBO frequency was much closer to twice the g-2 frequency, the CBO terms in the various fitting functions were more highly correlated to the g-2 frequency.

It was pointed out that neglecting corrections to error bars in the ratio time spectrum due to pileup subtraction (see, for example, [5]) can result in

Comparison of Fit R Values - Low n-value Data Set				
Fit	3 Par.	5 Par.	7 Par.	9 Par.
Avg. R @ 32.5 μs (fit to const.)	107.6 ± 0.94	107.5 ± .97	107.5 ± 0.97	107.6 ±0.96
$\chi^2/d.o.f.$ of fit to const.	0.833	0.828	0.775	0.796
Avg. $\chi^2/d.o.f.$ over detectors	1.011	1.010	1.010	1.010
$\sigma_{\chi^2/d.o.f.}$	0.039	0.038	0.039	0.039
Avg. R @ 32.5 μs for Det. 25	107.4 ±0.96	107.6 ± 0.95	107.3 ± 0.97	107.4 ± 0.97
$\chi^2/d.o.f.$	1.006	0.995	1.003	1.003
Avg. R @ diff. start times	107.9 ±0.91	107.9 ± 0.91	108.1 ± 0.91	108.0 ± 0.91
$\chi^2/d.o.f.$ of fit to const.	1.113	1.088	1.070	1.042
Avg. $\chi^2/d.o.f.$ over detectors	1.016	1.015	1.014	1.014
$\sigma_{\chi^2/d.o.f.}$	0.039	0.039	0.039	0.039

Table 2.5: Brief summary of the current results from the various functions fit to the low n-value data set. The $\chi^2/d.o.f.$ is from the result of fitting R vs. det. to a constant, whereas the average and $\sigma_{\chi^2/d.o.f.}$ are taken from the distribution of fit χ^2's from each detector.

a systematic error in R and change both R and the uncertainty on R by a small amount. All plots shown previously neglected these corrections. Instead of applying such a systematic error at the end, it was decided to do the χ^2 minimization as correctly as possible in the fits; therefore, the corrections to the errors were determined and applied (see Section A.4) fairly late-in-the-game. Indeed, the average R value changed by a small amount (0.06 ppm), and the statistical uncertainty on R changed by less than 0.5%. Figs. 2.45 show R vs. Detector using the 9-parameter ratio fit at different start times for the detectors with the error bar corrections applied. Determining R this way using five random seeds, we find for our final R-values: $R_{low-n} = 108.21 \pm 0.91$ ppm and $R_{high-n} = 108.42 \pm 1.10$ ppm. Fig. 2.46 is a similar plot of R vs. Detector for the "S+B" (silver + bronze runs) data set. Using five random seeds, we find $R_{SB} = 110.55 \pm 3.73$.

Comparison of Fit R Values - High n-value Data Set				
Fit	3 Par.	5 Par.	7 Par.	9 Par.
Avg. R @ 32.5 μs (fit to const.)	109.2 $\pm$1.17	109.0 $\pm$ 1.16	109.2 $\pm$ 1.16	109.2 $\pm$ 1.17
$\chi^2/d.o.f.$ of fit to const.	1.584	1.597	1.525	1.492
Avg. $\chi^2/d.o.f.$ over detectors	1.013	1.012	1.011	1.010
$\sigma_{\chi^2/d.o.f.}$	0.025	0.024	0.024	0.024
Avg. R @ 32.5 μs for Det. 25	109.2 $\pm$ 1.16	109.2 $\pm$ 1.13	109.3 $\pm$ 1.16	109.3 $\pm$ 1.17
$\chi^2/d.o.f.$	1.023	1.020	1.020	1.021
Avg. R @ diff. start times	107.8 $\pm$1.07	108.0 $\pm$ 1.09	108.3 $\pm$ 1.10	108.4 $\pm$ 1.10
$\chi^2/d.o.f.$ of fit to const.	2.036	1.996	1.806	1.631
Avg. $\chi^2/d.o.f.$ over detectors	1.029	1.028	1.026	1.026
$\sigma_{\chi^2/d.o.f.}$	0.026	0.025	0.025	0.025

Table 2.6: Brief summary of the current results from the various functions fit to the high n-value data set. The $\chi^2/d.o.f.$ is from the result of fitting R vs. det. to a constant, whereas the average and $\sigma_{\chi^2/d.o.f.}$ are taken from the distribution of fit χ^2's from each detector.

Correlation Matrix for 9 Parameter Fit, Low n-value									
Par.	A	R	ϕ_a	A_{N_c}	ϕ_{N_c}	A_{A_c}	ϕ_{A_c}	A_{ϕ_c}	ϕ_{ϕ_c}
A	1.000	-0.005	-0.007	0.000	0.013	0.049	-0.054	-0.046	0.045
R	-0.005	1.000	0.867	-0.024	0.001	0.051	0.041	-0.032	-0.033
ϕ_a	-0.007	0.867	1.000	-0.033	0.001	0.068	0.057	-0.042	-0.046
A_{N_c}	0.000	-0.024	-0.033	1.000	-0.005	0.002	-0.013	-0.006	0.006
ϕ_{N_c}	0.013	0.001	0.001	-0.005	1.000	0.009	0.000	0.010	0.002
A_{A_c}	0.049	0.051	0.068	0.002	0.009	1.000	0.001	-0.011	-0.012
ϕ_{A_c}	-0.054	0.041	0.057	-0.013	0.000	0.001	1.000	0.009	0.001
A_{ϕ_c}	-0.046	-0.032	-0.042	-0.006	0.010	-0.011	0.009	1.000	-0.004
ϕ_{ϕ_c}	0.045	-0.033	-0.046	0.006	0.002	-0.012	0.001	-0.004	1.000

Table 2.7: Correlation Matrix of the 9 fit parameters of the full physics function for the low n-value data set. Values are from the fit to detector 25, around 40 μs.

Correlation Matrix for 9 Parameter Fit, High n-value									
Par.	A	R	ϕ_a	A_{N_c}	ϕ_{N_c}	A_{A_c}	ϕ_{A_c}	A_{ϕ_c}	ϕ_{ϕ_c}
A	1.000	-0.001	0.000	0.004	-0.015	0.021	0.081	0.071	0.025
R	-0.001	1.000	0.861	0.007	0.014	-0.085	0.003	-0.041	0.067
ϕ_a	0.000	0.861	1.000	0.010	0.019	-0.114	0.007	-0.041	0.092
A_{N_c}	0.004	0.007	0.010	1.000	0.004	-0.013	0.027	-0.018	-0.021
ϕ_{N_c}	-0.015	0.014	0.019	0.004	1.000	-0.035	0.001	0.020	0.026
A_{A_c}	0.021	-0.085	-0.114	-0.013	-0.035	1.000	-0.005	-0.011	-0.016
ϕ_{A_c}	0.081	0.003	0.007	0.027	0.001	-0.005	1.000	-0.005	-0.007
A_{ϕ_c}	0.071	-0.041	-0.041	-0.018	0.020	-0.011	-0.005	1.000	0.070
ϕ_{ϕ_c}	0.025	0.067	0.092	-0.021	0.026	-0.016	-0.007	0.070	1.000

Table 2.8: Correlation Matrix of the 9 fit parameters of the full physics function for the high n-value data set. Values are from the fit to detector 25, around 40 μs.

Chapter 3

2001 Systematic Errors on ω_a

3.1 Energy Bin Analysis

An important check of our understanding of the data can be made by dividing the data up into energy bins. This allows us to see the energy-dependence of certain fit parameters, specifically the asymmetry and CBO parameters. Ideally the precession frequency, or R, is independent of the detected decay electron's energy.

The data were therefore divided up into 7 energy bins, 200 MeV wide. However, since typically the lower energy cut is around 1.9 GeV and the upper energy cut is fixed at 3.2 GeV, the 7th energy bin is 'troublesome' due to low statistics; indeed, many individual detector fits to data in this bin failed due to lack of data. Therefore, in the following plots we will show results for the first 6 energy bins.

Figs. 3.1 and 3.2 show the fit results for the two data sets, using the 9-parameter fit function. The upper left plots are of $< R >$ vs. energy bin, and a constant is fit to the data points. The values of $< R >$ are very consistent across energy bins for both n-values, and the average of the averages agrees very well with the results obtained using only one energy bin. The lower left plots show the fit asymmetry vs. energy bin. The values for asymmetry are taken from fits to detector 27, the second half of the ring, at around 25 μs after injection. The three plots on the right of Figures 3.1 and 3.2 show the amplitudes of the three CBO effects: N_c, A_c and ϕ_c. Although the amplitudes of the effects are in relative agreement with each other between data sets, the trends of the amplitudes as a function of energy bin differ quite a bit, especially for the ϕ_c term.

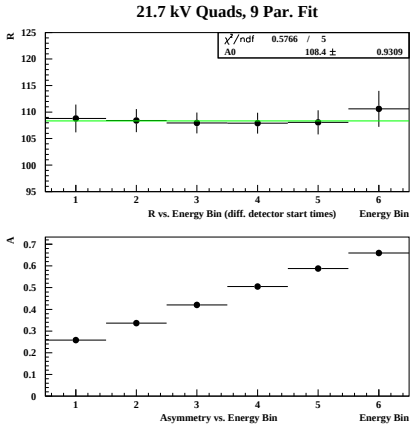

(a) $< R >$ vs. energy bin (top) and fit asymmetry vs. energy bin.

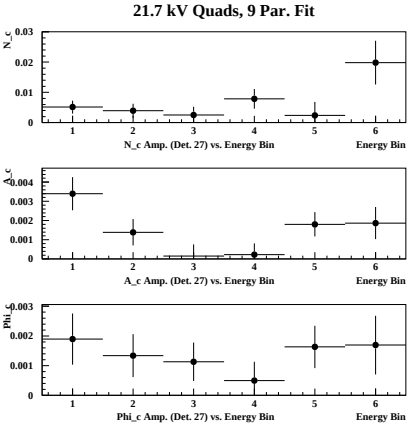

(b) CBO amplitudes vs. energy bin.

Figure 3.1: Various parameters as functions of energy bin obtained from fits to the low n-value data set. Each value of $< R >$ is obtained from a fit to R vs. det. using different start times for each detector. Energy bin 1 corresponds roughly to 1.9 GeV, and each bin is 200 MeV wide.

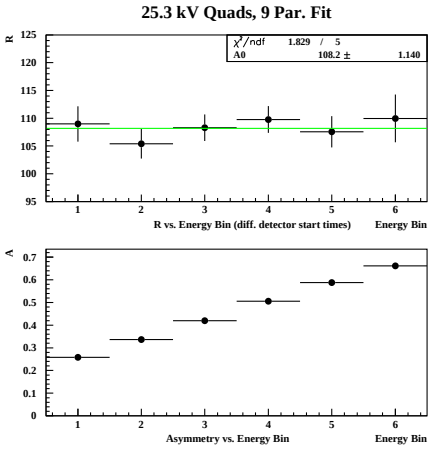

(a) $< R >$ vs. energy bin (top) and fit asymmetry vs. energy bin.

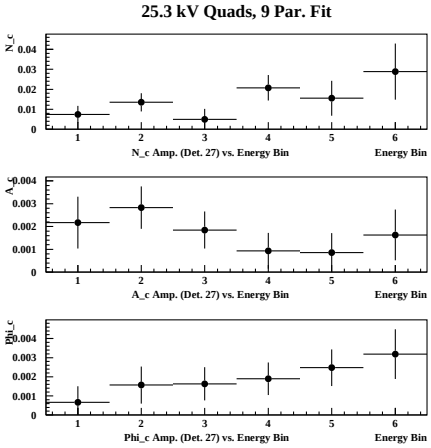

(b) CBO amplitudes vs. energy bin.

Figure 3.2: Various parameters as functions of energy bin obtained from fits to the high n-value data set. Each value of $< R >$ is obtained from a fit to R vs. det. using different start times for each detector. Energy bin 1 corresponds roughly to 1.9 GeV, and each bin is 200 MeV wide.

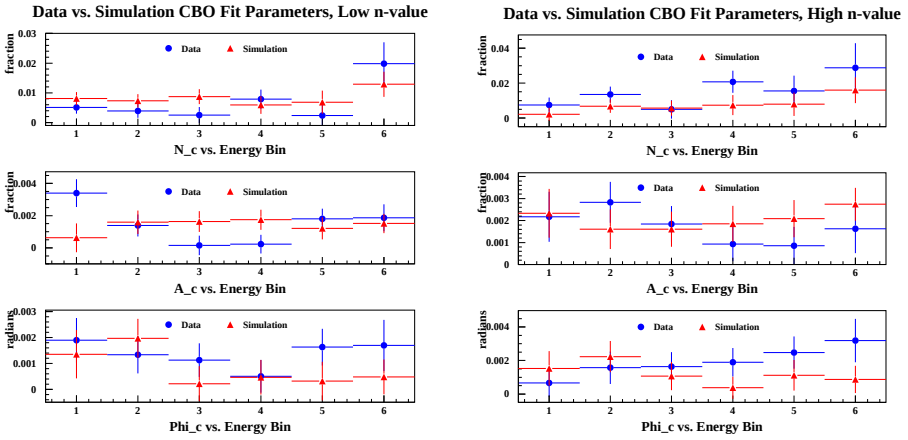

(a) Low n-value data set.

(b) High n-value data set.

Figure 3.3: Comparison between `G2GEANT` simulated data (red triangles) and actual data (blue circles).

To check our energy-binned results, Rob Carey has produced two `G2GEANT`-simulated data sets, each with the corresponding n-values and statistics of the true data sets. The simulation completely describes the ring and detector geometry and material and decay electrons are fully tracked. Energy-binned ratio time spectra of the simulated data were produced and fit to the 9-parameter ratio function. The binwidth of the energy bins of the simulated data is 200 MeV, and the minimum energy is 2 GeV. The results of the fits to both the simulated and true data are shown in Fig. 3.3. There is in general good agreement between the data and simulation. With a few exceptions, all fit results agree within errors.

However, as was first demonstrated by Chris Polly, there is an inconsistency of R vs. E-bin when R when obtained from fits to detector 25 (equivalent to fitting all detectors with the same fit start time) for the high n-value data set. The inconsistency is at a level at which it is very difficult to determine if there is a systematic problem, or if it is due to simply statistical fluctuations. In order to make an energy-binned study that is compatible to those of the other ω_a analyzers, the data were re-combined in energy-binned time spectra in steps of 200 MeV, with the center of the energy bins at 1.5 GeV, 1.7 GeV, etc. for each detector. Polly's findings were confirmed, as shown in Fig. 3.4, which are plots of R vs. E-bin for the low-n and high-n data sets. The top plots show R vs. E-bin fit to a constant in the energy range 1.8-3.4 GeV, the bottom plots show R vs. E-bin fit to a line in the same energy range. We see that the χ^2 of the fit of a constant to R vs. E-bin for the low-n data set has a perfectly acceptable

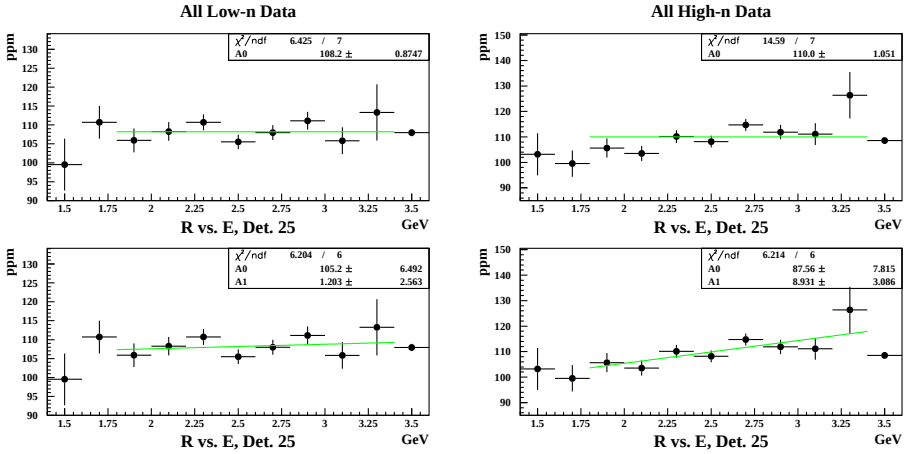

(a) All low-n data.

(b) All high-n data.

Figure 3.4: R vs. Energy bin for the low (left) and high (right) n-value data sets. A constant is fit to the top plots, whereas a straight line is fit to the bottom plots. Results are from a 3-parameter ratio fit at $\sim 33\mu s$.

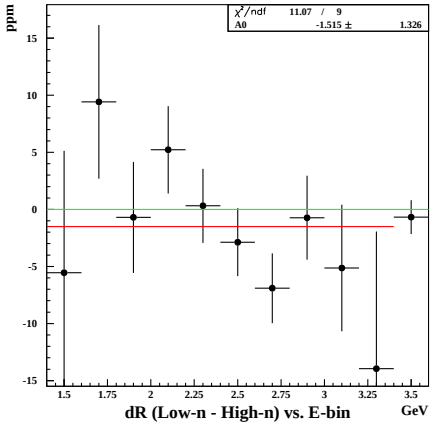

Figure 3.5: Difference of R vs. E-bin between the low-n and high-n data sets using a 9-parameter fit to the sum of all detectors at $\sim 33\mu s$. The bin centered at 3.5 GeV represents the sum of energies from 1.8-3.4 GeV. The green line shows a difference of zero, the red line shows a fit of a constant to the difference in R from 1.4-3.4 GeV.

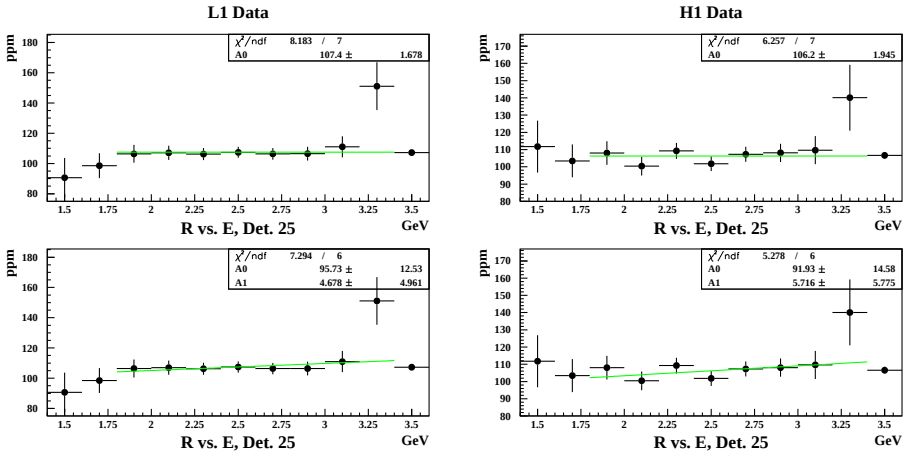

(a) L1 data subset.

(b) H1 data subset.

Figure 3.6: R vs. Energy bin for the first subsets of the low (left) and high (right) n-value data sets. A constant is fit to the top plots, whereas a straight line is fit to the bottom plots. Results are from a 3-parameter ratio fit at $\sim 33\mu s$.

value, whereas the same fit to the high-n data set has a χ^2 of ~ 2.1. Again, a fit $\chi^2/d.o.f.$ is not a "smoking-gun" of any systematic issue. As noted by Polly, a fit of the high-n data set to a straight line gives a much better χ^2. Fig. 3.5 shows a plot of the difference in R between the two data sets as a function of energy bin.

It should also be noted that it was determined that the "inconsistency" of R vs. E-bin is independent of fit function used; a comparison of R vs. E-bin as determined from a 9-parameter ratio fit and R vs. E-bin as determined from a 3-parameter ratio fit found little differences between the two. Therefore, since computationally a 3-parameter fit is much faster than the 9-parameter ratio fit, all R vs. E-bin studies discussed in this report were made using the 3-parameter ratio fit, unless otherwise noted.

To further investigate the discrepancy of R vs. E-bin, the data were split up into subsets according to chronological order. During the 2001 run, data were taken with alternating value of n, so the first subset is of low-n, the second subset is of high-n, the third subset is of low-n, etc. The subsets are henceforth labeled L1, H1, L2, H2, etc., where "L" corresponds to low-n, "H" corresponds to high-n, and the number following the letter corresponds to the subset of that data set. R vs. E-bin for L1, H1, L2 and H2 are shown in Figs. 3.6-3.8. We see that there is no significant discrepancy in fits of R vs. E-bin to a constant for either L1, H1, L2, or H3. However the subsets H2 and L3 definitely show strange behavior of R vs. E-bin, as seen by the fit χ^2's of R vs. E-bin to a

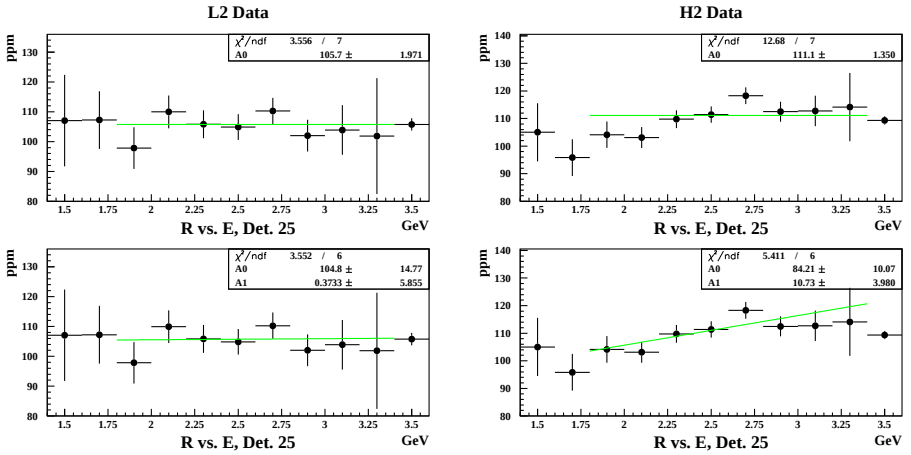

(a) L2 data subset.

(b) H2 data subset.

Figure 3.7: R vs. Energy bin for the second subsets of the low (left) and high (right) n-value data sets. A constant is fit to the top plots, whereas a straight line is fit to the bottom plots. Results are from a 3-parameter ratio fit at $\sim 33\mu s$.

constant.

The data were next fit on a detector-by-detector basis, so that R vs. E-bin was determined for each detector. Each R vs. E-bin plot was then fit to a straight line, and the slope of that line is plotted as a function of detector number in Figs. 3.9-3.10 for the various sets and subsets of data. Constants were then fit to each of these plots, which gives the average slope over the 23 detectors. These plots show an average slope that is *consistent* with zero at the 1.8 σ and 2.9 σ level for the entire high-n data set and the H2 data subset respectively. All other fits show slopes that are consistent with zero at well below the 1 σ level.

In order to determine if there is a fit start-time dependence of the R vs. E-bin, R vs. E-bin was determined for $\sim$ 175 different start times, from $\sim 33 - 250\mu s$. Each of these plots was fit to both a constant and to a straight line. The $\chi^2/d.o.f.$ of the fit to a constant is plotted as a function of fit start time in Fig. 3.11(a), and the fit slope as a function of fit start time is shown in Fig. 3.11(b). Interestingly enough, although the slopes of R vs. E-bin are quite consistent vs. fit start time, only at very early fit start times does the high-n data set show a discrepancy of R vs. E-bin with regard to the fit χ^2 of R vs. E-bin to a constant.

Several ideas as to possible causes of an energy dependent R value have been proposed, but so far, all have been ruled out. We here discuss a few of these studies that were pursued in this analysis: laser contamination, data

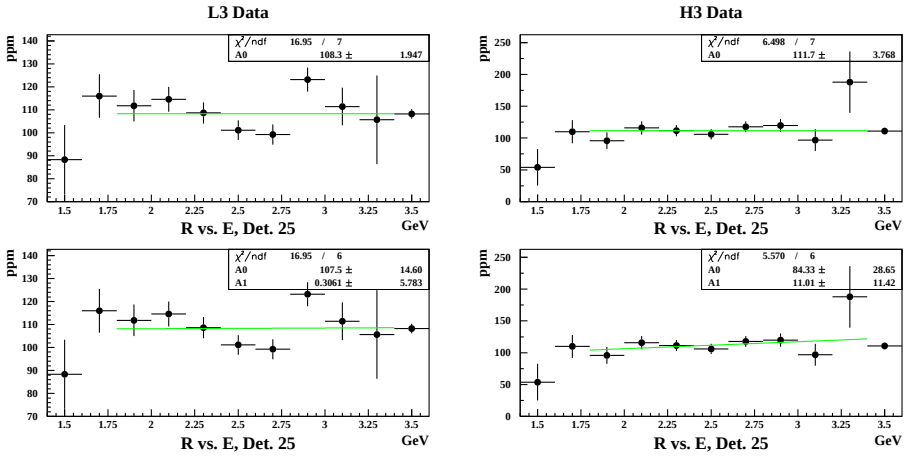

(a) L3 data subset.

(b) H3 data subset.

Figure 3.8: R vs. Energy bin for the third subsets of the low (left) and high (right) n-value data sets. A constant is fit to the top plots, whereas a straight line is fit to the bottom plots. Results are from a 3-parameter ratio fit at $\sim 33\mu s$.

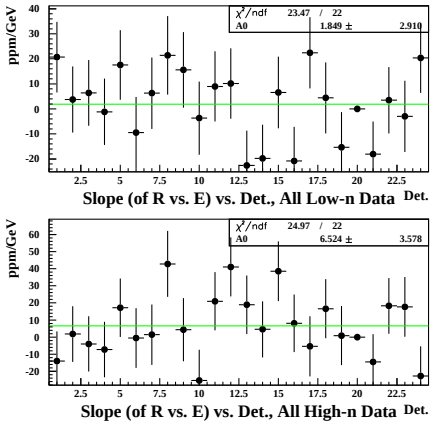

Figure 3.9: Slopes of R vs. E-bin obtained for each detector for the entire low-n data set (top) and the entire high-n data set (bottom). Results are from a 3-parameter ratio fit at $\sim 33\mu s$.

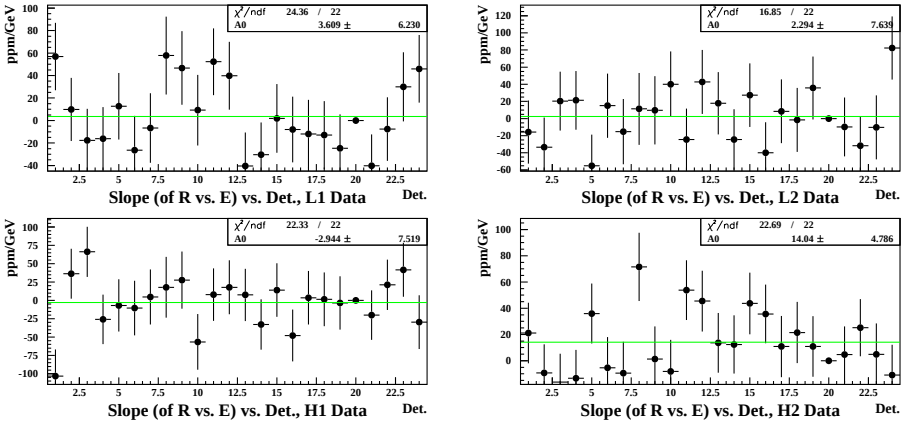

(a) First data subsets, L1 and H1.

(b) Second data subsets, L2 and H2.

Figure 3.10: Slopes of R vs. E-bin obtained for each detector for the first two subsets of the low- and high-n data set. Results are from a 3-parameter ratio fit at $\sim 33\mu s$.

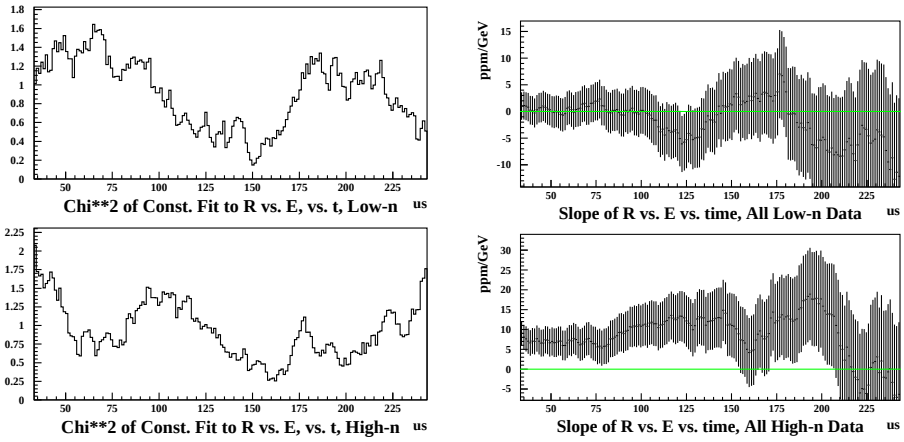

(a) Top: Low-n data. Bottom: High-n data.

(b) Top: Low-n data. Bottom: High-n data.

Figure 3.11: Left: $\chi^2/d.o.f$ of fit of a constant to R vs. E-bin as a function of fit start time. Right: Slopes of R vs. E-bin as a function of fit start time. Fit results are from a 3-parameter ratio fit to the sum of all data (det. 25).

duplication, and electrostatic quadrupole stability.

Early on in the search for a cause of the R vs. E problem it was noted that the H2 data set contains an above average number of laser runs as compared to the other data sets. The data were therefore resummed where not only all laser runs were removed, but also runs immediately following laser runs were removed (in case the laser had inadvertantly been left on). This had absolutely no effect on R vs. E, therefore laser contamination has been ruled out.

Jim Miller recommended that a sanity-check on possible data duplication be made. The concern here is that is that data could somehow have been copied either between detectors or between fills. Such data duplication would tend to produce poor χ^2's of fits to data and could possibly exaggerate a statistical fluctuation. Therefore a study was completed that a) searched for identical files across all runs, b) sorted and searched for duplicate (E, t) pairs in each run for each detector, and c) search for duplicate (E, t) pairs across detectors for each run. No identical files were found. As for duplicate (E, t) pairs, several "duplicates" were found per run, which sets the scale for a level of background. However, as shown in Fig. 3.12, two runs showed several orders of magnitude greater number of duplicate pairs than was typically seen. It was found that in these runs, numbered 11099 and 11268, data at the very end of the run were duplicated; how this happened is not yet understood. However, since these runs do not belong to the H2 data set, data duplication does not seem to be the cause. Furthermore, since data duplication is of a more general concern, since even with the highly-contaminated runs included the level of duplicate data (which also appears to have a normal-looking energy and time spectrum, see, ie: Fig. 3.13) contamination is around 30 ppm, the effect of duplicate data on R is quite negligible.

Electrostatic quadrupole stability was another concern for the H2 data set, since it is known that later in the 2001 run, it was extremely difficult to maintain 25.3 kV on the plates due to the deterioration of the vacuum. In the `G2OFF` ntuple, quadupole information is kept in the `IQUAD` (integer number giving the length, in μs of the quadrupole pulse), `QEARLY` (measure of the quadrupole voltage in ADC counts at early times, during scraping), `QMID` (measure of the quadrupole voltage in ADC counts $\sim 45\mu s$ after injection, and `QLATE` (measure of the quadrupole voltage in ADC counts $\sim 30\mu s$ before the quadrupole voltage drops to 80% of the `QMID` value) variables. Figs. 3.14-3.15 show the average values of the quadrupole voltage as a function of run (error bars are plotted, but too small to see in most cases), as well as the average value of the percent difference between the "mid" and "late" quadrupole voltage readings. The voltages seem quite stable from run to run, more so in the earlier part of the 2001 run than in the latter part. Red points show the voltages for the low-n data set, and the blue points show the voltages for the high-n data set. The quadrupole voltages appear to be fairly stable, and in particular the H2 data set does not appear to show any odd behavior in this regard.

At the moment, the strange behavior of R vs. energy-bin in the H2 and L3 data sets is not understood. Studies are in progress to narrow down other possible causes of the energy-dependence of R.

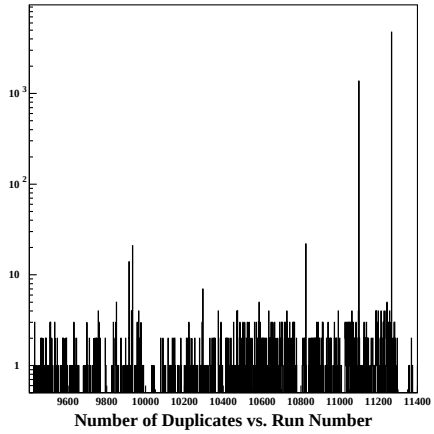

Figure 3.12: Number of duplicate (E, t) pairs found vs. run, in the first 250,000 pulses seen in each detector (some runs saw less than this number of pulses). Note the log scale on the number of duplicates. Two runs in particular show very large numbers of duplicates, runs 11099 and 11268, where it seems that data was overwritten or duplicated at the very end of both of these runs.

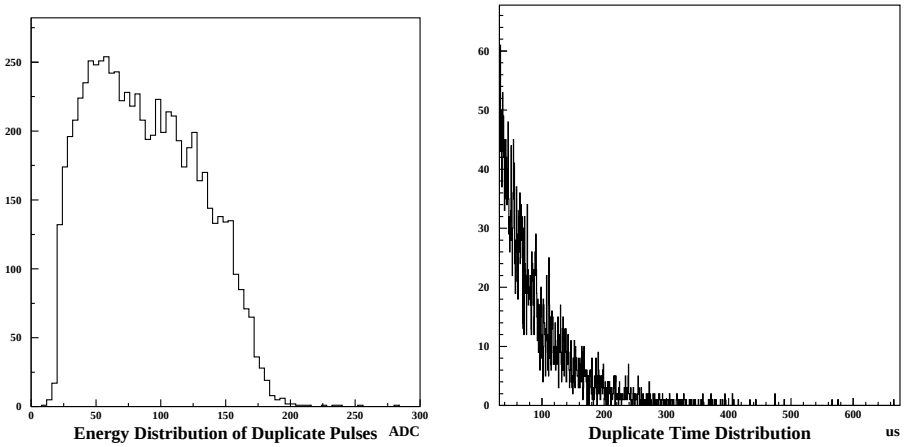

(a) Energy distribution of all duplicates.

(b) Time spectrum of all duplicates.

Figure 3.13: Energy and time spectra of all duplicate (E, t) pairs found.

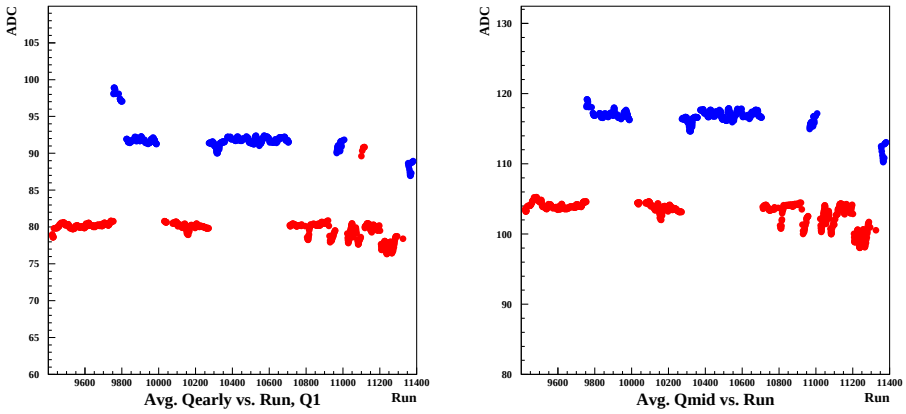

(a) Average QEARLY vs. Run.

(b) Average QMID vs. Run.

Figure 3.14: Average quadrupole voltage vs. run at both early times and "mid" times ($\sim 150\mu s$ after injection). Red points are for the low-n data set, blue points are for the high-n data set.

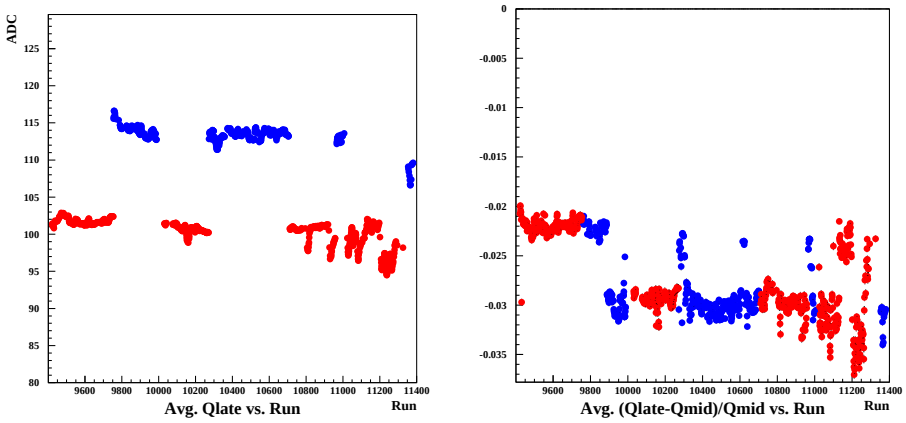

(a) Average QEARLY vs. Run.

(b) Average QMID vs. Run.

Figure 3.15: Average quadrupole voltage vs. run at late times, as well as the relative difference between the "mid" and late time quadrupole voltages. Red points are for the low-n data set, blue points are for the high-n data set.

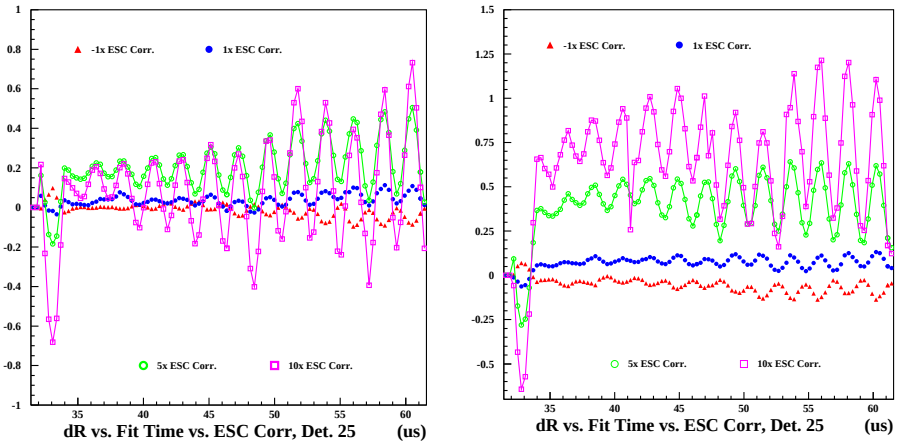

Figure 3.16: Difference of R vs. fit time plots for detector 25 (sum of all detectors) between un-corrected and gain-corrected data. Left: low n-value results. Right: high n-value results.

3.2 Energy Scale Changes

To determine the systematic error on R due to energy-scale corrections, we vary the amount of correction applied to the data by some factor α, fit the data to the 9-parameter ratio function, and determine how R changes as a function of α: $dR/d\alpha$. The error on R is therefore

$$dR_{ESC} = \frac{dR}{d\alpha} \times \delta\alpha \tag{3.1}$$

Fig. 3.16 plots the difference in resulting R-values between non-gain-corrected and gain-corrected data. The blue circles represent R(no correction)-R(1x correction) vs. fit time. The red triangles represent R(no correction)-R(-1x correction) vs. fit time, and the green circles and purple squares represent similar differences between R(no correction) and R(5x correction) and R(10x correction) respectively. One immediately sees a phase-pulling in the differences at twice the g-2 frequency which is expected from the ratio method (see Section A.2). Also, the differences are small for reasonable gain corrections (ie: 1x): a maximum value of 0.08 ppm for the low n-value data and a maximum value 0.15 ppm for the high n-value data. The differences can be a bit larger when applying a 5x or 10x gain correction, however this is a statistical effect. When applying such large corrections to the energies, large changes are made to the number of events; many high energy electrons are thrown out due to the applied upper energy cut, and many lower energy electrons are added to the time spectrum that otherwise would not have passed the applied lower energy cut.

To determine the systematic error on R due to applying the energy-scale change correction, we determine $dR/d\alpha_{ESC}$ for each detector at it's particular fit start time, where α_{ESC} is the scale factor of the applied correction. Therefore

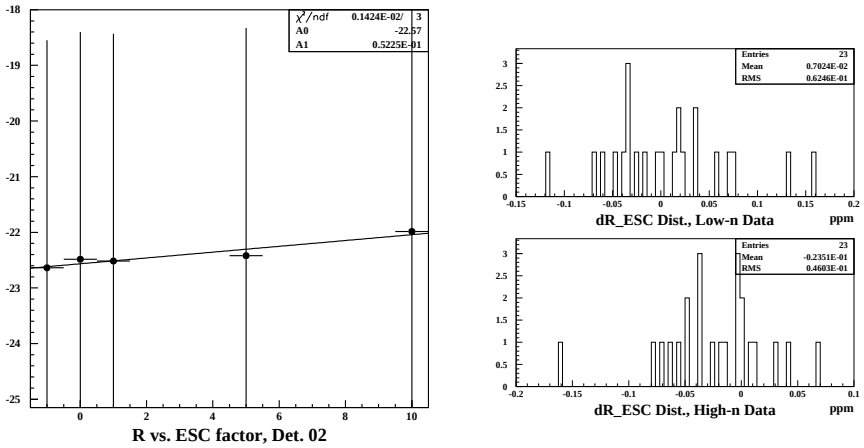

Figure 3.17: Left: R vs. α_{ESC} for detector 2 (low n-value data set). Right: Distributions of dR_{ESC} over detectors, for the low n-value data set (upper right) and the high n-value data set (lower right).

in this study we use values of α_{ESC} = -1, 0, 1, 5 and 10. As an example, the plot on the left of Fig. 3.17 shows R vs. α_{ESC} for detector 2 for the low n-value data set. The plot is fit to a straight line, to obtain the slope $dR/d\alpha_{ESC}$ in units of ppm/α_{ESC}. The uncertainty on the correction itself, $\delta\alpha$ is estimated to be 40%, obtained from a comparison of energy scale change corrections determined by the various ω_a analyzers. The plots on the right of Fig. 3.17 are the distributions of dR_{ESC} over the values determined for the 23 detectors for the two data sets using the above prescription. We find that dR_{ESC} is less than 0.01 ppm for the low n-value data set, and 0.024 ppm for the high n-value data set.

As discussed in Section 2.4, another energy-scale systemic effect exists due to the pulse-fitting algorithm's dependence on island length. Logashenko has calculated the effect of island length on average energy and has estimated the energy-scale correction as a function of time for each detector due to this effect. Fig. 3.2 shows the correction for the worst-effected detector (7) and a typical "quiet" detector (16). Note the g-2 oscillation in the correction itself; such an oscillation is potentially very dangerous. The g-2 oscillation in the correction arises due to there being a higher probability of having two or more pulses on a WFD island at the top of the g-2 cycle than at the bottom. However, the particular shape and magnitude of the correction is difficult to predict, since this depends largely on the shape of the flash background seen by each detector. Those detectors closest to the point of injection obviously see the largest effect, since they see the largest amount of flash. However, for some unknown reason, detector 7 behaves worse than detector 4, the magnitude of the correction being nearly twice as large for 7 yet the flash backgroud is nearly half that seen in detector 4. Luckily the amplitude of the oscillations is fairly small, at the level of 10^{-4}. The difference in R as a function of time for detectors 7, 16 and 25

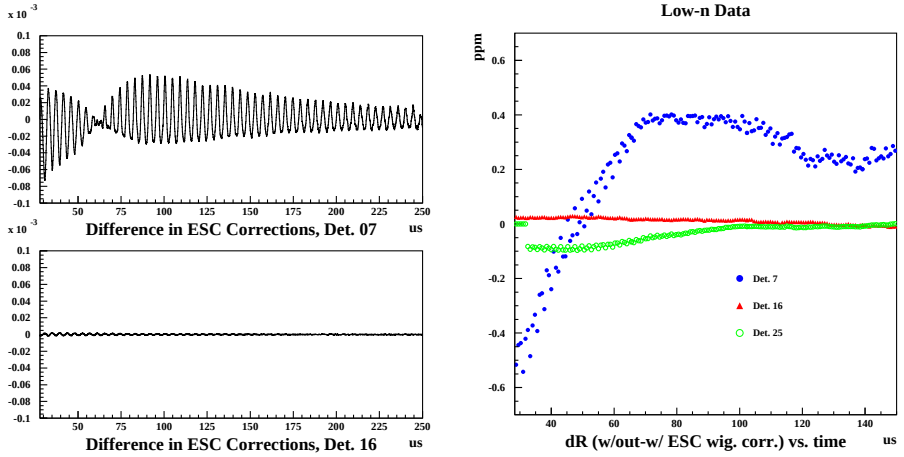

Figure 3.18: Left: ESC correction due to the pulse fitting algorithm's dependence on island length. The island length varies with the g-2 frequency due to a higher probability of having two or more pulses on an island at the top of the g-2 cycle than at the bottom. Detector 7 sees the largest ESC due to this effect, whereas detector 16 (typical of most quiet-side detectors) sees hardly any effect. Right: Difference in R vs. fit start time due to not applying and applying the wiggling ESC correction.

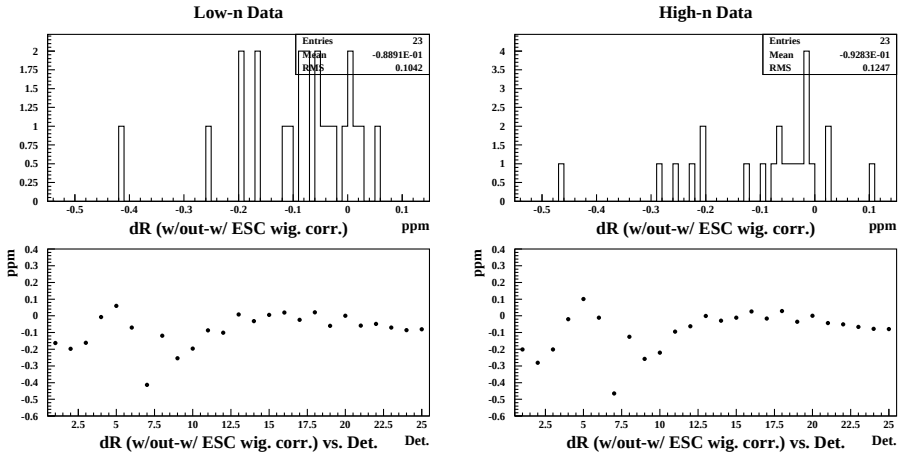

Figure 3.19: Distributions of difference in R when the wiggling ESC correction is applied to the data for the low-n (left) and high-n (right) data sets. Bottom: dR vs. Detector.

(the sum of all detectors) is shown in Fig. 3.2. As expected, detector 7 shows the largest difference in R. The effect on the sum of all detectors is found to be approximately 0.1 ppm near 32 μs after injection.

The two plots in Fig. 3.19 show the differences in R when the correction is applied for each detector (at their individual start times), both the distribution and as a function of detector. The results are very consistent for both data sets: the mean difference in R is $\sim$ 0.09 ppm. We therefore claim 0.1 ppm as the systematic uncertainty due to this effect. Note that we do not yet add this in quadruature to the systematic uncertainty on R due to the applied energy-scale corrections in quadrature, since wish to treat these two effects differently when combined with other systematic errors (ie: pileup subtraction).

3.3 Coherent Betatron Oscillations

The effects of coherent betatron oscillation of the muons in the storage ring on the spin precession frequency ω_a are at this point well understood. If one ignores these effects in the ratio method, or does not properly account for them in the fit function, we find phase pulling in the R value when we look at R vs. fittime. This is especially clear when we look at the difference of R vs. fittime between two halves of the ring, where we sum the data for one half of the ring and fit it and we sum the data from the other half of the ring and fit it. These difference plots have already been shown, however we summarize them in Figs. 3.20 and 3.21. Oscillations of the frequency $f_c - 2f_a$, or $\sim 30kHz$ are clearly seen in the 3- and 5-parameter fits, whereas the 7- and 9-parameter fits drastically reduce the amplitude of the oscillations.

Another interesting difference plot to consider is the difference of R vs. fittime between the various fit functions for a given detector. These plots are found in Figs. 3.22-3.27. Since there are 4 different fit functions used, we the differences shown are between the 3- and 5-parameter fits (R3-R5), the 3- and 7-parameter fits (R3-R7), the 3- and 9-parameter fits (R3-R9), the 5- and 7-parameter fits (R5-R7), and so on. One should note, however, that error bars are *not* drawn in these plots.

The differences between R values found from the 3- and 5-parameter ratio functions and those found using the 7- and 9-parameter functions is stunningly clear, especially for the 'quiet' side of the ring, detector 27, the sum of detectors 13-24. However, the effect is still quite clear even when all detectors are summed (detector 25), and the amplitude of the oscillations is $\sim$ 0.3 ppm for the low n-value data and $\sim$ 0.8 ppm for the high n-value data.

With the full 9-parameter physics function, the systematic error on R due to CBO comes from uncertainties in the functional form of the CBO effects, which is reflected in uncertainties (widths) of the cbo frequency and lifetime. To determine the systematic error on R due to CBO, the individual detector data were fit to the full physics function with varied fixed CBO lifetimes (with the CBO frequency fixed at the nominal value) and then with varied frequencies (with the CBO lifetime fixed at the nominal value), at the final fit start time.

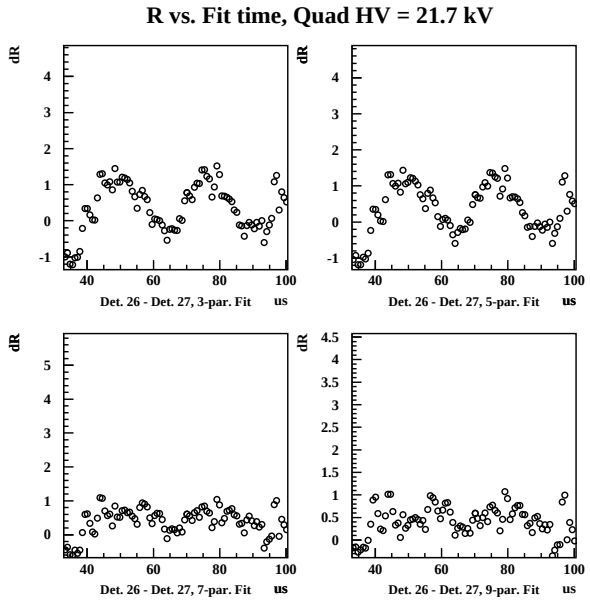

Figure 3.20: Difference between first-half and second-half of the ring of R vs. fit time for various fit functions applied to the Quad HV=21.7 data.

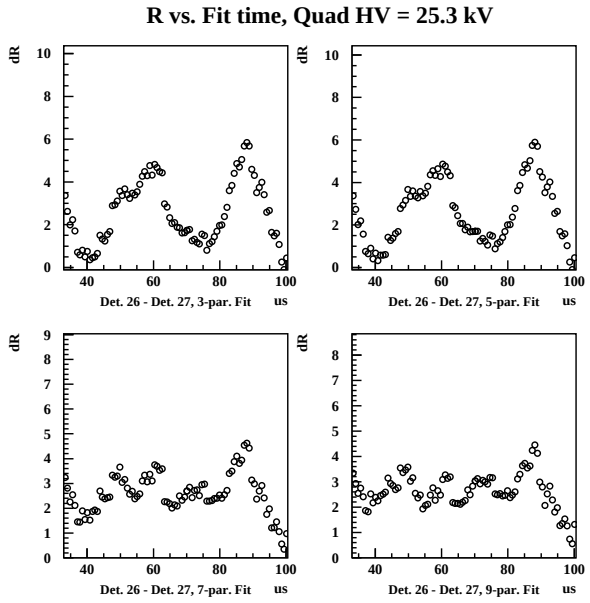

Figure 3.21: Difference between first-half and second-half of the ring of R vs. fit time for various fit functions applied to the Quad HV=25.3 data.

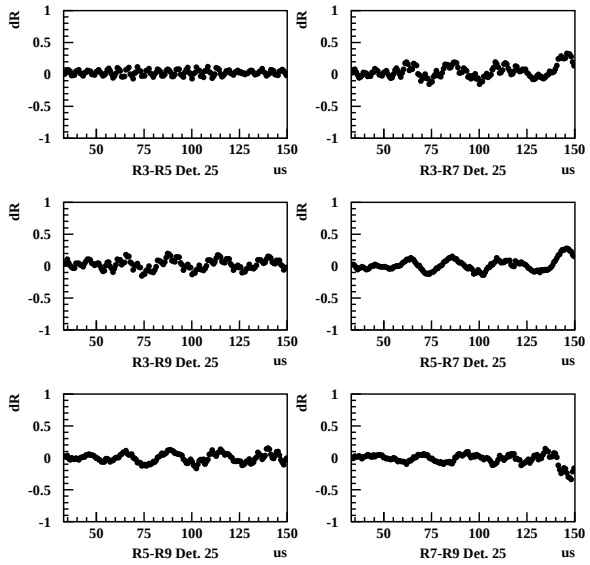

Figure 3.22: Difference between various fit functions of R vs. fit time plots of detector 25 applied to the Quad HV=21.7 data. Rn, where $n = 3, 5, 7, 9$ refers to the 3-, 5-, 7-, and 9-parameter ratio fit functions.

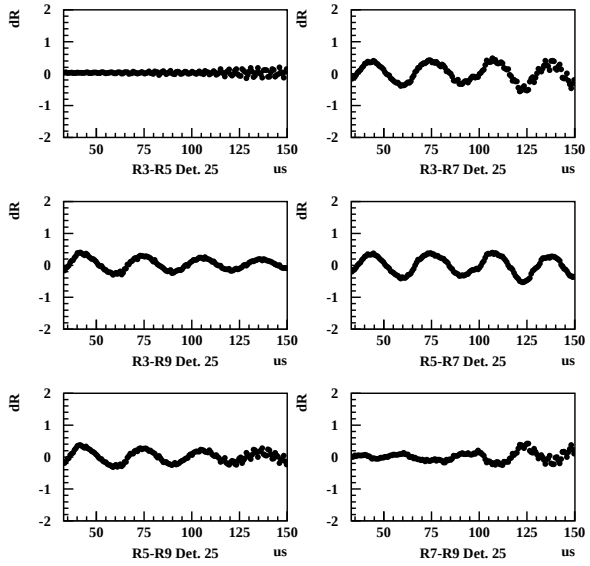

Figure 3.23: Difference between various fit functions of R vs. fit time plots of detector 25 applied to the Quad HV=25.3 data. Rn, where $n = 3, 5, 7, 9$ refers to the 3-, 5-, 7-, and 9-parameter ratio fit functions.

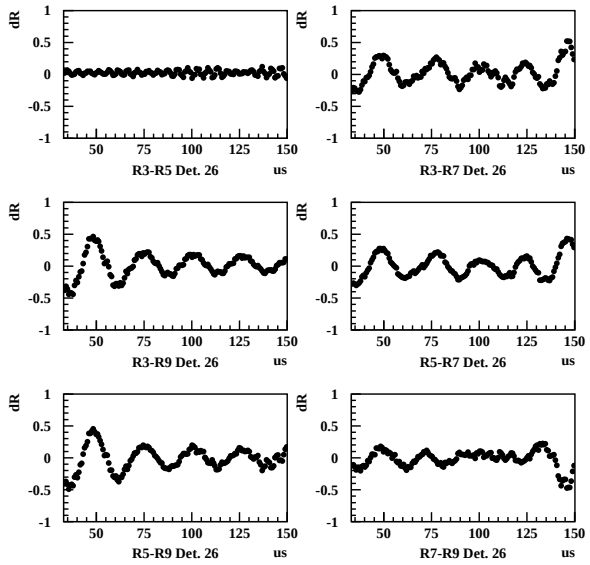

Figure 3.24: Difference between various fit functions of R vs. fit time plots of detector 26 applied to the Quad HV=21.7 data. Rn, where $n = 3, 5, 7, 9$ refers to the 3-, 5-, 7-, and 9-parameter ratio fit functions.

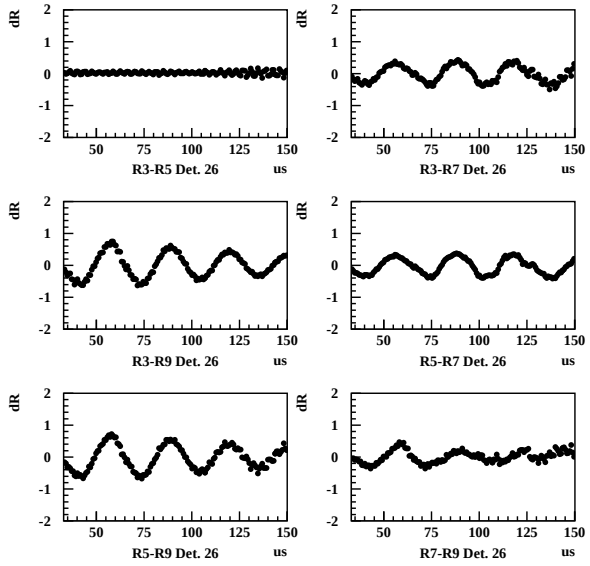

Figure 3.25: Difference between various fit functions of R vs. fit time plots of detector 26 applied to the Quad HV=25.3 data. Rn, where $n = 3, 5, 7, 9$ refers to the 3-, 5-, 7-, and 9-parameter ratio fit functions.

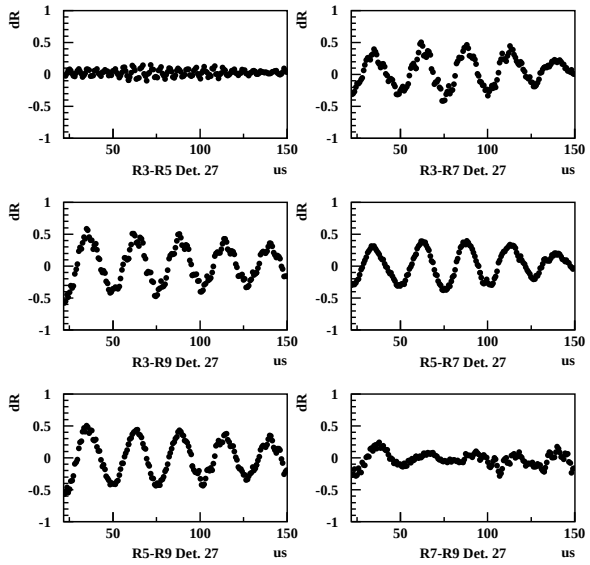

Figure 3.26: Difference between various fit functions of R vs. fit time plots of detector 27 applied to the Quad HV=21.7 data. Rn, where $n = 3, 5, 7, 9$ refers to the 3-, 5-, 7-, and 9-parameter ratio fit functions.

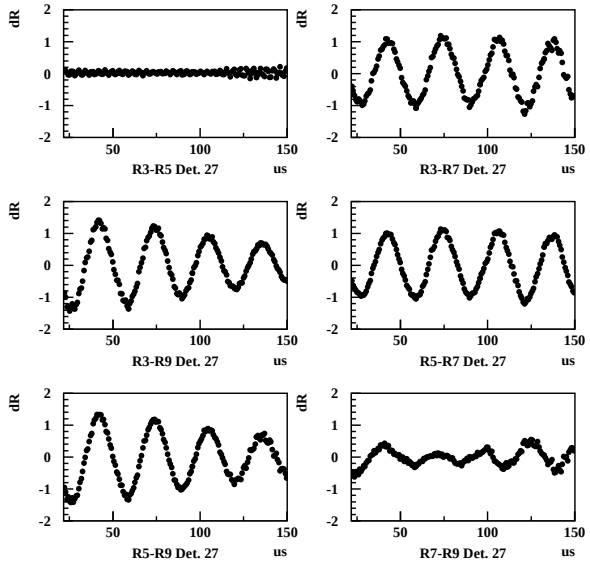

Figure 3.27: Difference between various fit functions of R vs. fit time plots of detector 27 applied to the Quad HV=25.3 data. Rn, where $n = 3, 5, 7, 9$ refers to the 3-, 5-, 7-, and 9-parameter ratio fit functions.

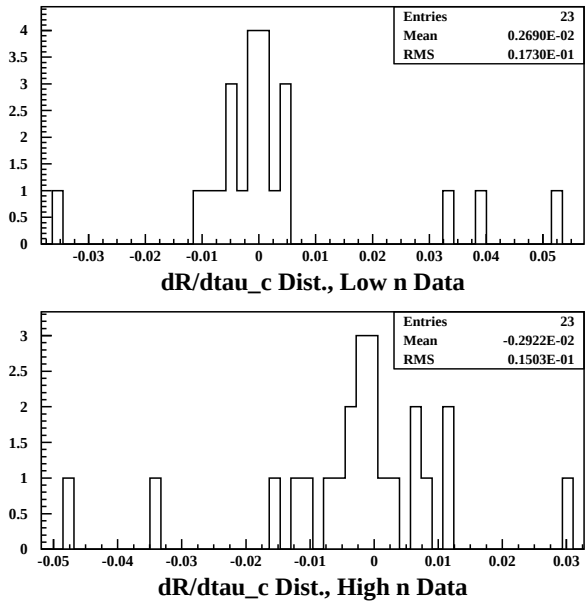

Figure 3.28: Distribution of $dR/d\tau_c$ determined for each of the 23 detectors at their corresponding fit start times. Top: results for the low n-value data set. Bottom: results for the high n-value data set.

The CBO envelope lifetime was varied from 82.1 to 102.1 μs and 120.1 to 140.1 μs for the low and high n-value data respectively in 5 μs steps, where the nominal lifetimes are 92.1 and 130.1 μs respectively. The CBO frequency was varied between 417.5-420.7 kHz and 489-492.2 kHz for the low and high n-value data respectively in 0.8 kHz steps. $dR/d\tau_c$ and dR/df_c where then determined for each detector by fitting a straight line to the R vs. τ_c and R vs. f_c plots. Figs. 3.28 and 3.29 show the distribution of these slopes for the 23 detectors. Taking the mean values of the distributions, and an uncertainty of 5 μs in the CBO lifetime and 0.6 kHz in the CBO frequency, we find for the low n-value data set a value of $dR_{\tau_c} = 0.01$ ppm and $dR_{f_c} = 0.03$ ppm; For the high n-value data set the situation is a bit worse, and we find $dR_{\tau_c} = 0.02$ ppm and $dR_{f_c} = 0.07$ ppm.

In addition to the intrinsic uncertainty of the CBO frequency, we must also consider the effect of having a time dependent CBO frequency. The time dependence arises due to scraping; the scraping voltage is turned off (that is, increases to the nominal voltages) with an RC time constant of 5 μs at 7 μs after injection. Therefore, at 23 μs, when data from most of the detectors in the latter half of the ring are fit, the quadrupole voltages are still changing slightly. During scraping, the n-value is [6]

$$n_1 = \frac{V_1 + V_0}{2V_0} n_0 \tag{3.2}$$

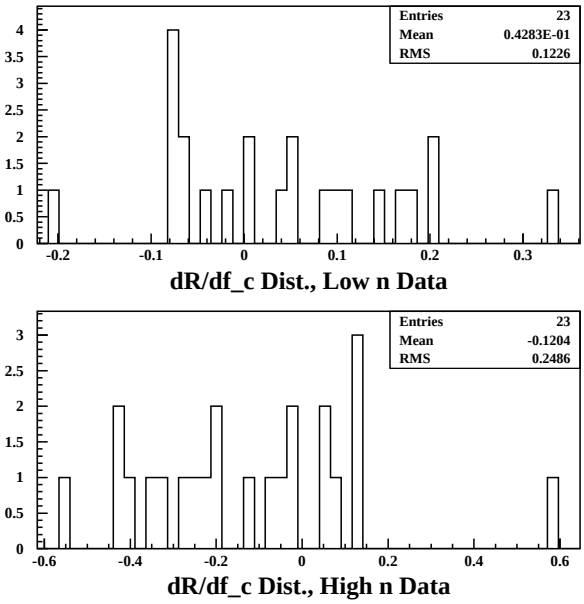

Figure 3.29: Distribution of dR/df_c determined for each of the 23 detectors at their corresponding fit start times. Top: results for the low n-value data set. Bottom: results for the high n-value data set.

where the subscript "1" refers to the value during scraping and the subscript "0" refers to the nominal value (ie: after scraping). The quadrupole voltages during scraping are set to 70% their nominal value, so $n_1 = 0.85 n_0$. Therefore, we have

$$n(t) = n_0(1 - 0.15e^{-(t-7)/5}) \tag{3.3}$$

Since

$$f_{cbo} = f_c(1 - \sqrt{1-n}) \tag{3.4}$$

where f_c is the cyclotron frequency, then plugging in the above time-dependent n-value one can easily show that

$$f_{cbo}(t) = f_{cbo_0} - \frac{0.15 f_c n_0}{2\sqrt{1-n_0}} exp(-(t-7)/5) \tag{3.5}$$

At $\sim 23\mu s$ after injection, the CBO frequency is nearly 0.5% lower than its nominal value. However, putting this time-dependent frequency into the 9-parameter ratio fits did not improve the χ^2 of the fits to the data at early times, and the distribution of differences in R from fits with and without the time-dependent CBO frequency has a mean value of 0.02 ppm for both the low- and high-n data sets. We therefore claim 0.02 ppm as the systematic uncertainty due to the time-dependence of the CBO frequency.

Another issue to consider is whether or not all CBO effects have the same functional form. To estimate this effect, fits to the data were made where we stepped through different lifetimes of the $N_c(t)$ term but held the lifetime of the $A_c(t)$ and $\phi_c(t)$ terms constant; a similar study was made in the reverse order, where the lifetime of the $N_c(t)$ term was held constant and the lifetime of the other two terms was varied. For the low-n data set, in the first case, the average value (over fits to the 23 individual detectors) of $dR/d\tau_N$ was found to be 2.2×10^{-4} ppm/μs. In the second case, the average value of $dR/d\tau_{A,\phi}$ was found to be -4.2×10^{-5} ppm/μs. For the high-n data set, $dR/d\tau_N = 7.6 \times 10^{-5}$ ppm/μs and $dR/d\tau_{A,\phi} = -1.6 \times 10^{-3}$ ppm/μ. A quantitative evaluation of the spread in lifetimes that would be representative of a very different functional form and/or lifetime of the CBO is at this time very difficult to make. However, we feel that a spread of 50 μs (roughly half the determined lifeitme) is reasonable; remember also that the distributions of CBO lifetimes determined from the studies in Section 2.2 is approximately 50 μs. Therefore, we find the uncertainty in R due to CBO envelope is 0.01 ppm for the low-n data set and 0.08 ppm for the high-n data.

Finally, Morse and Semertzidis have raised the possibility of another effect due to the functional form of the $\phi_c(t)$ term having two contributions, one from the radial mean and the other from the radial width, each with a different lifetime and phase. This effect was studied via simulation where the absolute worst-case scenario of the mean and width contributions having completely opposite phases is assumed (we know from tracking that the width and mean are slightly out of phase, but not opposite) and the lifetime of the contribution from the radial width is half that of the radial mean. That is,

$\phi_c(t) = \phi_{c_0}(A_1 \exp(-t/\tau_c)\cos(\omega_c t + \phi_c) - (1 - A_1)\exp(-2t/\tau_c)\cos(\omega_c t + \phi_c))$. Twenty-four time spectra were produced with N_c, A_c and ϕ_c terms included with differents phases that vary linearly (from 0 to 2π) around the ring, and equal amplitudes for each spectra except three (ie: the kicker detectors), where the amplitudes are 50% larger. The relative amount of mixing between the two terms (that is, the radial width and the real mean contributions) was also varied such that $A_1 = 15$-75% in 15% steps. On average, the R value obtained from the naive 9-parameter fit differed by 0.04 ppm from the input value, with a spread of 0.04 ppm. We therefore claim 0.04 ppm as our estimate of the systematic uncertainty due to the CBO phase term having out-of-phase contributions from the radial mean and radial width.

Assuming, quite conservatively, that the CBO frequency and lifetime are 100% correlated, we add those errors together linearly. We then add the uncertainty in R due to CBO envelope in quadrature to get a total systematic error due to CBO of 0.06 and 0.13 ppm for the low and high n-value data sets respectively.

3.4 Pileup

There are in general four main issues with pileup subtraction: (a) pileup construction efficiency, (b) pileup construction phase, (c) choice of shadow pulse window time offset used to construct the pileup, and (d) the effect of low energy pileup. Issues (a)-(c) are very highly correlated and so care must be taken when studying these issues.

Perhaps the easiest issue to deal with regarding pileup subtraction is that of the pileup construction efficiency. We have already estimated the pileup construction efficiency for each detector (on average it is $> 95\%$). To determine the effect that oversubtracting or undersubtracting pileup has on fitting for R, we vary the fraction of pileup subtracted from the data, fit the data and determine $dR/d\alpha_{PUS}$, where α_{PUS} is the fraction of pileup subtracted from the data, by fitting R vs. α_{PUS} for each detector at its specific start time. In this analysis, we allow α_{PUS} to range from 0.9-1.1 in 0.025 steps. Fig. 3.30 shows the distributions of dR_{PU_e}, the systematic error on R due to pileup construction efficiencies, over the 23 detectors, for each data set. The values of dR_{PU_e} were taken from the product of $dR/d\alpha_{PUS}$ and the inefficiency ($\delta\alpha$) of pileup construction determined for each detector. Taking the means of these distributions as the average systematic error, we find that $dR_{PU_e} = 0.034$ ppm for the low n-value data set, and 0.009 ppm for the high n-value data set.

As has been discussed[7], there could be a difference between constructed and true pileup phases. This is potentially quite dangerous, as Fig. 3.31 shows. Here, time spectra were generated assuming the 5-parameter function and a pileup term of the function

$$N_{PU}(t) = N_{0_{PU}} e^{-t/\tau_{PU}} \left(\cos(\omega_a t + \phi_{PU} + N_{1_{PU}} \cos(2\omega_a t + \phi_{PU_2}) \frac{N_{2_{PU}}}{N_{0_{PU}}} \right) \tag{3.6}$$

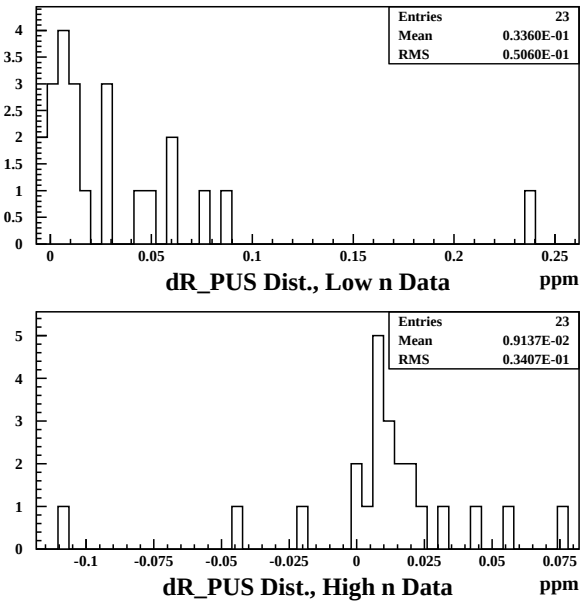

Figure 3.30: Distributions of dR_{PU_e}, the systematic error on R due to pileup construction efficiency, for both data sets.

The generated time spectra assumes $N_0/N_{0_{PU}} = 0.42\%$ at $t = 0$, and the rest of the parameters were obtained from fits to the pileup time spectrum itself. After the original time spectrum is built, pileup spectra with *different phases than the phase used* to generate the pileup background are subtracted from the time spectrum. Differences between 'true' and 'constructed' phases were varied from -40 to 40 mrad, in 20 mrad steps. The plots shown in Fig. 3.31 show differences in fit values of R as a function of fit time between spectra that have the 'true' pileup subtracted off and time spectra that have phase-shifted pileup subracted off. An error in the phase of pileup construction of 20 mrad results in a ~ 0.3 ppm error in R.

An error of 20 mrad, however, is unlikely. However errors in either the L ogashenko coefficients or the energy-dependent deadtime used to construct the pileup pulses could lead to shifts in the constructed pileup phase. This is because some pulses will be added or lost 'near' the edges one's (software) energy thresholds due to the errors in the Logashenko coefficients; the phase is energy-dependent, so this could cause the constructed pileup phase to differ from the true pileup phase.

To estimate the size of this effect, the energy-binned pileup time spectra were fit to Eq. 3.6; the fit values of the pileup phase vs. energy bin are shown in Fig. 3.32. The energy bins are 200 MeV wide, and results from energy bins 1.7-3.3 GeV are shown (note, the energies are the central value of the bin). In

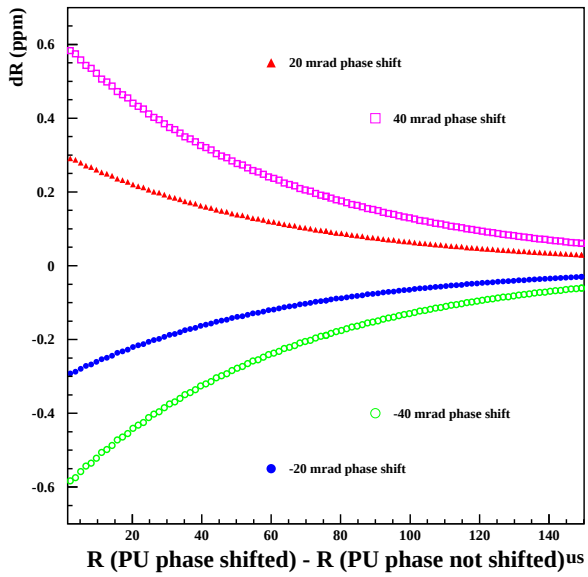

Figure 3.31: dR vs. fit time due to constructing pileup with phases that are shifted by -40, -20, 20, and 40 mrad with respect to the true pileup. These simulation results assume a 0.42% pileup contamination at t=0, and the other parameters used in the functional form of the pileup were obtained from fits to data.

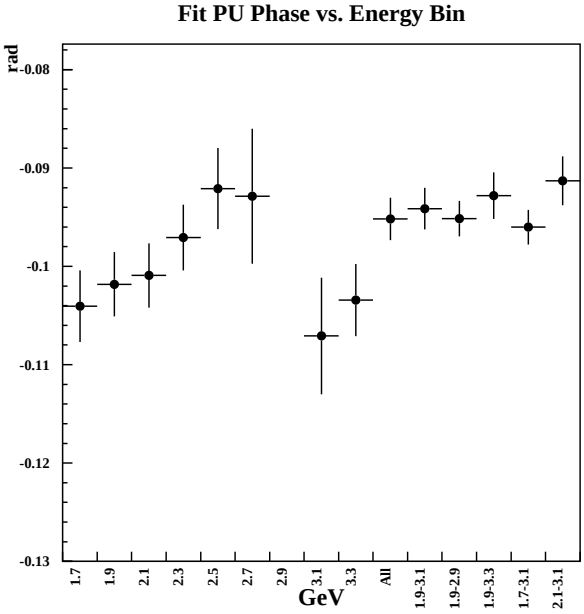

Figure 3.32: Pileup phase vs. energy bin as determined by fitting the time spectra to Eq. 3.6.

addition, fits to larger energy bins were made: 'All' represents the sum over all energy bins, and the numbered bins represent the sum over those bins (ie: 1.9-3.1 is the sum of the data from bins 1.9 to 3.1). Of the last five, the 1.9-3.1 bin is very similar to the energy-cuts used in constructing the time spectra for this analysis, and so the last four bins, 1.9-2.9, 1.9-3.3, 1.7-3.1 and 2.1-3.1 are as if 100% of the bins on the edges of the energy-cuts were added in or subtracted off from the data. We find that the largest change ($\sim$ 2.8 mrad) in pileup phase seen is due to throwing out the lowest energy bin. This is not unexpected, since the pileup phase changes more rapidly in this energy region than in the higher energy region. Since this 2.8 mrad change is obtained by assuming that the entire 200 MeV-wide energy bin would have to be lost during pileup construction, an estimate for the uncertainty in the PU phase of 2.8 mrad is therefore extremely conservative. Assuming a 2.8 mrad uncertainty in the PU phase, we find from Fig. 3.31, that this results in a 0.042 ppm systematic error on R. We therefore set the error due to constructed pileup phase on R to be 0.042 ppm for both data sets.

The effect of low energy pileup on R has been studied by both Ivan Logashenko [8] and Gerco Onderwater. Both found the same overall phase difference produced by the low energy pileup, however Logashenko's estimate of 0.06 ppm was obtained assuming that a phase difference in the pileup of 1 mrad is equivalent to a 3.5 ppm error in R. Onderwater, on the otherhand, did an

actual simulation and found the sensitivity to be much smaller, by a factor of 3. Since both studies found the same phase difference, Onderwater's estimate of 0.02 ppm supersedes Logashenko's estimate of 0.06 ppm.

Adding all errors in quadrature gives $dR_{PUS} = 0.06$ ppm for the low n-value data set and 0.05 ppm for the high n-value data set.

3.5 Muon Losses

One of the great advantages of the ratio method is that the spectrum $r(t)$ is largely unaffected by slow terms, such as muon losses, since these effects largely cancel out. To see this, we have simulated time spectra according to Eq. A.1 but with muon losses included. The muon loss function form (dN_μ/dt) here is an exponential with a lifetime of 25 μs and an amplitude of 1% at t=0. Figures 3.33 and 3.34 show the effects of muon losses when not taken into account when fitting the time spectra to the usual 5 parameter function vs. when fitting via the ratio method. Phase pulling in R vs. fit start time is quite obvious when fitting the 5 parameter function, however the results from the ratio method seem unperturbed by losses.

To obtain a systematic error on R due to muon losses in the ratio fit, the 3FC time spectra obtained from the 21.7 kV data set was fit to an exponential from 30-70 μs, another exponential from 70-100 μs, and a Gaussian from 100-300 μs giving an approximation of the muon loss function. The muon lifetime was also divided out of this function. The figures in 3.35 show the muon loss rate (left) and integrated muon losses (right). The integrated muon losses are normalized such that at very late times, the function goes to one. Therefore, a scale factor multiplying the integrated muon losses corresponds to the total (percentage of) muons lost during data taking.

Having a functional form, we next simulate the electron time spectrum *with no statistical fluctuations* according to the 5-parameter functional form, but include muon losses of varying amounts. Therefore, the function used to create the time spectrum is

$$N(t) = N_0 e^{-t/\tau}(1. + A\cos(\omega_a t + \phi))exp(-A_L F_L(t)) \tag{3.7}$$

where

$$F_L(t) = \int_{t_0}^{t} f_L(t')dt' \tag{3.8}$$

and A_L =0.0, 0.25%,0.5%, 0.75% and 1.0%. Fitting the resulting time spectra to the ratio method and comparing the results to the fit results of the spectrum with no muon losses, we find that the effect on R is extremely small. Fig. 3.36 shows the difference between fit results of spectra with and without muon losses. We see that if we lose a total of 0.6% of our injected muons after scraping, a number which is similar to loss rates determined from multiparameter fits of the actual data, the effect on R is much less than 0.01 ppm at the earliest fit times.

If muon losses were to only affect the number of decay electrons detected, then this would be the end of the story. However, if for some reason the missing

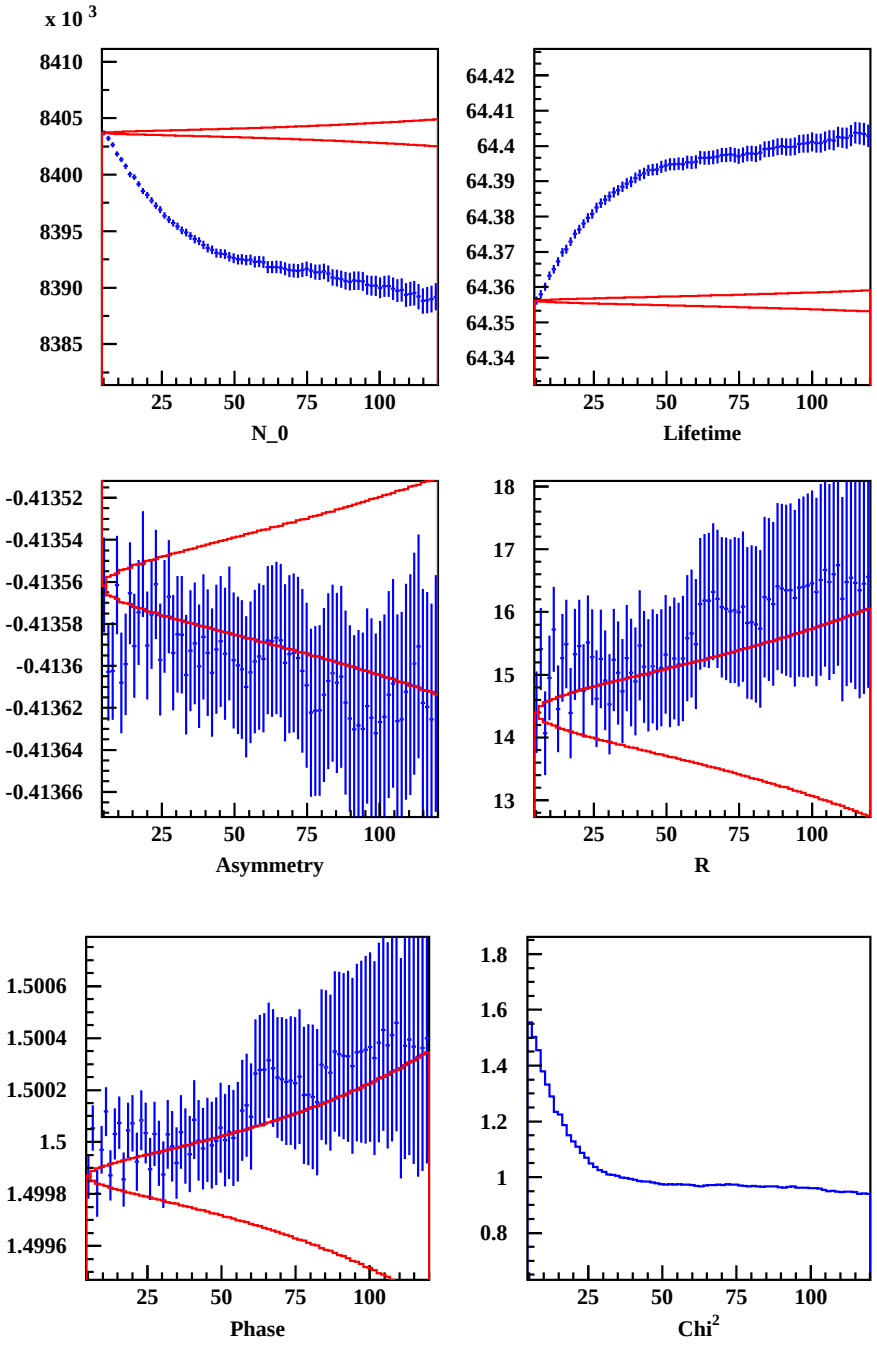

Figure 3.33: Fit results to simulated data. The simulated spectrum is derived from a random distribution according to Eq. A.1, but with muon losses included, and fit to a 5 parameter function. The fitted values of the parameters of the function are plotted vs. starttime of the fit. The red lines are the correlated error bands.

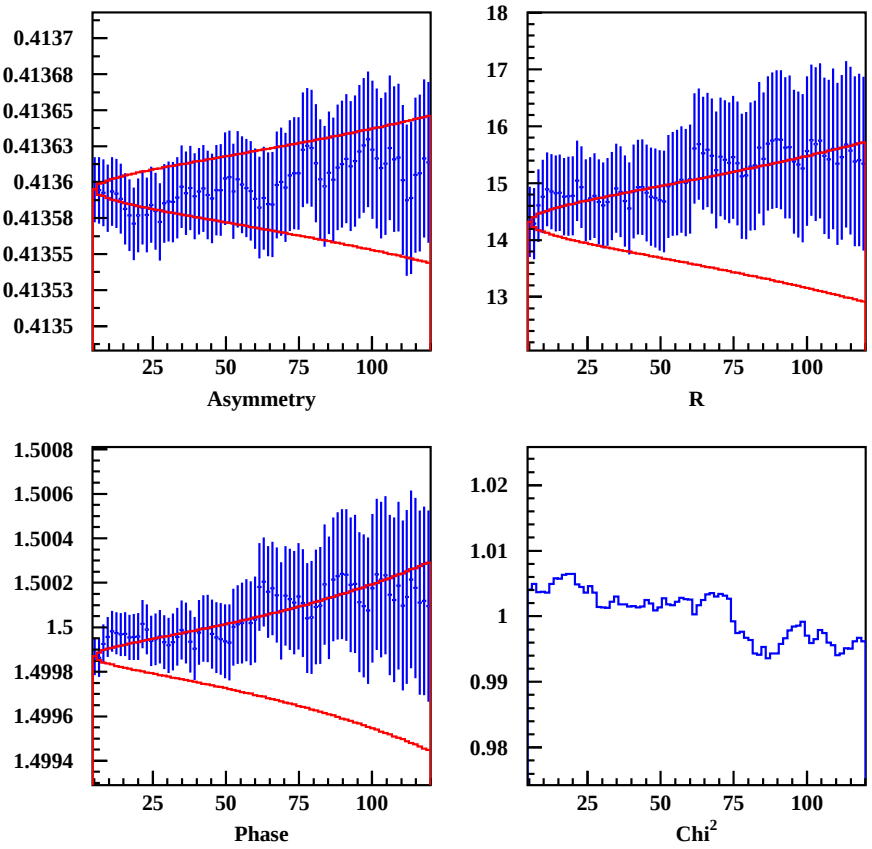

Figure 3.34: Fit results to simulated data. The simulated spectrum is derived from a random distribution according to Eq. A.1, but with muon losses included, rearranged according to Eq. A.7 and fit to the 3 parameter function A.20. The fitted values of the parameters of the function are plotted vs. starttime of the fit. The red lines are the correlated error bands.

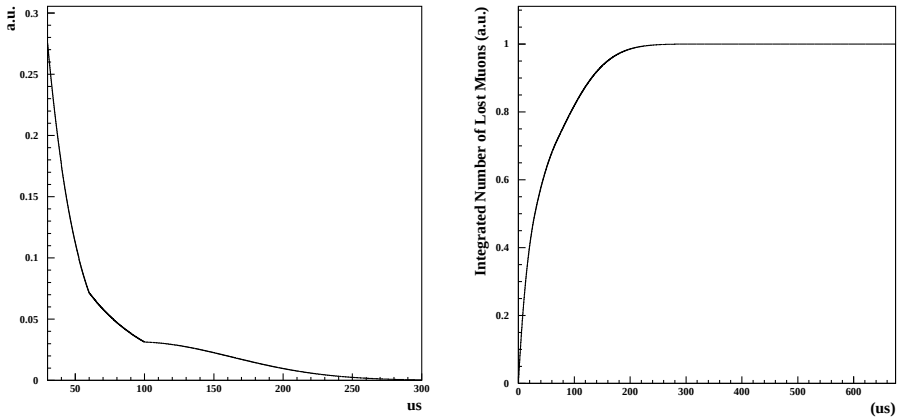

Figure 3.35: Left: Empirical fit to the 3FC time spectrum of the 21.7 kV data set, with the muon lifetime divided out. Right: Integrated muon losses ($F_L(t)$).

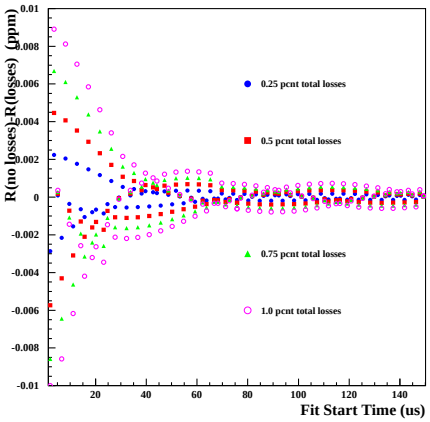

Figure 3.36: Effect of muon losses on R vs. fit start time with the ratio method. Plotted here is fit R(no losses) - fit R(losses). Note the scale of the effect: $< 10^{-4}$ ppm.

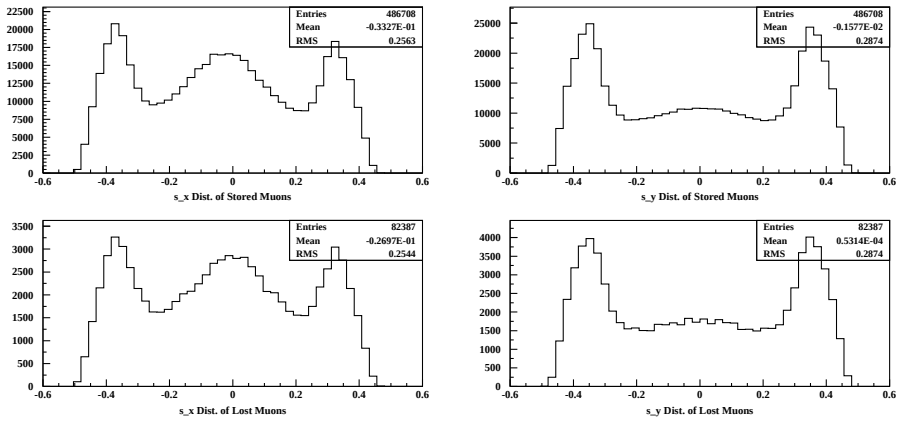

Figure 3.37: Left: radial (x) spin component distribution of injected muons, those that are stored (top) vs. those that are lost (bottom). Right: same as on left, but vertical (y) spin component distributions.

decay electrons (from lost muons) were to have a different average g-2 phase or asymmetry, then this must also be taken into account. Decay electron time spectra taking into account lost muons were generated as described above, however different asymmetries and g-2 phases are assumed for the lost decay electrons. The two plots in Fig. 3.39 show the size of the effect on ω_a for each of these effects. The effect of a slightly changing asymmetry (right plot) has very little effect on R. This is no surprise, as we know that A is not strongly correlated to R in the fits. Indeed, here most of the error on R is due to the effect on the *number* of decay positrons, since the amplitude of the phase pulling changes very slightly as the asymmetry changes. However, we see, as expected, that a changing g-2 phase does have a much larger effect on R (left plot).

There are two ways in which the missing decay electrons could have a different g-2 phase or asymmetry: beamline beam dynamics and storage ring beam dynamics.

Muons born before the beamline dipole magnet D5 have a different g-2 phase than those muons born after D5 (in the straight section of the beamline), since the spins of those born before rotate due to the magnet in D5. The effect on R has been estimated by Bill Morse, and he has set a conservative upper limit to be 0.13 ppm. Another way to check this result is to use tracking. Figs. 3.37 and 3.38 show the initial spin component distributions of those muons that are stored (top plots) vs. those that are lost (bottom plots) in `g2track`. Only muons that are lost after 4 turns around the storage ring are considered, so although muons lost during scraping are used in this study, there is a requirement that the muons at least survive injection and the kick. In this way we are able to obtain reasonable statistics. Stored muons are those that have not been lost after $\simeq 75\mu s$ after injection (muons do not decay in g2track).

The initial spins are obtained from the `BTRAF` program, which simulates the

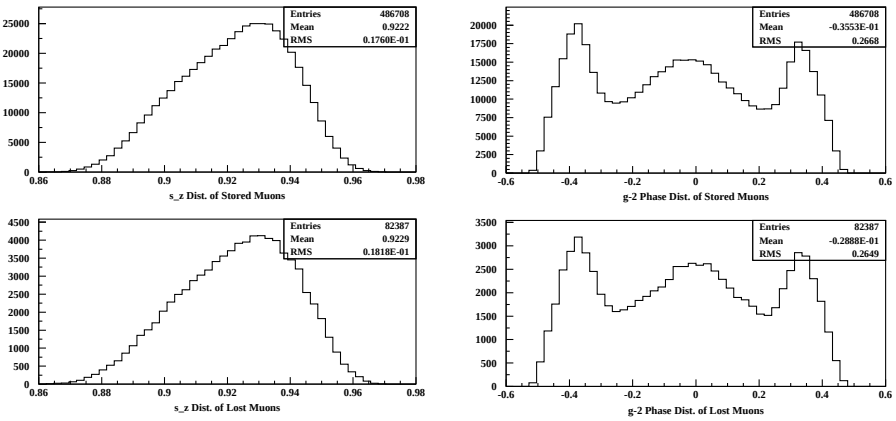

Figure 3.38: Left: longitudinal (z) spin component distribution of injected muons, those that are stored (top) vs. those that are lost (bottom). Right: initial g-2 phase distributions of stored (top) and lost (bottom) muons.

g-2 beamline and tracks spin. The quantity

$$\phi_{xz} = tan^{-1}\left(\frac{s_x}{s_z}\right) \tag{3.9}$$

is therefore the inital g-2 phase of each muon. The distribution of initial g-2 phases is shown in the right plots of Fig. 3.38. Using the $RMS/\sqrt{N}$ as the statistical error, we find that the average g-2 phase of the stored muons is -35.5 $\pm$ 0.4 mrad and that of the lost muons is -28.8 $\pm$ 0.9 mrad. Therefore, there is a difference of -6.7 $\pm$ 1 mrad. Looking at Fig. 3.39 and interpolating between the -4 and -8 mrad plots, we see that this will give an approximate error of 0.1 ppm for a total muon loss of 0.6%. However, Xiaobo Huang finds that the total muon loss is approximately 0.5% for the low-n data set and 0.03-0.04% for the high-n data set, so we can scale the error down to 0.08 and 0.06 ppm respectively.

The beam dynamics of the storage ring could also cause the missing decay electrons to have a different phase and asymmetry, since the lost muons very likely live on the outer edges of the phase space of the storage ring, and there most certainly are correlations between average radius, drift time and detector efficiencies. This effect has been studied in [9], and an upper limit of 0.04 ppm is set for both the low- and high-n data sets.

The systematic uncertainties discussed here were calculated assuming a fit start time of 30 μs. Since on average the fit start times is $\sim 25\mu s$ in this analysis, we must scale up the error to account for the effect of starting our fits earlier by $5\mu s$. Extrapolating the muon loss function backward by 5 μs, we find that the total fraction of lost muons increases by $\sim$ 18%. Therefore, the systematic error due to lost muons is estimated to be 0.11 ppm for the low-n data set and 0.083 ppm for the high-n data set.

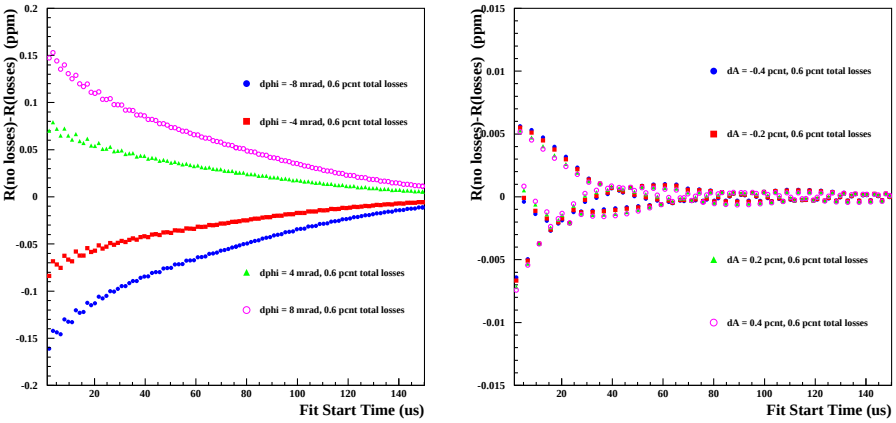

Figure 3.39: Effect on R vs. fit start time of muon losses assuming a 5% total loss and different average g-2 phases (left) and different average asymmetries (right). The nominal average g-2 phase in the simulated spectrum is 1.5 rad, and that of the asymmetry is 0.4.

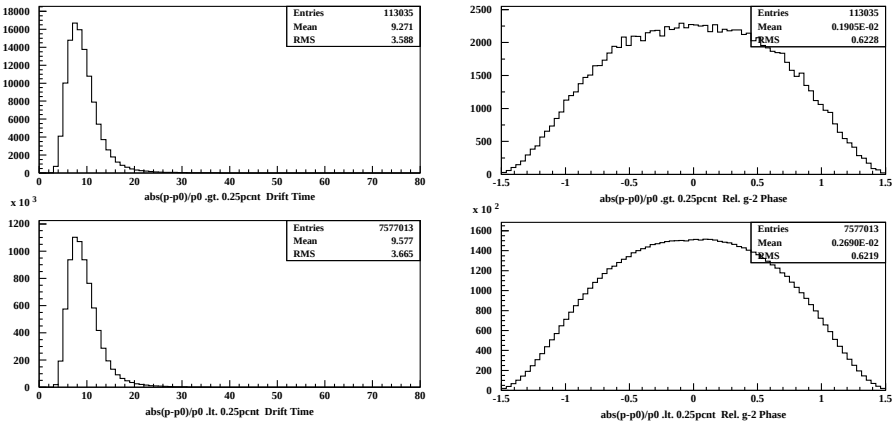

Figure 3.40: Drifttimes (left) and relative g-2 phases (right) of decay electrons in `G2GEANT` born in the outermost and innermost regions of the storage ring (top) and those born in the central regions. An energy cut of $E > 1.9$ GeV is enforced.

Finally, there is an additional acceptance effect due to lost muons, independent of the spin effect discussed above, which is due to the different phase-space distributions of the average stored muon and the average lost muon. This issue, first raised by Semertzidis, had been ignored in previous years because it was assumed that the g-2 phase dependence on the vertical position of the decay electron at birth is about the same as that for the radial position. However, as was discovered in late September of 2003, the phase depends quite heavily on the vertical position a factor of 5-6 times greater than on the radial position (this general effect became known as the Farley Effect, and in the case of lost muon, the Farley Effect for Lost Muons). To estimate the size of this effect, `g2track` was again utilized to determine the phase-space distribution of the lost muons. The details of this study may be found in [9]. We use $< \phi > (x, y)$ obtained from `G2GEANT` to calculate the difference between $< \phi >_{stored}$ and $< \phi >_{lost}$, and use the same simulation above to estimate the systematic shift in R. An upper limit of 0.04 ppm at $30\mu s$ is set for both data sets, therefore for the start times used in this analysis this becomes 0.05 ppm.

3.6 Others

"Others" includes systematic errors due to fill selection, bin width effects, fast rotation randomization, timing shifts, vertical oscillations and double CBO (both will be lumped into one "other BO" category, where BO stands for betatron oscillations), choice of g-2 period in shifting the time spectra for the ratio method, fit procedure and AGS background.

As discussed in Section 1.2, various cuts were made on each fill in order to filter out such potential problems as laser contamination, quad sparking, misreading the t0 pulse, and narrow pulse contamination. If one were able to assume that these cuts are 100% efficient, then we would not need to assign any systematic error on the precession frequency. However, as has been shown in the past, when the date rate flowing through the DAQ is very high, 'hiccups' can occur where the data is misread or fills become misaligned between the various crates. Therefore, for example, one could be reading out fill number 27 from some detectors, yet be reading out fill number 26 from others. The chance of this occurring is extremely small, yet still non-zero, and if this were to occur, then there is the possibility of using some data that is contaminated in some way.

During the run selection process, Chris Polly looked for coincidences between various non-contiguous detectors in order to eliminate runs that may have a large amount of laser contamination. The idea is that if after applying a cut on the laser flag one finds many coincidences between detectors, then it is very likely that the laser flag was misread. No laser runs were found that showed a large number of coincidences when the laser flag was not set, therefore we may assume the laser cut to be 100% efficient.

Unfortunately, we do not really know if there were other DAQ hiccups in the other non-laser runs. We can, however, estimate the level of contamination

from Chris' work: he finds 0 DAQ hiccups by looking at approximately 1.2×10^7 pulses. There are approximately 80 pulses on average per fill, therefore this means Chris looked at approximately 150,000 fills. Therefore we set an upper limit (or estimate) on the fraction of DAQ hiccups in the data set as approximately 7 ppm.

To set an upper limit on the systematic errors on R due to quadrupole cut inefficiencies, five-parameter time spectra were created where the decay electrons were truncated at 225 μs after injection. This would happen if, for example, the quadrupoles failed during a fill and the quadrupole cuts failed to catch this. The truncated data was added in to the time spectrum at the level of 10 and 50 ppm. Fitting the data to the 3-parameter ratio function we find the largest error in R to be less than 0.00005 ppm.

The t0 cut applied to each fill requires that the t0 has a non-zero value between 50-65 μs, and that the amplitude of the t0 pulse in the WFD is greater than 30. The relationship between these three requirements was investigated, and it was found that if any of the three t0 cuts fail, all three fail; they are 100% correlated. Therefore the only way that the t0 could be wrong is if, due to a DAQ hiccup, the wrong t0 time is used. However, the distribution of t0 per fill is fairly narrow, with a width of a few nanoseconds. Using a 'wrong' t0 would therefore mean using a t0 that is shifted by a nanosecond or two, which would only dilute the g-2 asymmetry in the data (thereby increasing the statistical error), and would cause no early-late shift. We therefore may safely ignore this issue.

Since the narrow pulse cut was applied rather late in the analysis, we may compare the fit results from before and after the cut was applied. The final results changed by 0.2 ppm for the low n-value data, and less than 0.05 ppm for the high n-value data. The narrow pulse cut is based on Qinzeng Peng's narrow pulse studies, and he finds[10] that of the 19,617 and 4,652 two-peak narrow pulses above 1.8 GeV that he finds in the low and high n-value data respectively, 268 and 128 two-peak narrow pulses remain after applying a cut on the average fit χ^2 per fill. Therefore we may assume that the cut is approximately 1.4% and 2.8% inefficient for the low and high n-value data sets respectively. Therefore, we obtain a systematic error on R due to two-peak narrow pulse contamination of 0.003 and 0.001 ppm for low and high n respectively.

The effect of bin width has been studies in past years, and there is no reason we should not be able to use those results for this year's analysis. We therefore use 0.05 ppm as our systematic error due to binning effects for both data sets.

Five different random seeds were used for fill randomization, therefore five different values of R were determined. We use $RMS(R)/\sqrt{5-1}$ to determine the systematic error due to randomization and find 0.03 ppm for the low n-value data set and 0.09 ppm for the high n-value data set.

The systematic error on R due to timing shifts in the pick-off time of pulses from the detectors has been determined by Rob Carey to be 0.02 ppm [11].

Besides radial CBO, the counting rate is also modified by other betatron frequencies. The three other dominant oscillations are at the frequency of twice the radial CBO frequency (dubbed DCBO), which comes from the radial "breath-

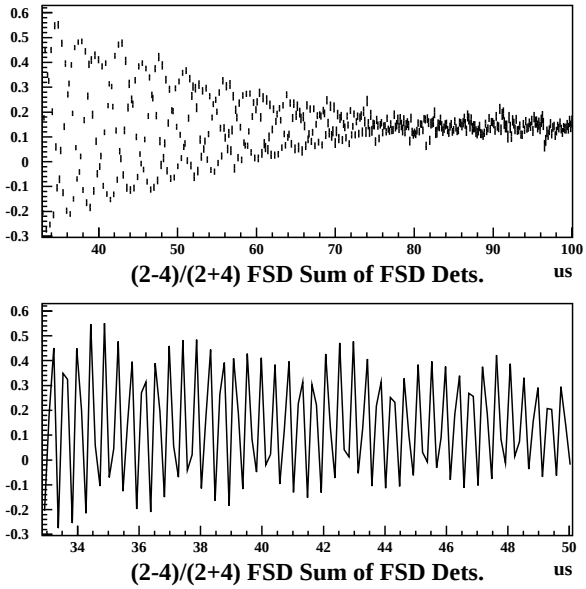

Figure 3.41: Vertical oscillations as seen by the FSDs by looking at the differences between tiles 2 and 4 as a function of time. Top: Sum of all "tile 2 - tile 4" time spectra from 33-100 μs. Bottom: Same as top, but from 33-50 μs, where the VBO oscillations are more easily seen.

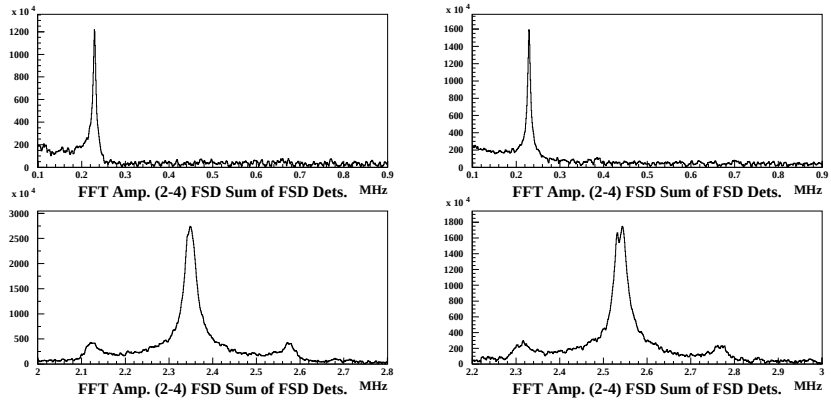

(a) Low n-value data.

(b) High n-value data.

Figure 3.42: FFT of "tile 2 - tile 4" time spectra. Top: low frequency range, showing a g-2 peak. Bottom: high frequency range, showing the vertical BO peak.

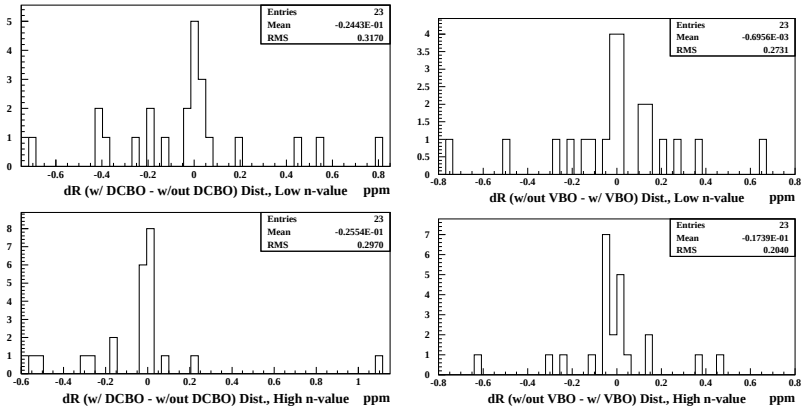

(a) Double CBO.

(b) Vertical BO.

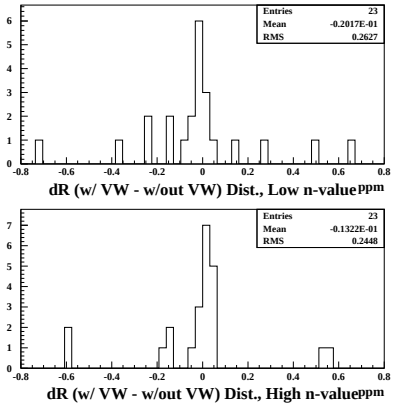

(c) Vertical Waist.

Figure 3.43: Effect on the fit values of R when neglecting the various OBO terms. $dR = R_{obo} - R_9$, where R_obo is the fit value of R with the OBO term included, and R_9 is the nominal fit value of R from the 9-parameter fit function.

ing" of the beam, where the width of the beam oscillates, the vertical breathing of the beam (dubbed VW for vertical waist) and the vertical oscillation frequency. These oscillations die-off rather rapidly, and are only seen in the data at very early times after injection. All oscillation frequencies are seen in the early-time residuals of fits of the data at late times, but the radial breathing of the beam has also been seen in the fiber harps, and the vertical oscillations are also seen by the FSDs when one takes the difference of the time spectra of FSD tiles 2 and 4 (see Fig. 3.41-3.42). It should be noted that the vertical breathing of the beam was not seen by the FSDs when looking at other combinations of FSD tiles (ie: 3-2-4), however the frequency appears as a clear peak in the FFT of the early-time residuals of the fits to the data.

The effect of DCBO was added to the fit function by modifying Eq. 2.27 to

$$f_0(t) = (1 + A_{N_c}(t) + A_{N_{dcbo}}(t))(1 + A(1 + A_{A_c}(t)) \cos(\omega_a t + \phi_a(1 + A_{\phi_c}(t)))) \tag{3.10}$$

where

$$A_{N_{dcbo}}(t) = A_{N_{dcbo}} e^{-2t/\tau_c} \cos(2\omega_c t + \phi_{N_{dcbo}}) \tag{3.11}$$

$f_{\pm}(t)$ were modified similarly. Note that the lifetime of DCBO is fixed to half the lifetime of the radial CBO, and the frequency is fixed to twice the radial CBO frequency. The plots in Fig. 3.43(a) show the dR distributions for both data sets between fitting for DCBO and not fitting DCBO. The mean systematic error for both data sets is $\sim$0.025 ppm.

Vertical oscillations were treated similarly by modifying Eq. 2.27 to

$$f_0(t) = (1 + A_{N_c}(t) + A_{N_{vbo}}(t))(1 + A(1 + A_{A_c}(t)) \cos(\omega_a t + \phi_a(1 + A_{\phi_c}(t)))) \tag{3.12}$$

where

$$A_{N_{vbo}}(t) = A_{N_{vbo}} e^{-t/\tau_{vbo}} \cos(\omega_{vbo} t + \phi_{N_{vbo}}) \tag{3.13}$$

$f_{\pm}(t)$ were modified similarly. The VBO lifetime is fixed to 28 μs, obtained from fits to the FSD tile 2-tile 4 spectra, and the VBO frequency is calculated given the assumed CBO frequency in the fit:

$$f_{vbo} = 6.703 \times \sqrt{1 - (1 - (f_c/6.703))^2} \tag{3.14}$$

where 6.703 is the cyclotron frequency in MHz and f_c is the assumed CBO frequency. The plots in Fig. 3.43(b) show the dR distributions for both data sets between fitting for VBO and not fitting VBO. The mean systematic error for the low n-value data set is less than 0.01 ppm and $\sim$ 0.02 ppm for the high n-value data set.

Finally, the vertical waist was treated the same was a vertical oscillations, with $A_{N_{vbo}}(t)$ replaced with $A_{N_{vw}}(t)$, f_{vbo} replaced with f_{vw} (calculated from the assumed CBO frequency in the fit) and τ_{vw} is set to 20 μs. The VW lifetime was obtained by fitting the relative FFT amplitudes of the VW peak as a function of time, where the FFT spectra binned in separate g-2 periods (that is, FFT of residuals from 20-24.365, 24.365-28.73, etc.) The plots in Fig.

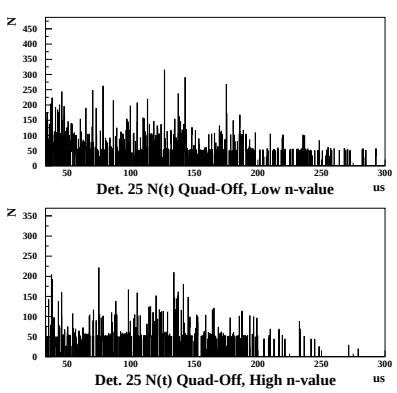

(a) Quad-off time spectra for both data sets.

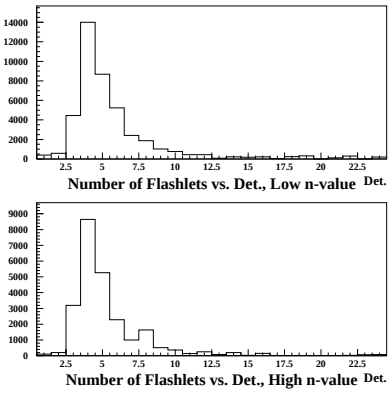

(b) Number of flashlets vs. detector for both data sets.

Figure 3.44: Quad-off time spectra, from 33-300 μs after injection, summed over all detectors, and the number of flashlets as a function of detector number for both data sets. Note that the quads were turned off every 49^{th} fill, therefore all entries in the $N(t)$ histogram have been scaled up by a factor of ~ 49. As expected, those detectors closest to the injection point have the highest number of flashlets.

3.43(c) show the dR distributions for both data sets between fitting for VW and not fitting for it. The mean systematic error due to ignoring VW in the fits is $\sim$ 0.02 ppm for both data sets. Adding all error in quadrature, we find the total systematic error on R due to other BO for the low n-value data set is 0.03 ppm, and 0.04 ppm for the high n-value data set.

The ratio method relies on knowledge of the g-2 period to within some accuracy in order to shift the time spectra appropriately without oscillation. Seven time ratio spectra were produced where the data was shifted using assumed g-2 periods of

$$T_a(1 - (n-4)7 \times 10^{-6}) \tag{3.15}$$

where $n = 1, 2...7$ and T_a is the actual g-2 period used in generating the time spectrum; therefore the maximal difference between assumed and true g-2 periods is ± 21 ppm. It was found that the fit results for R for these time spectra (21 ppm off from the true value) differ by no more than $\pm 4 \times 10^{-5}$ ppm from fits to the spectrum that used the true value of the g-2 period in shifting the time spectra. The g-2 period used in shifting the actual data is within 6 ppm of the fit result for R. Therefore we argue that this systematic error does not even need to be listed, since it is orders of magnitude smaller than all other systematic errors.

In the 2001 data run, the quadrupoles were turned off periodically; these

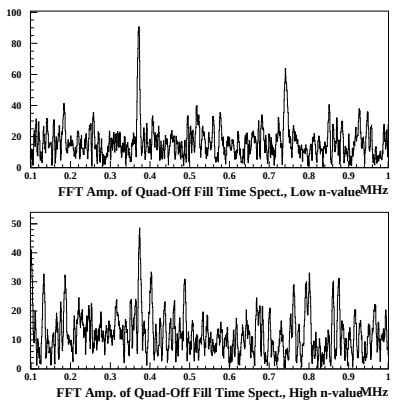

(a) Low frequency range (0.1-1.0 MHz).

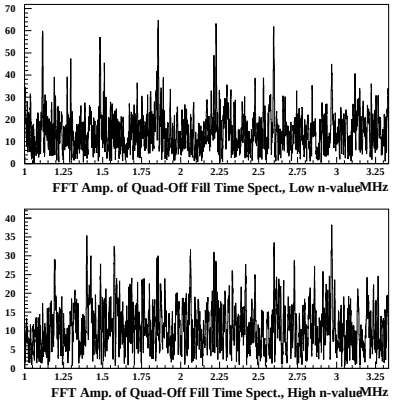

(b) High frequency range (1.0-3.33 MHz).

Figure 3.45: FFT amplitudes of the quad-off time spectra for both data sets in different frequency ranges. Note the AGS cyclotron frequency of ~ 370 kHz and its harmonics.

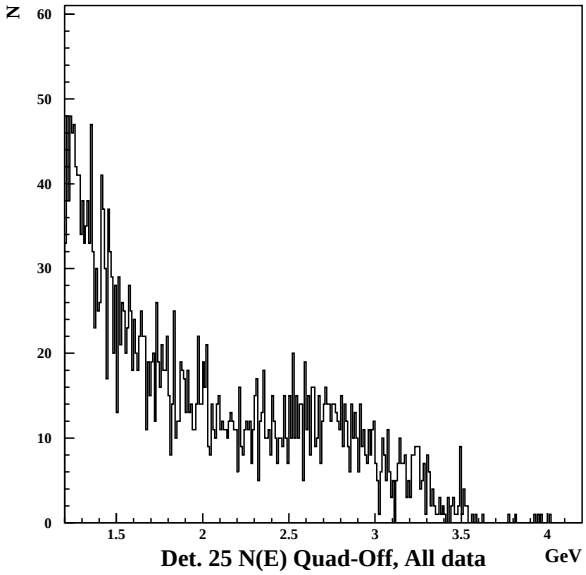

Figure 3.46: Flashlet energy spectrum, from 1.2-4.2 GeV.

'quad-off' fills allowed us to measure the time and energy spectra of the AGS background (a.k.a. flashlets). On the left of Fig. 3.44, the quad-off time spectra for both n-value data sets are shown, and on the right the distributions of flashlet contamination around the ring (number of flashlets vs. detector) for both data sets are shown. The time spectra were built applying the usual energy cuts, and they were later scaled-up by a factor of ~ 49 (since the quads were turned off only once every 49 fills). The FFTs of the the quad-off time spectra are shown in Fig. 3.45, the left plots showing the frequency spectra in the range of 100-1000 kHz, and the right plots showing the frequency spectra in the range of 1-3.3 MHz. The AGS cyclotron frequency of $\sim 370kHz$ and its harmonics are clearly distinguished; note also that there is no peak above noise at the g-2 frequency. The energy spectrum of the flashlets is shown in Fig. 3.46.

To determine the effect of AGS background on the fit value of R, the quad-off time spectra were added to the quad-on time spectra, with multiplicative factors of -1.5, -1, -0.5, 0, 0.5, 1, and 1.5. Therefore, the multiplicative factor of -1 essentially subtracted out the AGS background from the data, and the factor of 1 doubled the amount of AGS background in the data. These time spectra were then fit to the 9-parameter ratio function; the largest difference seen between fit R values from any of the fits was less than 0.01 ppm. We therefore claim a 0.01 ppm systematic error on R due to AGS background.

In Chris Polly's ω_a analysis, he found it necessary to add an extra term to the fit function to account for the beam's upward motion at early fit start times due to the turn-off of scraping. This is an acceptance correction to N_0, with an exponential lifetime of $\sim 5\mu s$. Although no such term has been found necessary in this ratio-based analysis (neither the residuals of fits at early times nor the fit χ^2 show a 5 μs time-dependence), the effect was investigated by adding the term to the fit function (making a 10-parameter ratio function) and fitting the sum of all early-detectors at the nominal fit start time (23 μs). The χ^2s of the fits with this term do not improve significantly ($\Delta\chi^2/d.o.f. < 1 \times 10^{-4}$), and the change in R is less than 0.001 ppm for both data sets. Therefore, we claim no systematic effect due to beam relaxation in this analysis.

In this analysis, limits were set on all fit parameters in order to ensure fit parameter stability and χ^2 minimization convergence. However this can be problematic with `MINUIT`, since if a parameter is found to be at or near its limit then `MINUIT` cannot properly evaluate the error on the parameter. Fairly loose limits were set on the *important* parameters, ie: A and R, and ϕ_a had limits from 0 to 2π. The CBO amplitudes all had limits from 0 to 10 times the 'typical' amplitudes found from the fits, and the cbo phases were also limited to fall within 0 to 2π. Occasionally in the fit start time scans some of the CBO parameters were found to be at or very close to their limits. However, R was never found anywhere near its limits (-200 to 200, where they typical value of R was -25).

Still, to be sure that the value and errors of R were not systematically pulled, a study was done where the limits on R were removed. About 90% of the fits converged, and the average difference between those R values found with limits and those found without was $\sim -0.04 \pm 0.07$ ppm. An order of magnitude

Values of Fit Parameters		
Fit Param.	Low-n Fits	High-n Fits
A	$0.3814 \pm 3.068 \times 10^{-5}$	$0.3812 \pm 3.674 \times 10^{-5}$
ϕ_a	$3.0322 \pm 1.4438 \times 10^{-4}$	$3.0323 \pm 1.746 \times 10^{-4}$
A_{N_c}	$(9.22 \pm 0.958) \times 10^{-3}$	$(1.28 \pm 0.139) \times 10^{-2}$
A_{A_c}	$(2.50 \pm 0.247) \times 10^{-3}$	$(3.05 \pm 0.245) \times 10^{-3}$
A_{ϕ_c}	$(6.62 \pm 0.826) \times 10^{-4}$	$(5.80 \pm 0.768) \times 10^{-4}$
$\chi^2/d.o.f.$	22.49/22	36.72/22

Table 3.1: Average (over 23 detectors) values of the fit parameters for the 9-parameter ratio fit. Results are for one random seed, however χ^2's are averaged over 5 random seeds.

smaller average difference (and also consistent with zero) was found between the *errors* on R. Similar studies were done where not only the limits on R were removed, but also the limits on the CBO amplitudes were removed, and similar average differences (~ 0.04 ppm) were found. We therefore set the systematic error on R due to fit procedure at 0.04 ppm.

3.7 Summary

Table 3.1 summarizes the average values of the asymmetry, phase and CBO amplitudes determined from the 9-parameter ratio fits.

The final R values determined from both data sets are very consistent with each other: $R_{low} = 108.21 \pm 0.91$ ppm, $R_{high} = 108.42 \pm 1.10$ ppm and $R_{SB} = 110.55 \pm 3.73$, where the errors are statistical. Table 3.2 summarizes the systematic errors on R for both data sets. The systematic errors for the "S+B" data set are for the most part assumed to be the same as for the "golden" low-n subset with a few exceptions: the muon loss systematic error is conservatively estimated to be twice the size for the S+B data set than for the golden low-n data set due to the expected increase in the fraction of lost muons (less scraping and lower kick = more losses), and the randomization systematic error is obtained from the spread of R values found using five random seeds.

The systematic uncertainties due to beam dynamics include differential decay, $d < y > /dt$ and $d < \sigma_y > /dt$. "CE" and "CP" refer to the uncertainties in the radial electric field and pitch corrections respectively that will be applied to ω_a. In calculating the total systematic error, we currently assume the individual systematics errors are uncorrelated, and therefore all errors are added in quadrature to obtain a total systematic uncertainty of 0.22 for all data sets combined.

Systematic Error Table (all units in ppm)					
Syst. Error	Low-n	High-n	Low+High	S+B	L+H+S+B
ESC	0.01	0.02	0.01	0.01	0.01
WW	0.1	0.1	0.1	0.1	0.1
Pileup	0.06	0.05	0.05	0.06	0.05
CBO	0.06	0.12	0.08	0.06	0.08
Muon Losses	0.12	0.09	0.11	0.24	0.12
Random-ization	0.04	0.05	0.04	0.18	0.05
Timing Shifts	0.02	0.02	0.02	0.02	0.02
Bin Width	0.05	0.05	0.05	0.05	0.05
Other BO	0.03	0.04	0.03	0.03	0.03
AGS Bgnd	0.01	0.01	0.01	0.01	0.01
Fit Procedure	0.04	0.04	0.04	0.04	0.04
Fill Cuts	0.01	0.01	0.01	0.01	0.01
CE & CP*	0.06	0.06	0.06	0.06	0.06
Beam** Dynam.	0.05	0.05	0.05	0.05	0.05
Total Syst. Error	0.21	0.22	0.21	0.35	0.22
Stat. Error	0.91	1.10	0.70	3.73	0.689

Table 3.2: Summary of systematic errors for the various individual and combined data sets. All units are in ppm. * See [1]. ** From studies by W. Morse, D. Hertzog, C. Polly, Q. Peng, R. Carey and J. Miller.

Appendix A

The Ratio Method - Derivations

A.1 Simple 3-Parameter Function

This is derived from the simple 5-parameter function for N(t),

$$N_5(t) = N_0 e^{-t/\tau}(1 + A\cos(\omega_a t)) \tag{A.1}$$

where we have set ϕ_{g-2} equal to zero for simplicity (it will of course be added in later).

Let

$$u_+(t) = N_5(t + T/2) = N_0 e^{-t/\tau} e^{-T/2\tau}(1 - A\cos(\omega_a t + \delta)) \tag{A.2}$$

and

$$u_-(t) = N_5(t - T/2) = N_0 e^{-t/\tau} e^{T/2\tau}(1 - A\cos(\omega_a t - \delta)) \tag{A.3}$$

where T is a good approximation of the g-2 period (to about 5-10 ppm) and δ is the difference between T and T_{true}, $\delta = \frac{\omega_a}{2}(T - T_{true}) = \pi \times \delta T$.

Now let

$$v_1(t) = v_2(t) = N_5(t) \tag{A.4}$$

$$U(t) = u_+(t) + u_-(t) \tag{A.5}$$

$$V(t) = v_1(t) + v_2(t) \tag{A.6}$$

$$r(t) = \frac{V(t) - U(t)}{V(t) + U(t)} \tag{A.7}$$

Expanding $e^{\pm T/2\tau}$ and $A\cos(\omega_a t \pm \delta)$, we find

$$\begin{aligned} u_+(t) &= N_0 e^{-t/\tau}\left(1 - \frac{1}{2}\frac{T}{\tau} + \frac{1}{2}\left(\frac{1}{2}\frac{T}{\tau}\right)^2 - \ldots\right) \times \\ &\quad \big(1 - A\cos(\omega_a t) + A\delta\sin(\omega_a t)\big) \end{aligned} \tag{A.8}$$

$$\begin{aligned} u_-(t) &= N_0 e^{-t/\tau}\left(1 + \frac{1}{2}\frac{T}{\tau} + \frac{1}{2}\left(\frac{1}{2}\frac{T}{\tau}\right)^2 + \ldots\right) \times \\ &\quad \big(1 - A\cos(\omega_a t) - A\delta\sin(\omega_a t)\big) \end{aligned} \tag{A.9}$$

and so,

$$\begin{aligned} U(t) &= 2N_0 e^{-t/\tau}\left(1 + \frac{1}{2}\left(\frac{1}{2}\frac{T}{\tau}\right)^2\right)\big(1 - A\cos(\omega_a t)\big) - \\ &\quad N_0 e^{-t/\tau}\frac{T}{\tau}A\delta\sin(\omega_a t) \end{aligned} \tag{A.10}$$

Now let

$$C_1 = \frac{1}{16}\left(\frac{T}{\tau}\right)^2 \simeq 2.87 \times 10^{-4}, \tag{A.11}$$

and

$$C_2 = \frac{TA\delta}{4\tau} \simeq 2 \times 10^{-7} \tag{A.12}$$

then,

$$\begin{aligned} V(t) - U(t) &= 4N_0 e^{-t/\tau}\left(A\cos(\omega_a t) + C_2\sin(\omega_a t)\right) - \\ &\quad 4N_0 e^{-t/\tau}C_1(1 - A\cos(\omega_a t)) \end{aligned} \tag{A.13}$$

$$\begin{aligned} V(t) + U(t) &= 4N_0 e^{-t/\tau}\left(1 - C_2\sin(\omega_a t)\right) + \\ &\quad 4N_0 e^{-t/\tau}C_1(1 - A\cos(\omega_a t)) \end{aligned} \tag{A.14}$$

$$\begin{aligned} r(t) &= \frac{A\cos(\omega_a t) + C_2\sin(\omega_a t)) - C_1(1 - A\cos(\omega_a t))}{(1 - C_2\sin(\omega_a t)) + C_1(1 - A\cos(\omega_a t))} \\ &= \frac{A'\cos(\omega_a t) - C_1 + C_2\sin(\omega_a t)}{1 - C_2\sin(\omega_a t) + C_1(1 - A\cos(\omega_a t))} \end{aligned} \tag{A.15}$$

where $A' = A(1 + C_1)$

Since the terms in the denominator are small, we can rewrite this as

$$\begin{aligned} r(t) &= (A'\cos(\omega_a t) - C_1 + C_2\sin(\omega_a t)) \times \\ &\quad (1 - C_1(1 - A\cos(\omega_a t)) + C_2\sin(\omega_a t)) \end{aligned} \tag{A.16}$$

Keeping terms to first order, we have

$$\begin{aligned} r(t) &= A'\cos(\omega_a t) - C_1 + C_2\sin(\omega_a t) - C_1 A'\cos(\omega_a t) + \\ &\quad C_1 A A'\cos^2(\omega_a t) + C_2 A'\sin(\omega_a t)\cos(\omega_a t) \\ &= A''\cos(\omega_a t) - C_1 + C_2\sin(\omega_a t) + \\ &\quad C_2 A'\cos(\omega_a t)\sin(\omega_a t) + C_1 A A'\cos^2(\omega_a t) \end{aligned} \tag{A.17}$$

where

$$A'' = A'(1 - C_1) = A(1 - C_1^2) \tag{A.18}$$

Terms involving C_2 are of order 10^{-7} or less, and so may be neglected, and we are left with

$$r(t) = A''\cos(\omega_a t) - C_1 + C_1 A A'\cos^2(\omega_a t) \tag{A.19}$$

In practice, the last term is omitted, so that

$$r(t) = A\cos(\omega_a t) - C_1 \tag{A.20}$$

Verification of the above derivation can be easily done using simulation. We have produced time spectra according to Eqn. [A.1] for 3.6 billion muon decays, with an energy range of 2-2.9 GeV. The energy dependence of the asymmetry is taken into account. We have fit both the normal time spectrum with the five parameter function A.1 and the ratio time spectrum with the three parameter function A.20. The input parameters are: $\tau_\mu = 64.4\mu s$, $R = 15.0ppm$, and $\phi = 1.5rad$. The fit results are shown in Figures A.1 and A.2. Both methods of obtaining R give acceptable results (good χ^2, consistant R vs fit start time, etc.).

A.2 Derivation of the Ratio Function with a Background Term

Here we assume a background term $B(t)$ such that

$$N(t) = N_5(t) + B(t) \tag{A.21}$$

where $B(t)/N_5(t) \ll 1$. Eq. A.15 from the previous derivation is then modified to be

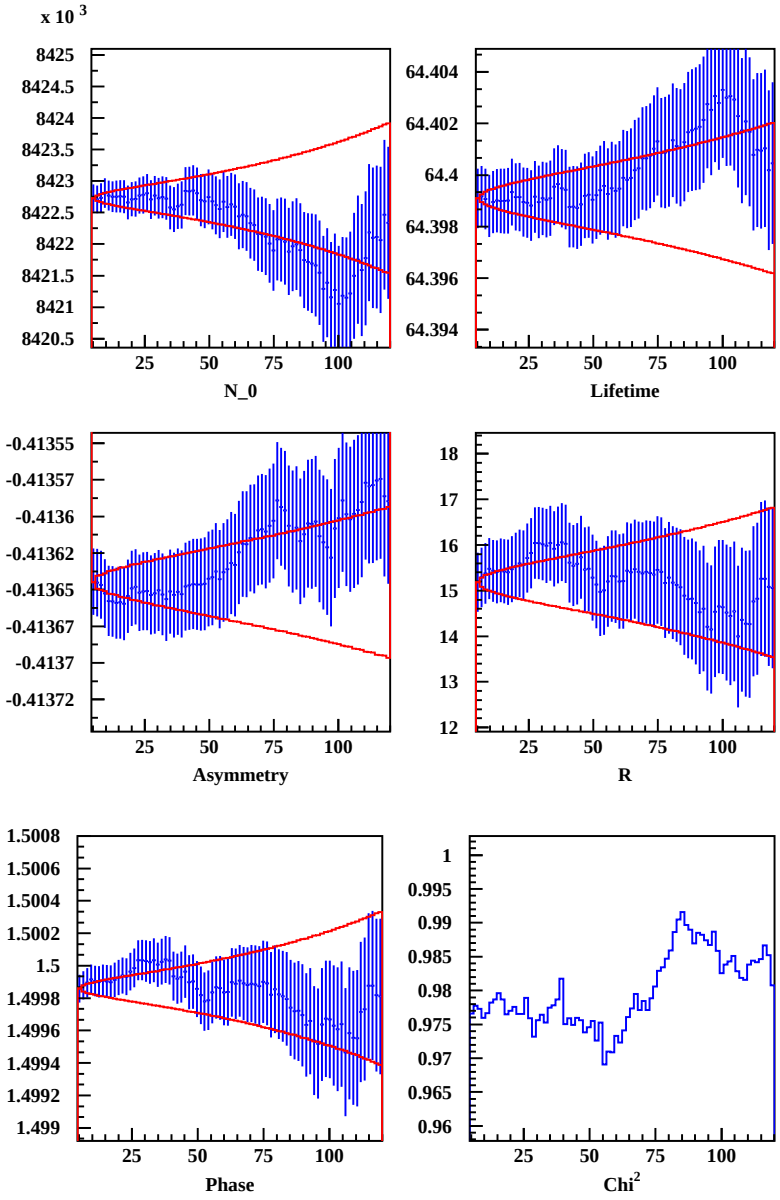

Figure A.1: Fit results to simulated data. The simulated spectrum is derived from a random distribution according to Eq. A.1, and fit to a 5 parameter function. The fitted values of the parameters of the function are plotted vs. starttime of the fit. The red lines are the correlated error bands.

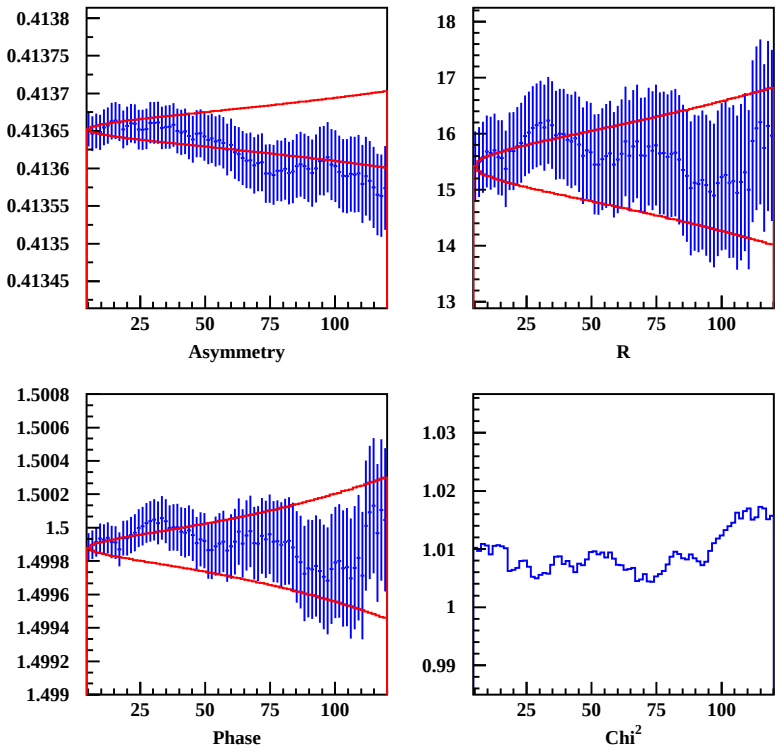

Figure A.2: Fit results to simulated data. The simulated spectrum is derived from a random distribution according to Eq. A.1, rearranged according to Eq. A.7 and fit to the 3 parameter function A.20. The fitted values of the parameters of the function are plotted vs. starttime of the fit. The red lines are the correlated error bands.

$$r(t) = \frac{A\cos(\omega_a t) + C_2\sin(\omega_a t)) - C_1(1 - A\cos(\omega_a t)) + b_{num}(t)}{(1 - C_2\sin(\omega_a t)) + C_1(1 - A\cos(\omega_a t)) + b_{den}(t)}$$

$$= \frac{A'\cos(\omega_a t) - C_1 + C_2\sin(\omega_a t) + b_{num}(t)}{1 - C_2\sin(\omega_a t) + C_1(1 - A\cos(\omega_a t)) + b_{den}(t)} \quad \text{(A.22)}$$

where

$$b_{num}(t) = \frac{2B(t) - B(t + T/2) - B(t - T/2)}{4N_0 exp(-t/\tau)} \quad \text{(A.23)}$$

and

$$b_{den}(t) = \frac{2B(t) + B(t + T/2) + B(t - T/2)}{4N_0 exp(-t/\tau)} \quad \text{(A.24)}$$

Therefore, the ratio becomes, neglecting the same terms as before but keeping the background terms to first order,

$$r(t) = A\cos(\omega_a t)(1 - b_{den}(t)) - C_1 + b_{num}(t) \quad \text{(A.25)}$$

From this result one immediately sees that if the background term is large enough, the fit result for ω_a will be fit-start-time dependent. We also see that any background that oscillates, such as pileup and CBO, will produce "beat frequencies" in the ratio time spectrum. Pileup will produce beat frequencies of $f_{beat} = 0$ and $f = 2f_a$, whereas CBO will produce beat frequencies of $f_{beat} = f_{cbo} \pm f_a$. If a beat frequency sits close to the actual g-2 frequency f_a, then fits to the data that do not have background subtracted or fits to the data with a simple three-parameter function will show oscillations in the fit value of ω_a at frequencies $f = f_{beat} \pm f_a$. This is readily seen when the 2001 data set is fit to the three-parameter ratio function: ω_a oscillates vs. fit start time at frequencies $f \simeq 40$ kHz and $f \simeq 32$ kHz for the low- and high-n data sets respectively.

Another, perhaps more subtle, expectation is $g - 2$ oscillations in difference plots of ω vs. fit start time with a *non-oscillating* background "removed" (either subtracted or fitted out) and the background left in. A good example of this is gain or ESC corrections; since gain or ESC effects N_0, τ and in particular A versus time, one finds that $b_{den}(t) \propto \cos(\omega_a t)$. Therefore, in the fit-start-time scan of ω_a with the background left in, ω_a will have small oscillations at $f = 2f_a$ (since $\cos(\omega_a)^2 = \frac{1}{2}(1 + \cos(2\omega_a))$) and the fit-start-time scan of ω_a with the background term removed will either have no oscillations at this frequency or at least oscillations of a much smaller amplitude. When looking at (R(corr.) vs. t) − (R(no corr.) vs. t), one expects to see oscillations at twice the g-2 frequency. This is indeed the case, as shown in Fig. 3.17.

A.3 A General Derivation of the Ratio Function with CBO

From past experience, we know that Eq. A.1 is not sufficient to obtain stable fit results from the data. This is because the counting rate is changed by other effects, primarily those from detector gains, muon losses, and coherent betatron oscillations (CBO). The ratio method is largely insensitive to detector gains and muon losses, however it is not blind to CBO.

Assume that the number, asymmetry and phase are affected by CBO. Then the number of decay electrons or positrons as a function of time is in general written as:

$$N(t) = (N_0 + N_{cbo}(t))e^{-t/\tau}[1 + (A + A_{cbo}(t))\cos(\omega_a t + \phi + \phi_{cbo}(t))] \quad \text{(A.26)}$$

Assuming that the effect of CBO is small, we expand Eqn. A.26 out and keep terms to only first order:

$$\begin{aligned} N(t) &= (N_0 + N_{cbo}(t))e^{-t/\tau}[1 + A\cos(\omega_a t + \phi) + A_{cbo}(t)\cos(\omega_a t + \phi) - \\ &\quad A\phi_{cbo}(t)\sin(\omega_a t + \phi)] \\ &= N_0 e^{-t/\tau}(1 + A\cos(\omega_a t + \phi))\left(1 + \frac{N_{cbo}(t)}{N_0}\right) + \\ &\quad N_0 e^{-t/\tau}\left(1 + \frac{N_{cbo}(t)}{N_0}\right)(A_{cbo}(t)\cos(\omega_a t + \phi)) - \\ &\quad A\phi_{cbo}(t)\sin(\omega_a t + \phi)) \\ &= N_5(t)\,(1 + f_1(t) + f_2(t)) \\ &= N_5(t)\,(1 + f_{cbo}(t)) \end{aligned} \quad \text{(A.27)}$$

where

$$f_1(t) = \frac{N_{cbo}(t)}{N_0}, \quad \text{(A.28)}$$

$$f_2(t) = \frac{A_{cbo}(t)\cos(\omega_a t + \phi)) - A\phi_{cbo}(t)\sin(\omega_a t + \phi)}{1 + A\cos(\omega_a t + \phi)}, \quad \text{(A.29)}$$

and

$$f_{cbo}(t) = f_1(t) + f_2(t) \quad \text{(A.30)}$$

Eqn. A.27 is equivalent to having a background term,

$$N(t) = N_5(t) + B(t) \quad \text{(A.31)}$$

where

$$B(t) = N_5(t) \cdot f_{cbo}(t) \quad \text{(A.32)}$$

In the previous section it was shown that with a background term $B(t)$, Eqn. A.20 becomes:

$$r(t) = [1 - b_{den}(t)]\, A\cos(\omega_a t + \phi) - C_1 + b_{num}(t) \tag{A.33}$$

where

$$b_{den}(t) = 2b(t) + b_+(t) + b_-(t), \tag{A.34}$$

$$b_{num}(t) = 2b(t) - b_+(t) - b_-(t), \tag{A.35}$$

$$b(t) = \frac{B(t)}{4N_0 exp(-t/\tau)}, \tag{A.36}$$

$$b_+(t) = b(t + T/2), \tag{A.37}$$

and

$$b_-(t) = b(t - T/2), \tag{A.38}$$

Now,

$$\begin{aligned} b_+(t) + b_-(t) \quad = \quad & \frac{1}{4}\left(1 - \frac{T}{2\tau} + \frac{1}{2}\left(\frac{T}{2\tau}\right)^2\right)(1 - A\cos(\omega_a t)) \times \\ & f_{cbo}(t + T/2) + \\ & \frac{1}{4}\left(1 + \frac{T}{2\tau} + \frac{1}{2}\left(\frac{T}{2\tau}\right)^2\right)(1 - A\cos(\omega_a t)) \times \\ & f_{cbo}(t - T/2) \end{aligned} \tag{A.39}$$

where we have left out all terms with $A\delta\sin()$ since they are small compared to the $A\cos()$ terms, and the phase, ϕ is implied in all cosine terms. Since $f_{cbo}(t)$ is small, we keep only the highest order terms:

$$b_+(t) + b_-(t) = \frac{1}{4}\left(1 - A\cos(\omega_a t)\right)\left(f_{cbo}(t + T/2) + f_{cbo}(t - T/2)\right) \tag{A.40}$$

Similarly,

$$2b(t) = \frac{1}{2}\left(1 + A\cos(\omega_a t)\right) f_{cbo}(t) \tag{A.41}$$

Using Eqns. A.28 and A.29, we find that

$$\begin{aligned} b_+(t) + b_-(t) \quad = \quad & \frac{1}{4}(1 - A\cos(\omega_a t))\left(\frac{N_{cbo}(t + T/2) + N_{cbo}(t - T/2)}{N_0}\right) - \\ & \frac{1}{4}\left(A_{cbo}(t + T/2) + A_{cbo}(t - T/2)\right) \cdot \cos(\omega_a t) + \\ & \frac{1}{4}\left(A\phi_{cbo}(t + T/2) + A\phi_{cbo}(t - T/2)\right) \cdot \sin(\omega_a t) \end{aligned} \tag{A.42}$$

and again similarly,

$$2b(t) = \frac{1}{2}\left((1 + A\cos(\omega_a t))\frac{N_{cbo}(t)}{N_0} + A_{cbo}(t)\cos(\omega_a t) - A\phi_{cbo}(t)\sin(\omega_a t)\right) \tag{A.43}$$

Next, we look at b_{den} and b_{num}:

$$\begin{aligned} b_{den} &= 2b(t) + b_+ + b_- \\ &= \frac{1}{4}\left(\frac{2N_{cbo} + N_{cbo+} + N_{cbo-}}{N_0}\right) + \\ &\quad \frac{1}{4}\left(A\cos(\omega_a t)\frac{2N_{cbo} - N_{cbo+} - N_{cbo-}}{N_0}\right) + \\ &\quad \frac{1}{4}\left((2A_{cbo} - A_{cbo+} - A_{cbo-})\cos(\omega_a t)\right) - \\ &\quad \frac{1}{4}\left((2A\phi_{cbo} - A\phi_{cbo+} - A\phi_{cbo-})\sin(\omega_a t)\right) \end{aligned} \tag{A.44}$$

and

$$\begin{aligned} b_{num} &= 2b(t) - b_+ - b_- \\ &= \frac{1}{4}\left(\frac{2N_{cbo} - N_{cbo+} - N_{cbo-}}{N_0}\right) + \\ &\quad \frac{1}{4}\left(A\cos(\omega_a t)\frac{2N_{cbo} + N_{cbo+} + N_{cbo-}}{N_0}\right) + \\ &\quad \frac{1}{4}\left((2A_{cbo} + A_{cbo+} + A_{cbo-})\cos(\omega_a t)\right) - \\ &\quad \frac{1}{4}\left((2A\phi_{cbo} + A\phi_{cbo+} + A\phi_{cbo-})\sin(\omega_a t)\right) \end{aligned} \tag{A.45}$$

The above equations look a bit scary, but we can simplify them quite a bit. If one assumes $N_{cbo} \sim A_{cbo} \sim \phi_{cbo} \sim exp(-t/\tau_c)\cos(\omega_c t)$ and that τ_c is much greater than $T/2$, then since

$$\cos(\omega_c(t \pm T/2)) = \cos(\omega_c t)\cos(\omega_c T/2) \mp \sin(\omega_c t)\sin(\omega_c T/2) \tag{A.46}$$

we find that $N_{cbo+}+N_{cbo-} \simeq 2N_{cbo}\cos(\omega_c T/2)$, $A_{cbo+}+A_{cbo-} \simeq 2A_{cbo}\cos(\omega_c T/2)$ and $\phi_{cbo+} + \phi_{cbo-} \simeq 2\phi_{cbo}\cos(\omega_c T/2)$. Therefore we can rewrite Eqns. A.44 and A.45 as

$$\begin{aligned} b_{den} &= \frac{1}{2}\left(\frac{N_{cbo}}{N_0}(1+\xi) + A\cos(\omega_a t)\frac{N_{cbo}}{N_0}(1-\xi) + \right. \\ &\quad \left. A_{cbo}(1-\xi)\cos(\omega_a t) - \phi_c'(1-\xi)\sin(\omega_a t)\right) \end{aligned} \tag{A.47}$$

and

$$\begin{aligned} b_{num} &= \frac{1}{2}\left(\frac{N_{cbo}}{N_0}(1-\xi) + A\cos(\omega_a t)\frac{N_{cbo}}{N_0}(1+\xi) + \right. \\ &\quad \left. A_{cbo}(1+\xi)\cos(\omega_a t) - \phi_c'(1+\xi)\sin(\omega_a t)\right) \end{aligned} \tag{A.48}$$

where $\xi = \cos(\omega_c T/2)$ and $\phi_c' = A\phi_c$.

Several aspects of these results should be noted. First, when we took data with quadrupole focusing such that $T_{cbo} \simeq \frac{1}{2} T_{g-2}$ (ie: 1999 and 2000 runs), then many terms in b_{den} and b_{num} cancel since $\xi \simeq 1$. We end up with

$$b_{den} \simeq \frac{N_{cbo}}{N_0} \tag{A.49}$$

and

$$\begin{aligned} b_{num} \quad \simeq \quad & \left(A \cos(\omega_a t) \frac{N_{cbo}}{N_0} \right) + \\ & A'_{cbo} \cos(\omega_a t) - \phi'_{cbo} \sin(\omega_a t) \end{aligned} \tag{A.50}$$

Looking at Eqn. A.33 we see that all CBO terms involve products of $\cos(\omega_{cbo} t)$ with either $\cos(\omega_a t)$ or $\sin(\omega_a t)$, which reduce to some linear combination of $\cos((\omega_{cbo} - \omega_a)t)$ and $\cos((\omega_{cbo} + \omega_a)t)$. Note that there are **no** terms involving simply $\cos(\omega_{cbo} t)$! This is a rather unique result, and obviously does not apply to the 2001 data.

Next, the amplitude of the main cbo peak can in principle be either minimally zero or maximally the same size as would be seen in a multiparamter fit of the normal "wiggle" plot, which is the special case of the 2000 run conditions. Otherwise, the cbo amplitude should be suppressed by some factor in the ratio method. For the 2001 data, where $f_c \simeq$ 419 and 490 kHz, then $\xi \simeq$ -0.15 and 0.10 respectively and the suppression factor is ~ 2.

A.4 Error Propagation

In a counting measurement, the uncertainty in the number of counts within a time bin is simply the square root of the number of counts in that time bin, or, more precisely the square root of the function averaged over that time bin. Therefore, if one were to fit the data directly to a function $N(t)$, in a log-likelihood or χ^2 fit, the error on each bin is $\sqrt{N}$ or $\sqrt{N(t)}$. However, when fitting the data to a function $f(N(t))$, the uncertainty of that function must be determined.

The ratio is defined as

$$r(t) = \frac{V(t) - U(t)}{V(t) + U(t)} \tag{A.51}$$

where

$$V(t) = v_1(t) + v_2(t) = N_1(t) + N_2(t) \tag{A.52}$$

and

$$U(t) = u_+(t) + u_-(t) = N(t + T/2) + N(t - T/2) \tag{A.53}$$

It is important to note that $N_1(t)$, $N_2(T)$, $N(t + T/2)$, $N(t - T/2)$ are all statistically independent data sets. The uncertainty of the ratio at time t is therefore

$$\sigma_r(t)^2 = \left(\frac{\partial r(t)}{\partial V(t)} \right)^2 \delta V(t)^2 + \left(\frac{\partial r(t)}{\partial U(t)} \right)^2 \delta U(t)^2 \tag{A.54}$$

Now,

$$\frac{\partial r(t)}{\partial V} = \frac{1}{U+V} - \left(\frac{V-U}{(U+V)^2}\right), \tag{A.55}$$

$$\frac{\partial r(t)}{\partial U} = \frac{-1}{U+V} - \left(\frac{V-U}{(U+V)^2}\right), \tag{A.56}$$

$$\delta V^2 = \delta v_1^2 + \delta v_2^2 = v_1 + v_2 = V \tag{A.57}$$

and

$$\delta U^2 = \delta u_+^2 + \delta u_-^2 = u_+ + u_- = U \tag{A.58}$$

where both V and U are at time t. Therefore we find

$$\sigma_r^2 = \frac{4UV}{(V+U)^3} = \frac{1-r^2}{V+U} \tag{A.59}$$

The above is the correct derivation of the error propagation when no backgrounds are subtracted from the data. However, in this analysis, pileup events are statistically constructed from the data and then subtracted from the data set; therefore one must properly calculate the correct error bar due to subtracting a subset of correlated data from a set of data. This is determined in [5] for a multiparameter fit: the error at a given time t is increased by

$$\sigma_N^2 \rightarrow \sigma_N^2(1+\gamma e^{(t-t_0)/\tau}) \tag{A.60}$$

where γ is the product of the fraction of pileup events at t_0 and a "correlation" factor as described in [5], and τ is the pileup lifetime (32.2 μs). γ was determined for each detector in this data set at $t_0 = 32\mu s$; the typical value of γ is $\sim 1.04\%$.

However, one must first determine the proper functional form of the "correct" error of the ratio due to pileup subtraction. We begin with the modification of the errors on V and U.

$$\begin{aligned} \delta V^2 &= \delta v_1^2(1+\gamma(t)) + \delta v_2^2(1+\gamma(t)) \\ &= (v_1+v_2)(1+\gamma(t)) = V(1+\gamma(t)) \end{aligned} \tag{A.61}$$

where $\gamma(t) = \gamma e^{(t-t_0)/\tau}$, and

$$\begin{aligned} \delta U^2 &= \delta u_+^2(1+\gamma(t_+)) + \delta u_-^2(1+\gamma(t_-)) \\ &= u_+(1+\gamma(t)e^{-T/2\tau}) + u_-(1+\gamma(t)e^{T/2\tau}) \\ &\simeq (u_+ + u_-)\left(1+\gamma(t)\left(1+\frac{1}{2}\left(\frac{T}{2\tau}\right)^2\right)\right) \\ &= U\left(1+\gamma(t)\left(1+\frac{1}{2}\left(\frac{T}{2\tau}\right)^2\right)\right) \end{aligned} \tag{A.62}$$

However, since $\gamma(t)$ is already very small at $32\mu s$, we neglect the extra $\frac{1}{2}\left(\frac{T}{2\tau}\right)^2$ term and find that the change in the error due to pileup subtraction is, to a

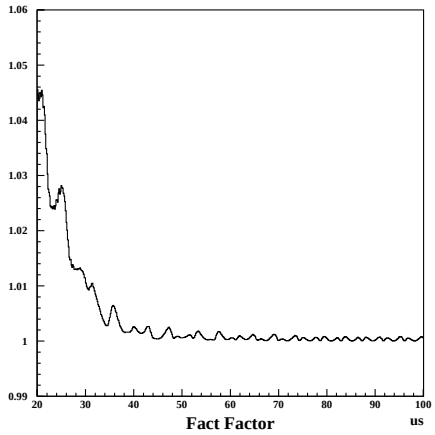

Figure A.3: The "fast factor" as a function of time after injection. This enhances the effect of pileup at early times, albeit by a small amount.

very good approximation, the same for ratio fits as for multiparameter wiggle fits: $\sigma_r^2 \to \sigma_r^2(1 + \gamma e^{-(t-t_0)/\tau})$.

One further correction must be made, and that is to the value of γ itself. At early times after injection, the bunched structure of the beam causes an enhancement of the pileup by the so-called fast-factor:

$$ff(t) = \frac{< N^2 > (t)}{< N >^2 (t)} \tag{A.63}$$

where t denotes the center of a bin of a given bin width dt. The fast factor was found by extracting $N(t)$ spectra using bin widths of $dt = 5$ ns, and taking the ratio of $N(t)^2$ rebinned with $dt = 150$ ns to the square of $N(t)$ rebinned with $dt = 150$ ns. In the 2000 data, the fast factor was found to be as large as 1.6 around 20 μs after injection, however, as shown in Fig. A.3, in the 2001 data the fast factor is only ~ 1.03 at 20 μs. The difference is due to a sharp reduction in data rate between the 2000 and 2001 runs.

We therefore find that the error on the ratio at time t is given as $\sigma_r \to \sigma_r(1 + ff(t)\gamma e^{-(t-t_0)/\tau})$. Using this improved estimation of the error bars of the ratio results in an improvement in the $\chi^2/d.o.f.$ of the 9-parameter fit by about 3×10^{-3}, changes the fitted R value by less than 0.06 ppm, and changes the statistical uncertainty on R by less than 0.005 ppm.

Bibliography

[1] W. M. Francis Farley and J. Paley, radial Electric Field and Vertical Pitch Corrections for the 2001 Data (unpublished).

[2] C. Polly, note published on http://www.npl.uiuc.edu/ polly/g-2/ (unpublished).

[3] C. S. Ozben and Y. K. Semertzidis, g-2 Note 365 (unpublished).

[4] F. James, MINUIT Reference Manual, Version 94.1.

[5] J. P. F. Farley, C. Ozben and Y. K. Semertzidis, g-2 Note 377 (unpublished).

[6] Y. Orlov, g-2 Note 335 (unpublished).

[7] Y. K. Semertzidis, g-2 Note 426 (unpublished).

[8] I. Logashenko, distributed Note, Jan. 23, 2003 (unpublished).

[9] J. Paley, review of Beam Resonance Studies in `g2track` (unpublished).

[10] Private communications with Qinzeng Peng.

[11] Carey, Robert, private communication.